NASA Grant NAGW-2727
10/1/91-3/31/94

Trace Gas Emissions to the Atmosphere by Biomass Burning in the West African Savannas

Robert Frouin, Samuel F. Iacobellis
Herisoa Razafimpanilo, Richard C. J. Somerville
Scripps Institution of Oceanography
University of California San Diego
La Jolla, California

Final Report

August 28, 1994

SUMMARY

We have focused on savanna fires and atmospheric carbon dioxide (CO_2) our NAGW-2727 investigation entitled "Trace Gas Emissions to the Atmosphere by Biomass Burning in the West African Savannas" (PI: R. Frouin; Co-PI: R. C. J. Somerville). Instead of just considering west African savannas, we have considered all north African savannas, because fires in various regions of the north African savannas occur at the same time, allowing us to study remote effects across the Atlantic Ocean. The lack of available high resolution, calibrated, and georeferenced satellite datasets over Africa has obliged us to use CO_2 emission rates available from the literature. The results of the investigation are detailed in the two attached articles.

In the first article, "North African Savanna Fires and Atmospheric Carbon Dioxide" (*J. Geophys. Res.*, 99, 8321-8334) (appendix 1), we use a 3-dimensional tracer transport model and estimates of CO_2 fluxes to quantify the effect of north African savanna fires on atmospheric CO_2 concentration, including patterns of spatial and temporal variability and significance to global emissions. The transport model simulations indicate that biomass burning in the north African savannas significantly influence atmospheric CO_2 concentrations in South America. They also show that the effect is more pronounced during the period from January through march (dry season in North Africa), when biomass burning in South America is almost non-existent. During this period, the atmospheric CO_2 concentration in parts of South America may increase by 0.5 to 0.75 ppm at 970 mb. Later in the year, when biomass burning occurs in South America, the effect of north African savanna fires becomes relatively small (10-15%) of the effect of South American fires), yet not negligible. From May through September, the effect of biomass burning in southern Africa (forests as well as savannas) may be substantial in South America. The resulting CO_2 concentration increase at 3.9°N-50°W and 970 mb may be as large (1 ppm) as the increase due to local fires. In the extreme northern and southern parts of South America, where there is little burning at this time, the effect of southern Africa fires may be 2-3 times larger than the effect of South American fires. Even in the central part of the continent, where biomass burning is most severe, southern African fires contribute to at least 15% of the CO_2 concentration increase at 970 mb. At lower pressure levels, less CO_2 from north African savanna fires reaches South America, and at 100 mb no significant amount of CO_2 is transported across the Atlantic Ocean.

In the second article, "Estimating Burned Area from AVHRR Reflectance Data" (*Rem. Sen. Environ.*, to be submitted) (appendix 2), we describe two methods to determine burned area from Advanced Very High Resolution Radiometer (AVHRR) data. The methods are based on the relationship between percentage of burned area and AVHRR channel 2 reflectance (linear method) or Normalized Difference Vegetation Index (NDVI) (non-linear method). Radiative transfer simulations indicate that the linear method, unlike the non-linear method, must be applied to top-of-atmosphere reflectances that have been corrected for atmospheric influence. For the methods to work properly, the initial background must be characterized by an AVHRR channel 2 reflectance above 9% and by a positive NDVI. In addition, the fire scar must also occupy at least 12 and 20% of the pixel in the case of savanna and green vegetation (e.g., forest),

respectively. When applied to homogeneous pixels, the mean relative error on the percentage of burned area is about 20% for the linear method and 10% for the non-linear method. The non-linear method does not perform well with heterogeneous pixels, unless the NDVI difference between the various backgrounds is below 0.1 and the background with the lowest NDVI is burned. Both methods are not applicable when the target contains very low reflectance backgrounds (e.g., water). The greenness of the vegetation and the burning efficiency may have compensatory effects: vegetation may not burn efficiently when contrast between background and burned area is high, i.e. when the methods are more accurate.

- APPENDIX 1 -

"North African Savanna Fires and Atmospheric Carbon Dioxide"
S. F. Iacobellis, R. Frouin, H. Razafimpanilo, R. C. J. Somerville, and S. C. Piper
J. Geophys. Res., **99**, 8321-8334, 1994

JOURNAL OF GEOPHYSICAL RESEARCH, VOL. 99, NO. D4, PAGES 8321–8334, APRIL 20, 1994

North African savanna fires and atmospheric carbon dioxide

Sam F. Iacobellis, Robert Frouin, Herisoa Razafimpanilo,
Richard C. J. Somerville, and Stephen C. Piper

California Space Institute, Climate Research Division, and Geological Research Division, Scripps Institution of Oceanography, University of California, San Diego

Abstract. The effect of north African savanna fires on atmospheric CO_2 is investigated using a tracer transport model. The model uses winds from operational numerical weather prediction analyses and provides CO_2 concentrations as a function of space and time. After a spin-up period of several years, biomass-burning sources are added, and model experiments are run for an additional year, utilizing various estimates of CO_2 sources. The various model experiments show that biomass burning in the north African savannas significantly affects CO_2 concentrations in South America. The effect is more pronounced during the period from January through March, when biomass burning in South America is almost nonexistent. During this period, atmospheric CO_2 concentrations in parts of South America typically may increase by 0.5 to 0.75 ppm at 970 mbar, the average pressure of the lowest model layer. These figures are above the probable uncertainty level, as model runs with biomass-burning sources estimated from independent studies using distinct data sets and techniques indicate. From May through September, when severe biomass burning occurs in South America, the effect of north African savanna fires over South America has become generally small at 970 mbar, but north of the equator it may be of the same magnitude or larger than the effect of South American fires. The CO_2 concentration increase in the extreme northern and southern portions of South America, however, is mostly due to southern African fires, whose effect may be 2–3 times larger than the effect of South American fires at 970 mbar. Even in the central part of the continent, where local biomass-burning emissions are maximum, southern African fires contribute to at least 15% of the CO_2 concentration increase at 970 mbar. At higher levels in the atmosphere, less CO_2 emitted by north African savanna fires reaches South America, and at 100 mbar no significant amount of CO_2 is transported across the Atlantic Ocean. The vertical structure of the CO_2 concentration increase due to biomass burning differs substantially, depending on whether sources are local or remote. A prominent maximum of CO_2 concentration increase in the lower layers characterizes the effect of local sources, whereas a more homogenous profile of CO_2 concentration increase characterizes the effect of remote sources. The results demonstrate the strong remote effects of African biomass burning which, owing to the general circulation of the atmosphere, are felt as far away as South America.

1. Introduction

We present a study of carbon dioxide (CO_2) emissions due to biomass burning in the savannas of north Africa. Our overall goal is to quantify the effect of the fires on atmospheric CO_2 concentration, including patterns of spatial and temporal variability and significance to global emissions. The motivation for this research is the recognized importance of biomass burning as a source of atmospheric CO_2 [e.g., *Seiler and Crutzen*, 1980], combined with the many unanswered questions regarding biomass burning and its consequences for the composition and chemistry of the atmosphere [*Crutzen and Andreae*, 1990].

There is no doubt that biomass burning, by releasing radiatively active trace gases (mostly CO_2) to the atmosphere, deserves recognition as a potentially critical initiator of anthropogenic climate change. A recent summary of the implications of biomass burning [*Levine*, 1991] points out that as much as 40% of the annual gross release of CO_2 through combustion may be due to biomass burning. Furthermore, the biomass consumed by burning of savanna grasslands, estimated at 3690 Tg of dry material per year (Tg dm/yr), exceeds the other components of biomass burning: agricultural waste, forests, and fuel wood. Human activity is responsible for most biomass burning, and the scope and magnitude of this activity is thought to be increasing with time.

It is important to note that this release does not represent a net increase to the atmosphere as this CO_2 will eventually return to the biosphere through regrowth (on a timescale of 1–5 years for savanna grasslands). Nevertheless, a more comprehensive knowledge of the short-term variability of atmospheric CO_2 will help us to better understand CO_2 variability on longer timescales and the potential impact on global warming.

Our methodology combines in situ and satellite remote sensing estimates of CO_2 fluxes which are input to a tracer

Paper number 93JD03339.
0148-0227/94/93JD-03339$05.00

transport model. Using wind data from operational numerical weather prediction analyses, the model then provides CO_2 concentrations as a function of space and time. We validate the results by comparing these model products with measured concentrations at experimental sites. We focus on remote effects in South America, where systematic burning of the Amazonian tropical rain forests and cerrado (consisting of grasslands, savannas, and semideciduous forests [*Ward et al.*, 1992]) occurs for land use purposes.

2. Three-Dimensional Transport Model

We use the tracer transport model of *Russell and Lerner* [1981] as modified by *Heimann and Keeling* [1989]. This model is similar to the global atmospheric general circulation model (GCM) of *Hansen et al.* [1983], in that it has a coarse horizontal spatial resolution (approximately 8° latitude by 10° longitude) and nine levels in the vertical. The wind fields used in the model, however, are not those produced by the GCM. Instead, following *Heimann and Keeling* [1989], we use winds based on meteorological observations which have been processed by the four-dimensional data assimilation system of the European Centre for Medium-Range Weather Forecasts (ECMWF). Like them, we have employed the widely used data from the 1978 to 1979 Global Weather Experiment, in which the routine weather observations were supplemented by many special observing systems to give an unusually accurate and complete description of the global atmospheric circulation. In addition to simulating the effects of advection of tracers by these wind fields, the model also simulates the effects of small-scale vertical convective processes on tracer concentrations, using a parameterization based on that of the GCM. Horizontal diffusion of CO_2 is taken into account as well. For a detailed description of these aspects of the model, see *Heimann and Keeling* [1989].

The CO_2 sources and sinks used in the transport model, except biomass burning, are those of *Heimann and Keeling* [1989]. They comprise natural (oceanic, terrestrial biospheric) and anthropogenic (industrial) components. *Heimann and Keeling*'s [1989] biospheric destruction component, based on data compiled by *Houghton et al.* [1987], is too crudely established for the purpose of our study. Seasonal patterns are not accounted for, and biomass burning emissions from savanna fires, which according to *Hao et al.* [1990] account for 75% of the CO_2 emissions, are not included. For convenience we keep *Heimann and Keeling*'s [1989] land use and deforestation source but add more recent and complete estimates of CO_2 emissions by biomass burning. Since the transport model is linear, differences between concentrations obtained using *Heimann and Keeling*'s [1989] source only and those obtained by adding the more recent estimates should show the effect of the more recent estimates.

3. CO_2 Emissions by North African Savanna Fires

The fluxes of CO_2 resulting from north African savanna fires are treated as varying both seasonally and spatially. They are not balanced but represent a net release of CO_2 to the atmosphere. Monthly values are estimated from the results of two independent studies, and the estimates are contrasted to evaluate their accuracy.

The first estimate is obtained from the distribution of CO_2 in tropical regions given by *Hao et al.* [1990] and based on the areas of annual land clearing compiled for individual countries by the Food and Agricultural Organization (FAO) [*Lanly*, 1982]. The monthly gross, CO_2-C (carbon contained in CO_2) emissions by forests and savannas in 5° latitude × 5° longitude cells are presented as well as the three months of most severe burning. Since the authors assume that the first and the last month of a 5-month burning period each contribute to 12.5% of the annual emission, while the three middle months contribute to 25% of that emission, and since they give the emissions per month of intense burning, the annual emission is 4 times the amounts reported. To estimate the month by month emissions, we use the above coefficients for the five months of burning, respectively, and we assume that fires did not occur before and after the dry season.

The second estimate is based on the calculations of *Menaut et al.* [1991] from satellite estimates of maximum biomass obtained by *Loudjani* [1988]. These calculations, which use ranges of values for the relevant parameters (maximum biomass, area burnt, burning efficiency), provide minimum, maximum, and average CO_2-C emissions for each type of savanna. Each 5° latitude × 5° longitude grid cell is first partitioned into types of savanna (Guinean, southern Sudanian, northern Sudanian, and Sahelian), classified by climate and biomass density. The CO_2-C emission in each cell is then computed by weight-averaging emissions by individual savannas according to the fraction of the cell they occupy. The computations are extended to the region east of 15°E, assuming that the characteristics of the CO_2 emissions are comparable for the same type of savanna. Since the emission obtained is annual and corresponds to the dry season, we divide the resulting amounts by 4 to make them comparable to the estimates based on the study of *Hao et al.* [1990]. The month by month emissions are deduced by dividing the annual estimates by the number of burning months, which also depends on the type of savanna, as given by *Menaut et al.* [1991].

Figure 1 displays the CO_2-C emissions (in units of teragrams of equivalent carbon per month and per grid cell, hereafter Tg CO_2-C) obtained from the two studies. Average values range approximately from 0.4 to 7 Tg CO_2-C (Figures 1a and 1b), but those based on *Menaut et al.* [1991] are generally lower. For both estimates, high emissions are located between 5°N and 12°N, a region dominated by high grass savannas (Guinean and south Sudanian savannas). In the western part the *Hao et al.* [1990] study yields higher values in the vicinity of the Ivory Coast (5°N–10°N; 5°W), whereas the *Menaut et al.* [1991] study yields higher values around 5°E, thus eastward by 10° of longitude. In the eastern part, differences between estimates based on *Hao et al.* [1990] and *Menaut et al.* [1991] are difficult to interpret since generalizing the characteristics of the western savannas reported by *Menaut et al.* [1991] might not be correct: more observational data are needed. Furthermore, the distribution of the region's bioclimatic zones is still not well known. Nevertheless, both estimates give a similar spatial distribution of sources east of 15°E, with maximum values in the north of the Central African Republic (8°N–10°N; 15°E–25°E). In the north Sahelian region, where the carbon emissions are the lowest (0.4 to 1 Tg CO_2-C), both estimates are in good agreement except in the area north of Senegal where the estimates obtained from *Hao et al.* [1990] (Figure

1a) are generally higher than the maximum values obtained from *Menaut et al.* [1991] (Figure 1d). The differences might be due to the months of burning considered, from January to May for *Hao et al.* [1990] (severe burning from February to April) and from September to December for *Menaut et al.* [1991], knowing that fires occurring at the end of the dry season are more efficient than earlier fires. Since the spatial location of fires extends northward when moving from east to west, as documented by *Razafimpanilo* [1991], local factors such as population density or land use practices may influence considerably the distribution of CO_2 emissions. Such local factors are not taken into account in the calculations of *Menaut et al.* [1991]. The *Hao et al.* [1990] results, based on ground reports, include in some way the effect of local factors, but those reports are scarce in the tropics. This suggests that actual emissions may be underestimated by *Hao et al.* [1990]. The minimum values of *Menaut et al.* [1991] are lower than the values of *Hao et al.* [1990] (Figures 1c and 1a), but the maximum values of *Menaut et al.* [1991] are not everywhere higher than the values of *Hao et al.* [1990], especially north of 15°N (Figures 1d and 1a). As evidenced in Figure 2, the correlation between estimates from *Hao et al.* [1990] (Figure 1a) and *Menaut et al.* [1991] (Figure 1b) is poor. The linear correlation coefficient is only 0.2 at the 99% confidence level and the standard deviation is approximately 1.8 Tg CO_2-C (80% of the average value from *Hao et al.* [1990]), suggesting that estimates of CO_2 emissions by north African savanna fires based on available data are still inaccurate.

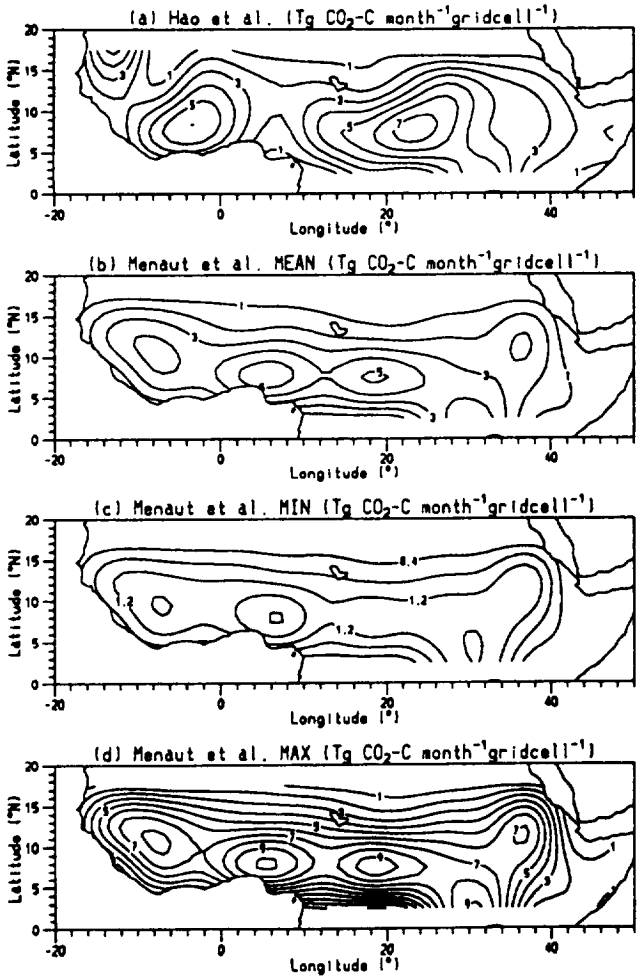

Figure 1. Biomass-burning emission of CO_2 in the north African savannas in teragrams (Tg) CO_2-C per month and 5° latitude × 5° longitude given by (a) *Hao et al.* [1990] and (b), (c), and (d) estimated from *Menaut et al.* [1991]. The contour plots in Figures 1b, 1c, and 1d correspond to average, minimum, and maximum values, respectively.

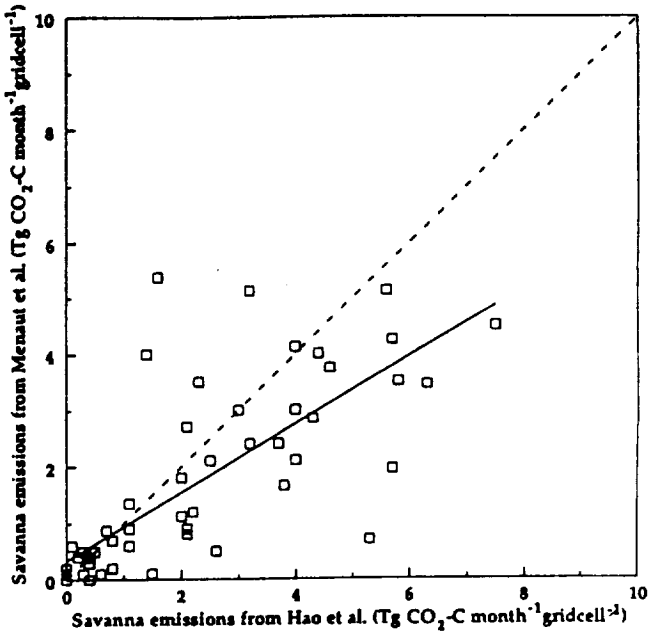

Figure 2. Biomass-burning emission of CO_2 in the north African savannas in Tg CO_2-C per month and 5° latitude × 5° longitude given by *Hao et al.* [1990] versus the average emission estimated from *Menaut et al.* [1991]. The linear correlation coefficient between the two estimates is 0.21 at the 99% confidence level.

The inaccuracy of the estimates is linked to the difficulty of estimating the biomass available for burning before the fires, the burning efficiency (which may increase as the dry season progresses), and the total area actually burnt, parameters not always available or not easily inferred from satellite imagery. The discrepancy between the estimates may also be due to the different years of the data sets considered: 1975 to 1980 for *Hao et al.* [1990] and 1983–1984 for *Menaut et al.* [1991]. More detailed studies in time (to determine the effective months of burning) and space (to better locate the sources) are certainly needed to improve the accuracy of the estimates. In any case, the comparison presented above enables us to interpret our transport model experiments more confidently, by making sure that the predicted effects are significant and not the result of uncertainties in the emissions.

4. Model Experiments

A series of seven numerical experiments have been performed to investigate the transport of emissions from biomass burning in the north African savannas. Each experiment is initiated with an identical spin-up cycle. The spin-up begins January 1, 0000 GMT and continues for 4 simulated years and 9 months ending October 1, 0000 GMT. The

Table 1. Experiment Names and CO_2 Sources/Sinks Used for Each Numerical Experiment

Experiment Name	Sources During Spin-up	Sources During Last Year
CONTROL	HK89	HK89
NAS	HK89	HK89 + H90-NAS
SAS	HK89	HK89 + H90-SAS
AFR	HK89	HK89 + H90-AFR
SA	HK89	HK89 + H90-SA
NAS-SA	HK89	HK89 + H90-NAS + H90-SA
GLOBAL	HK89	HK89 + H90-GLOBAL

Each experiment is initiated with an identical spin-up cycle beginning January 1, 0000 GMT and continues for 4 simulated years and 9 months ending October 1, 0000 GMT. The spin-up cycle is initialized with a uniform global CO_2 concentration of 350 ppm and utilizes the CO_2 sources and sinks compiled by *Heimann and Keeling* [1989] (HK89) and the 1979 wind fields from the European Centre for Medium-Range Weather Forecasts analysis. Each model experiment is then run for an additional year beginning October 1, 0000 GMT utilizing the particular set of CO_2 sources and sinks listed in the table. The CO_2 sources and sinks are defined in the text.

spin-up cycle is initialized with a uniform global CO_2 concentration of 350 ppm and utilizes the CO_2 sources and sinks compiled by *Heimann and Keeling* [1989] and the 1979 wind fields from the ECMWF analysis. As noted earlier, the year 1979 is selected because of the unprecedented amount of observations assimilated into the ECMWF analysis through the Global Weather Experiment. As the present study focuses on the potential impact of biomass burning on the seasonal cycles of CO_2, the use of a single year of wind fields is justified. At the end of the spin-up period the cycle of CO_2 concentration is both in equilibrium (relative to the annual average at the south pole) and realistic (see section 5).

After the spin-up period each model experiment is run for an additional year beginning October 1, 0000 GMT utilizing a particular set of CO_2 sources and sinks. The initial date is chosen because it corresponds to minimum biomass burning in both the north African and the South American savannas according to the data of *Hao et al.* [1990]. This allows a smooth start-up from the conditions at the end of the spin-up cycle for each of the experiments performed.

Table 1 lists the names of and the CO_2 sources/sinks used for each numerical experiment. HK89 denotes the CO_2 sources and sinks of *Heimann and Keeling* [1989], including the biospheric destruction component, H90-NAS is the CO_2 source due to biomass burning in the north African savannas only, H90-SAS is the CO_2 source due to biomass burning in the south African savannas only, H90-AFR is the CO_2 source due to biomass burning in Africa only, H90-SA is the CO_2 source due to biomass burning in South America only, and H90-GLOBAL is the CO_2 source due to biomass burning in all regions of the tropics. The last five sources, which are time varying, are constructed from the data of *Hao et al.* [1990], as described in section 4 for the north African savanna component. Interpolation and integration of the biomass-burning data onto the transport model grid follows the methodology of *Heimann and Keeling* [1989]. Despite the possibility that there may be errors in the timing of the maximum burning in the north African savannas, estimates from H90 are selected for the biomass-burning sources, because unlike those of *Menaut et al.* [1991], they cover the entire tropics, allowing comparisons of effects from various regions using a single, consistent data set. Estimates from *Menaut et al.* [1991] for north African savannas are used but only to provide uncertainty levels for the results obtained with estimates from *Hao et al.* [1990]. These discrepancies between data sets point out the serious need for studies using field work and remote sensing to establish an accurate distribution of biomass burning in space and time. *Cahoon et al.* [1992] studied the temporal and spatial variations of African savanna fires using nighttime satellite imagery. While this work is too qualitative to be included in the present study, this technique may provide a significant verification tool in future studies.

5. Discussion

Figure 3 shows modeled annual cycles of atmospheric CO_2 concentration in the lowest layer (1000–940 mbar) at grid cells corresponding to three measurement locations in the Atlantic, namely, Terceira Island (38°45'N–27°05'W), Ascension Island (7°55'S–14°25'W), and Ragged Point (13°10'N–59°26'W), together with the observed annual cycles at these sites. The HK89 + H90-GLOBAL sources are used in the transport model (GLOBAL run), and the observed values are those reported by *Boden et al.* [1991]. Except for Ascension Island, where the weak annual cycle is underestimated, the modeled amplitudes agree well with the observations. Modeled and observed maxima and minima occur during the same months, indicating that the seasonal uptake and release of CO_2 are modeled properly. As the effect of biomass burning is small at the sites selected, running the transport model without the H90-GLOBAL sources (HK89 run) yields insignificant differences (not shown here).

To further verify the transport model, we compare simulated vertical profiles of CO_2 concentration near Korhogo, Ivory Coast, in October, when biomass burning is nonexistent (rainy season), and in January, when biomass burning occurs (dry season) (Figure 4). The model is run with the HK89 + H90-GLOBAL sources. By January the CO_2 concentration in the surface layers has increased by about 11 ppm. Vertical profiles of CO_2 concentration similar to the January profile of Figure 4 were measured near Korhogo at the end of December 1987 during the Tropospheric Ozone

(TROPOZ) I campaign [*Delmas et al.*, 1991], indicating that the model outputs are realistic, even when the H90-GLOBAL sources are added to the HK89 sources despite some overlap in biomass-burning sources.

The remainder of this discussion focuses on the temporal and spatial effects that biomass burning may have on the atmospheric CO_2 budget. To isolate the effects of biomass burning from other CO_2 sources and sinks, the CO_2 concentration from the CONTROL run is subtracted from the CO_2 concentration of the particular model run at each grid point. In this manner the effects from CO_2 sources and sinks due to industrial, oceanic, and photosynthesis processes are removed.

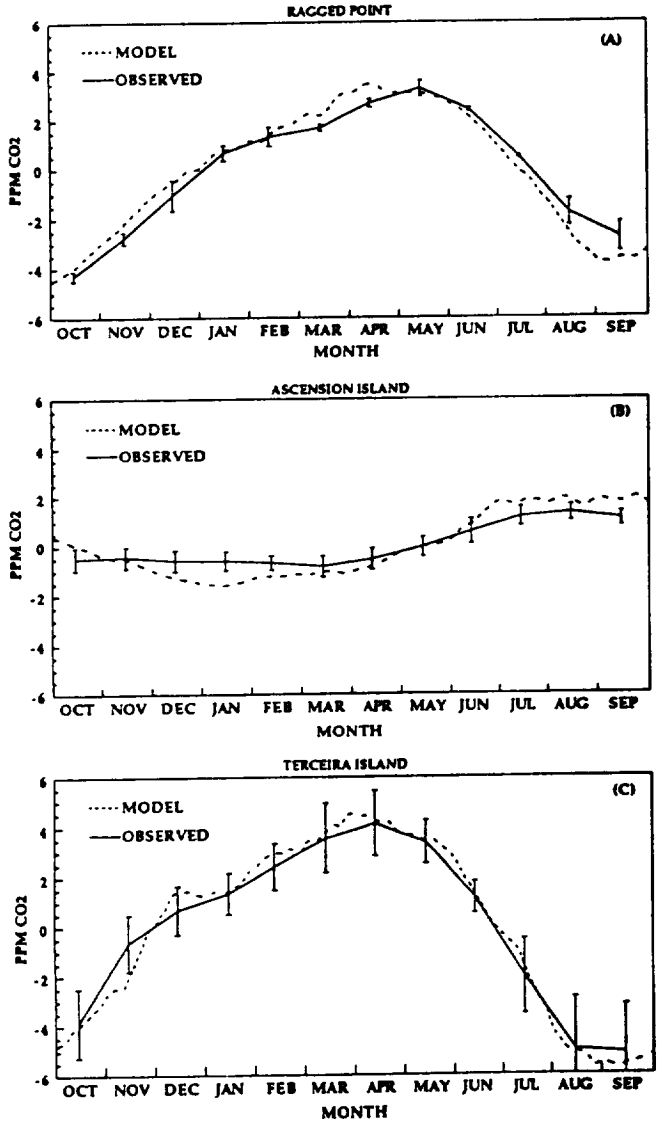

Figure 3. The annual cycle of CO_2 concentration in units of parts per million (ppm) with the annual mean removed at (a) Ragged Point (13°N–50°W), (b) Ascension Island (8°S–14°W), and (c) Terceira Island (39°N, 27°W). The solid curve is the result of model run CONTROL and the dashed curve is the observed concentration. The observed concentration curves are produced by calculating the seasonal cycle (annual mean removed) for each year of available data and then taking the average of these seasonal cycles. The error bars on the observed curves show the standard deviation.

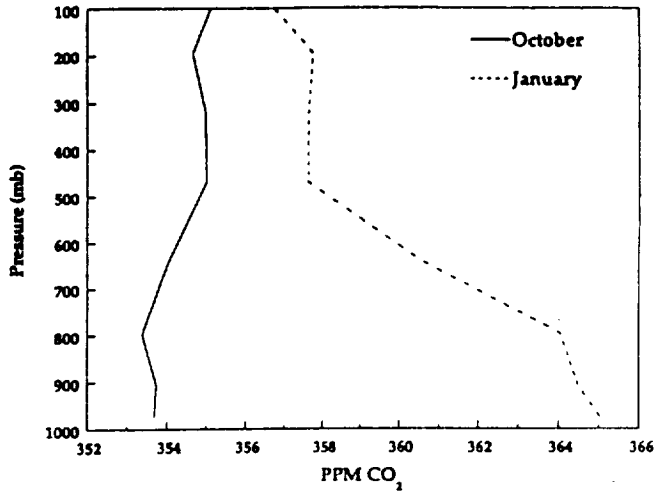

Figure 4. The average vertical profile of CO_2 concentration during October (solid curve) and January (dashed curve) from model run GLOBAL at 11.7°N–10°W (near Korhogo, Ivory Coast).

Plate 1 shows, for various times of the year, the difference in the CO_2 concentration between model runs NAS + SA and CONTROL at 970 mbar (average pressure of lowest model layer) at three different times of the year. By subtracting the CO_2 concentration of the CONTROL run, the effects of biomass burning in the north African savannas and South America are isolated. In the top map (December 28), the CO_2 emissions from biomass burning in the north African savannas are maximum over the African continent but extend westward over the tropical Atlantic Ocean and onto the South American continent. The results from model run NAS (not shown) verify that the majority of the CO_2 difference over South America at this time is due to burning in the north African savannas and not due to local burning in northern South America or Central America. By February 1 (middle map) the emissions from the north African savannas have intensified over both the Atlantic Ocean and South America. It is not until later in the year (July 21, bottom map) that the emissions from biomass burning in South America become significant. These results are in qualitative agreement with other studies that have shown that north African dust/aerosols are frequently carried across the Atlantic Ocean to South America [e.g., *Prospero et al.*, 1981; *Talbot et al.*, 1990; *Andreae et al.*, 1990].

These maps illustrate two important points: (1) the peak emissions from biomass burning in the north African savannas and South America are separated in time by about six months and (2) the emissions from the north African savannas may have a significant impact on the CO_2 concentration over parts of South America. To further investigate the latter point, the CO_2 concentrations from experiments CONTROL, NAS, and SA are examined at 3.9°S–50°W, a selected location in South America. Figure 5a displays as a function of time the difference between CO_2 concentrations at 970 mbar from experiments NAS and CONTROL (solid line) and SA and CONTROL (dashed curve). It is evident that at 3.9°S–50°W the effects of biomass burning in the north African savannas are largest during January and February, while the effects of biomass burning in South America are

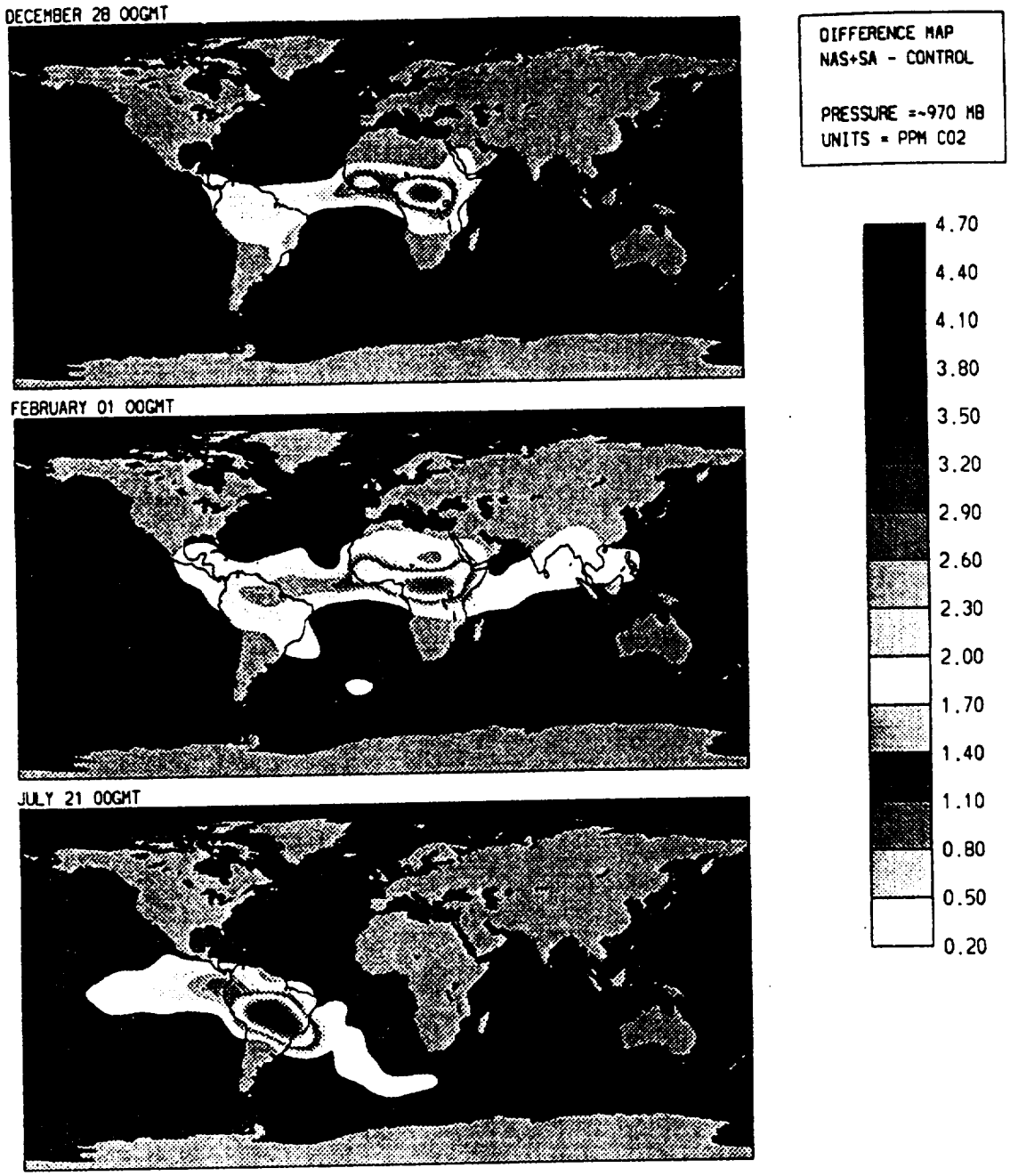

Plate 1. The difference between CO_2 concentrations (ppm) at 970 mbar from model run NAS + SA and model run CONTROL at three instances: (top) December 28, (middle) February 1, and (bottom) July 21.

largest from June through September. The maximum increase in CO_2 concentration due to the burning in South America (about 1.4 ppm) is roughly twice the maximum increase due to the burning in the north African savannas. After May the residual effect of north African savanna fires, which dominated from December through April, has been reduced to 10–15% of the effect of South American fires. Note in Figure 5a that the CO_2 concentration increase due to South American fires is as high as 0.4 ppm just after spin-up (local burning still occurs in October).

Other biomass-burning sources may affect the CO_2 concentration increase at 3.9°S–50°W, as Figure 5b demonstrates. This figure displays, as a function of time, the difference between CO_2 concentrations at 970 mbar from experiments NAS + SA and CONTROL (dashed curve) and GLOBAL and CONTROL (solid curve). Biomass burning in northern African forests, southern Africa, and southeast Asia, not included in experiment NAS + SA but included in experiment GLOBAL, significantly increases the CO_2 concentration at 3.9°S–50°W, especially from June through September. The effect of additional sources, however, is generally less than the effect of biomass burning in the north African savannas and South America (NAS + SA experiment). At the end of the runs, the effect of additional sources

increase is 60% of the combined effect of biomass burning in the north African savannas and South America and approximately 4 times the effect of biomass burning in the north African savannas. This result is typical of other nearby model grid points.

The additional sources that contribute to the CO_2 concentration increase at 3.9°S–50°W originate mostly from Africa (southeast Asia or Australia emissions are too remote). Figure 6 shows the ratio of CO_2 emissions from north African savannas to the total African emissions, during the course of the year, as well as the total African emissions (estimates are from *Hao et al.* [1990]).. The emissions from southern Africa dominate the total emissions from June through October and are responsible for increasing by 60% the CO_2 concentration increase due to biomass burning in the north African savannas and South America at 3.9°N–50°W in September (Figure 6b).

The relative importance of emissions from north African savannas and South America may vary depending on geographic location. Plate 2 shows for two time periods, January 25 to February 7 and July 18–31, the spatial distribution in South America of the ratio of the differences between CO_2 concentrations at 970 mbar from experiments NAS and CONTROL and SA and CONTROL. For convenience the ratio is scaled logarithmically. During the first period (top map) the influence of north African savannas generally dominates, except in the northwestern and southern parts of the continent where Central American and South American fires have, respectively, the major effect. During the second period (bottom map) local emissions largely govern the spatial patterns of CO_2 concentration increase in most regions. In the center of the continent, for instance, only 3–5% of the CO_2 concentration increase is due to north African savanna fires. In the northern and southern parts of the continents, however, the effect of north African savanna fires is similar to or even larger than the effect of South American fires.

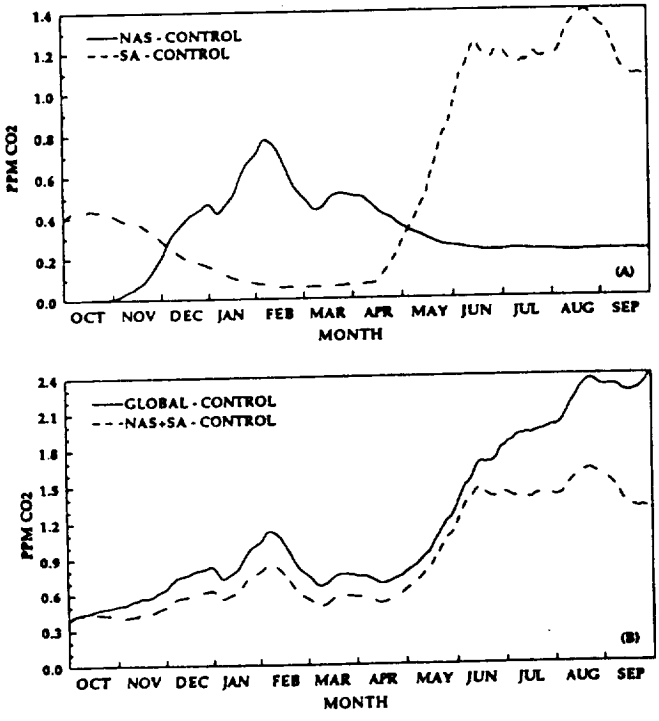

Figure 5. (a) The annual cycle of the difference between CO_2 concentrations (ppm) at 3.9°S–50°W and 970 mbar from model runs NAS and CONTROL (solid curve) and SA and CONTROL (dashed curve). (b) Same as Figure 5a but model runs NAS + SA and CONTROL (dashed curve) and GLOBAL and CONTROL (solid curve).

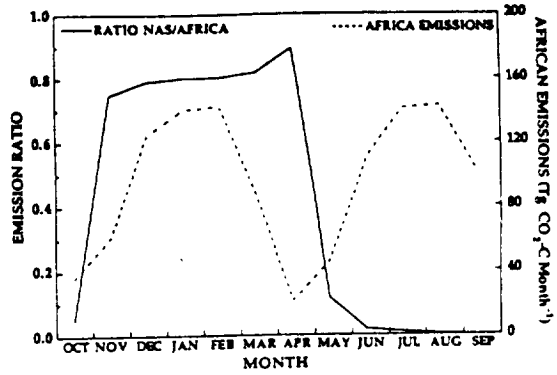

Figure 6. The fraction of African biomass-burning emissions (CO_2) from north African savannas to total African emissions (solid curve), and the amount of biomass burning emissions (CO_2) in units of Tg CO_2-C per month (dashed curve). Both of these curves are based on the data of *Hao et al.* [1990].

The ratio is substantially modified when emissions from the entire African continent are considered instead of emissions from only north African savannas, revealing the reduced influence of local (South American) fires (Plate 3). During the January 25 to February 7 period, burning of north African forests enhances the African effect, especially in the southern part of the continent. During the July 18–31 period the effect of South American fires is preponderant in a more limited region, but African emissions contribute to at least 25% of the total CO_2 concentration increase.

The patterns of variability described above are not the result of uncertainties in the estimates of CO_2 release, as Figure 7 indicates. This figure displays, as a function of time, the difference between CO_2 concentrations of the NAS experiment and those obtained when the CO_2 emissions by north African savanna fires are estimated from *Menaut* [1991]. Except for January and February, when the difference reaches 0.2 ppm, both estimates yield CO_2 concentrations at 3.9°S–50°W that generally agree within 0.1 ppm. Thus the effect of uncertainties in the biomass-burning emissions are small compared with the effect of the emissions themselves, which is typically an order of magnitude larger (Figure 4). Because the grid point of interest is far from the source region, the difference in CO_2 concentrations remains small, even though the discrepancy between the biomass-burning emissions from *Hao et al.* [1990] and *Menaut et al.* [1991] is large (see Figures 1 and 2). Note that the estimates from *Menaut et al.* [1991] yield higher CO_2 concentrations than those from *Hao et al.* [1990] at 3.9°S–50°W during October–December, which may be linked to the period of severe burning reported by the authors. According to *Menaut et al.* [1991], intense burning typically occurs earlier than indicated by *Hao et al.* [1990].

Thus far our discussion has focused on CO_2 concentrations in the lowest model layer, centered at 970 mbar. In

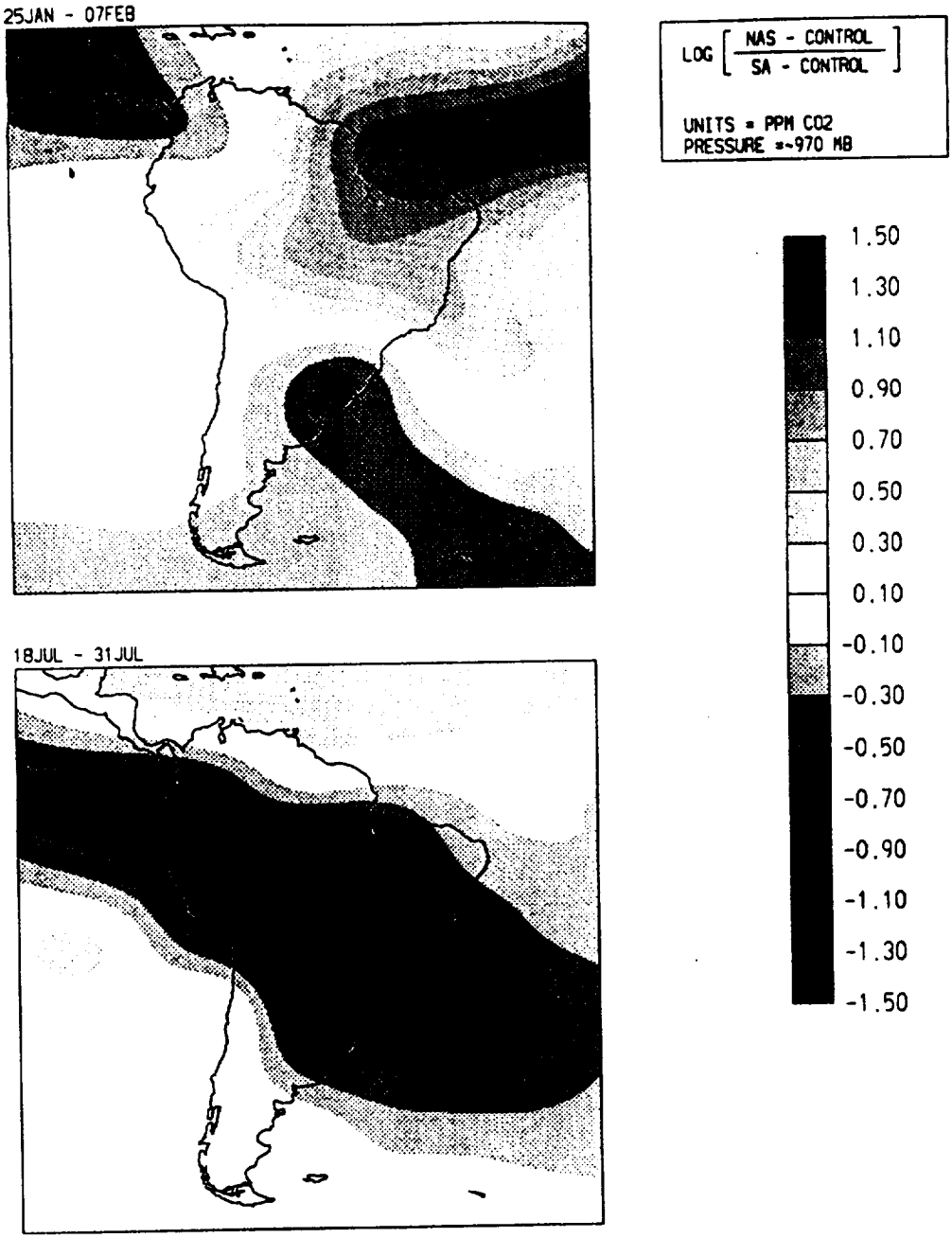

Plate 2. The ratio, scaled logarithmically, of differences between CO_2 concentrations at 970 mbar from experiments NAS and CONTROL and SA and CONTROL during January 25 to February 7 (top map) and July 18–31 (bottom map).

higher layers the effect of biomass-burning emissions is generally smaller, not exceeding 1.0 ppm at 470 mbar and 0.7 ppm at 100 mbar on December 28, February 1, and July 21 (Plates 4 and 5, respectively). At 470 mbar, CO_2 from north African savanna fires is transported both westward and eastward (Plate 4, maps of December 28 and February 1). Not much CO_2, however, reaches Pacific Ocean longitudes. Over South America, local effects are significant, yet small (0.2–0.4 ppm). Later in the year (Plate 4, map of July 21), the effect of South American fires, which are almost entirely responsible for the CO_2 concentration increase at 470 mbar, is felt as far as southern Africa. At 100 mbar, due to a predominantly eastward atmospheric circulation, no CO_2 from north African savanna fires is transported across the Atlantic Ocean (Plate 5, maps of December 28 and February 1). Some CO_2 from South American fires, however, is locally transported upward and reaches that level. On July 21 (Plate 5, bottom map) the CO_2 increase due to South American fires has spread both eastward and westward, forming a continuous, zonally oriented band extending over all longitudes.

Now we examine the vertical structure of the CO_2 concentration increases at 3.9°S–50°W during two 14-day periods: January 25 through February 7 (period 1) and July 18 to

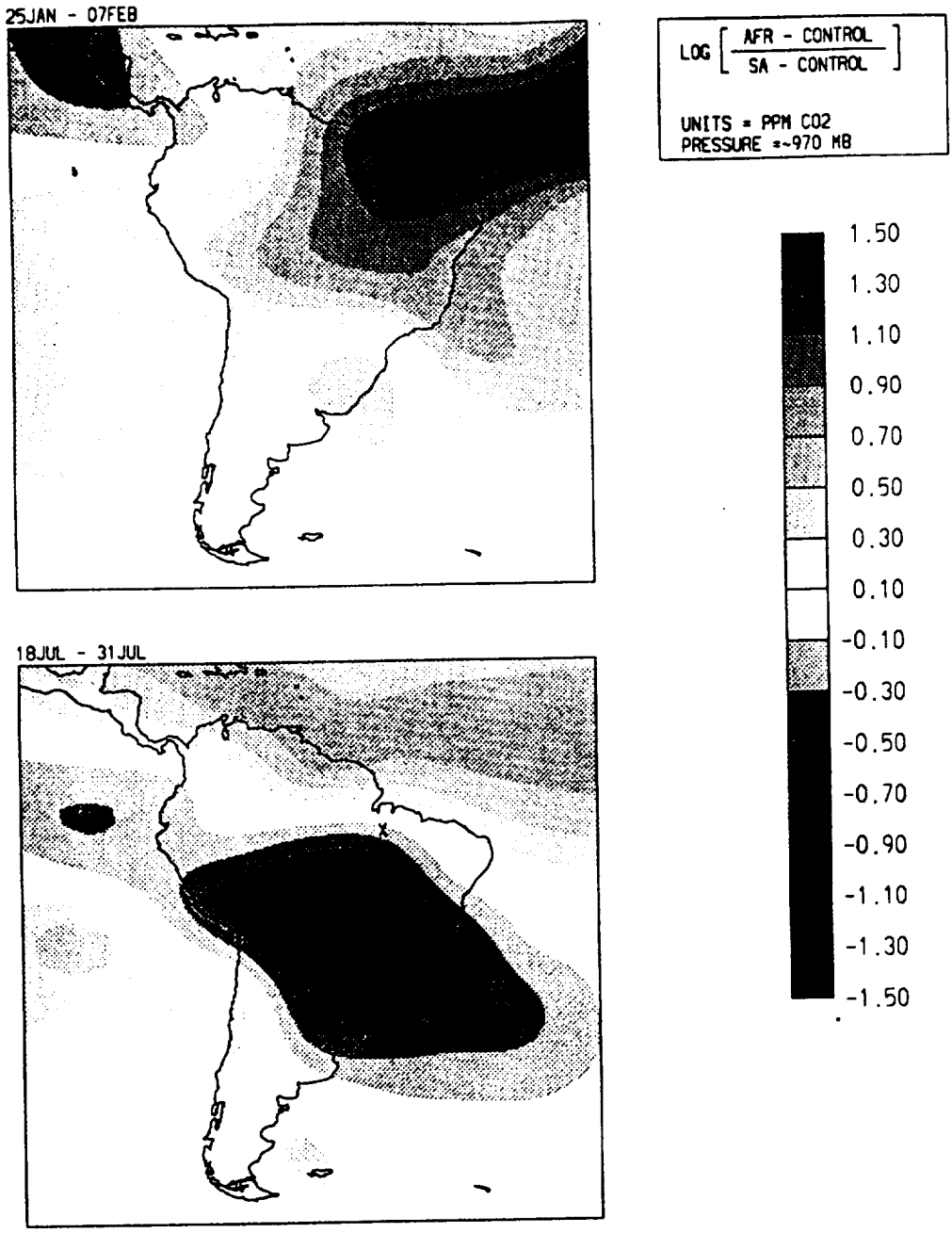

Plate 3. Same as Plate 2 but experiment AFR (all African emissions) instead of NAS.

July 31 (period 2). These periods correspond, respectively, to the times when the burning in the north African savannas and South America have their largest effect at 3.9°S–50°W. We examine the quantity $dC(z)$ which for model run NAS + SA is defined as

$$dC(z) = [C_{NAS+SA}(z)] - [C_{CONTROL}(z)], \quad (1)$$

where C is the CO_2 concentration from the particular model run, z refers to each model level in the vertical, and the brackets indicate an average over the 14-day period.

Figure 8 shows the vertical profiles of the ratio $dC(z)/dC(z = 0)$ at 3.9°S–50°W from model run NAS + SA during the two periods defined above. During period 1 the increase in CO_2 concentration due to biomass burning extends considerably farther into the middle troposphere than during

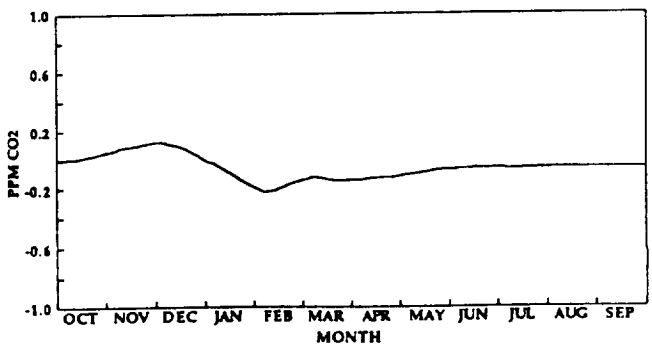

Figure 7. Difference between CO_2 concentrations from the NAS experiment and those obtained with CO_2 emissions estimated from *Menaut et al.* [1991] at 3.9°S–50°W.

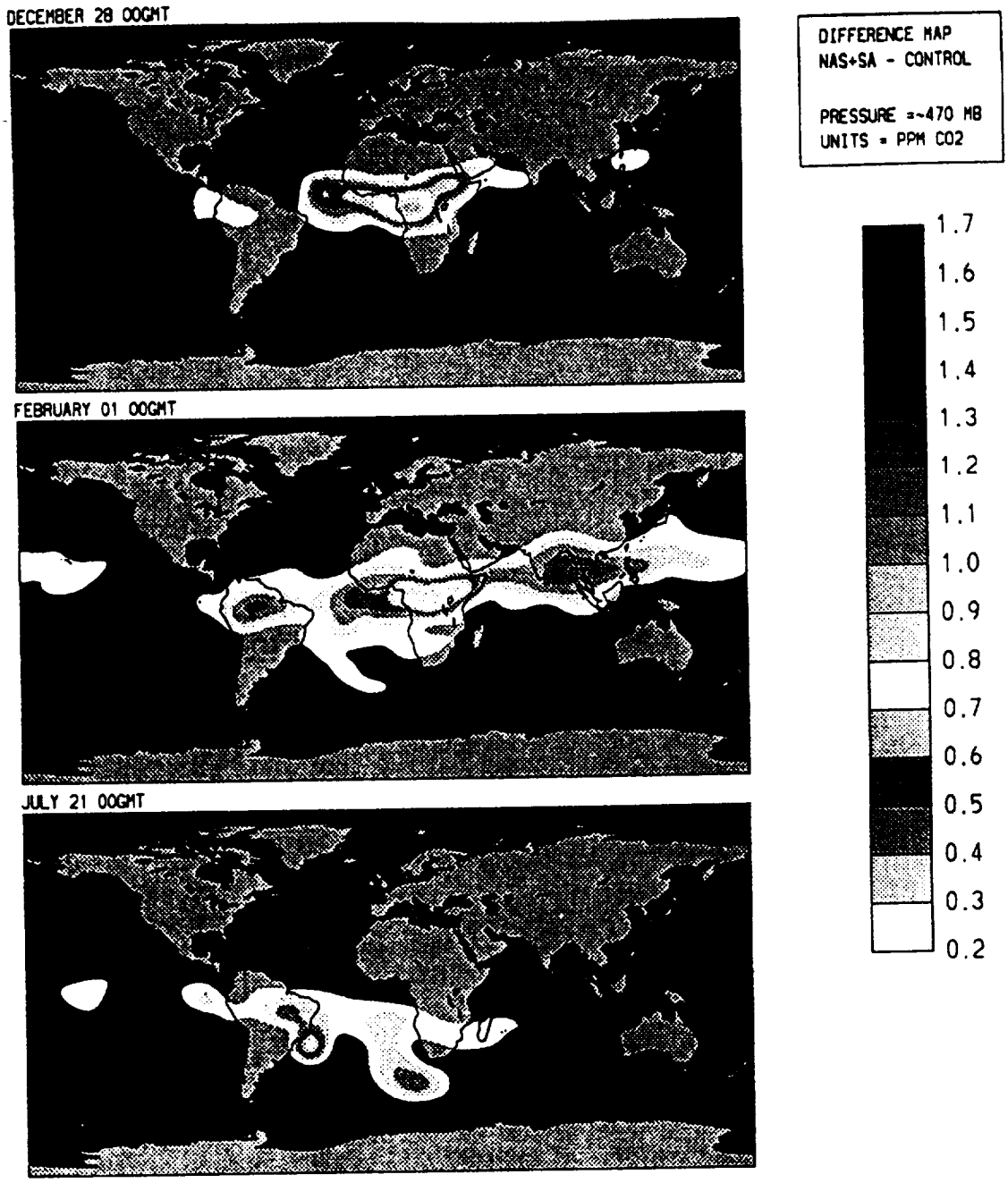

Plate 4. Same as Plate 1 but 470 mbar.

period 2. Since the increase in CO_2 concentration is primarily from north African savannas during period 1 and from South America during period 2, the difference between the vertical profiles may be related to the source region and the distance between the source region and 3.9°S–50°W. As we are looking at periods from different times of the year, it is also possible that the difference in the vertical profiles may be due to different local conditions (i.e., convection).

The vertical cross section of $dC(z)/dC(z = 0)$ obtained for period 1 along the path from 3.9°S–50°W to 7.5°N–20°E, a point located in the north African savannas, is shown in Figure 9. At the eastern end (beginning) of the path the profile $dC(z)/dC(z = 0)$ is similar in shape to the profile of period 2 at the western end (Figure 8). As the path is followed westward, the shape of the profile $dC(z)/dC(z = 0)$ changes dramatically, with a pronounced maximum near 800 mbar over the Atlantic Ocean and isolines generally displaced upward, except west of 35°W, where the isolines become less crowded. This implies that the shape of the profile during period 1 in Figure 8 is partly due to processes that take place during the transport from the source region (north African savannas), which tend to homogenize the CO_2 concentration vertically. This implies that the effect of remote sources are more likely to be observed in the surface layers rather than in the upper layers.

In the above discussion we have contrasted the effects of

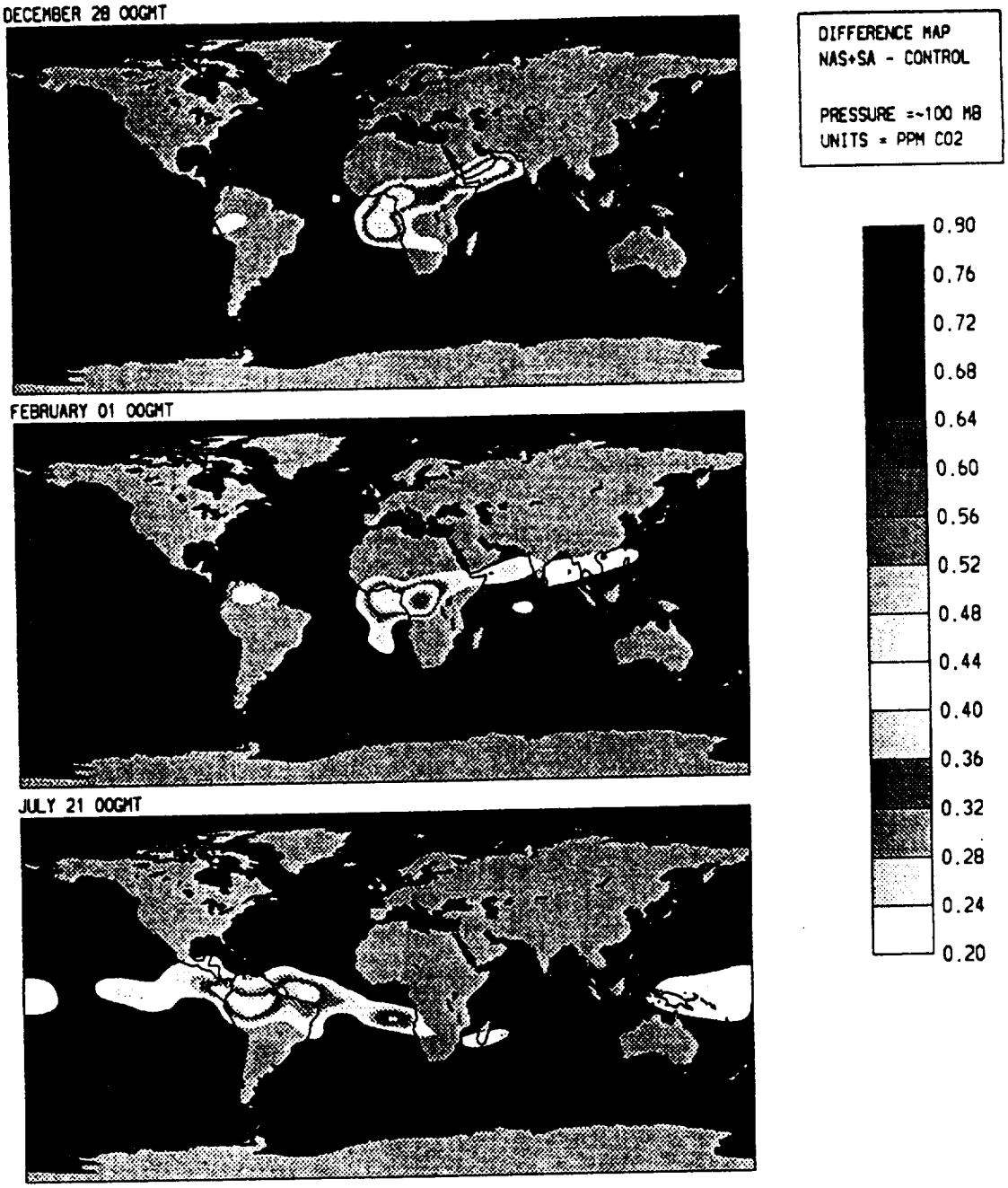

Plate 5. Same as Plate 1 but 100 mbar.

biomass burning in the north African savannas (or all Africa) against the effects from burning in South America. We now discuss briefly the relative effects of biomass burning in the northern and southern African savannas. Plate 6 contains results from model runs NAS and SAS at 800 mbar (our choice of 800 mbar is to compare to ozone measurements; see below). The quantity shown in these maps is the difference between model run NAS (or SAS) and CONTROL averaged over January (or August). The emissions from model runs NAS and SAS are maximum during the months of January and August, respectively.

These results show that emissions from both NAS and SAS are transported over the Atlantic Ocean and onto the South American continent. The emissions from SAS tend to be transported across South America at a more northerly latitude and extend farther into the Pacific Ocean than the emissions from NAS. Conversely, the emissions from NAS extend much farther to the east than the emissions from SAS. It is also evident that biomass burning in both the southern and the northern African savannas are responsible for roughly equal increases in CO_2 concentration over the Atlantic Ocean at 800 mbar.

Fishman et al. [1992] used measurements from 11 years (1979–1989) of satellite data and 11 months (July 1990 to May 1991) of ozonesonde data to map the distribution of tropospheric ozone in the tropics. The satellite-derived results

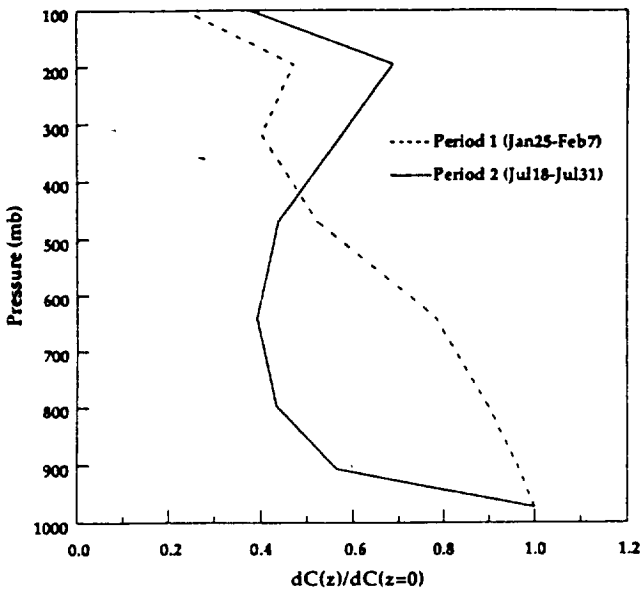

Figure 8. The mean vertical profile of $dC(z)/dC(z = 0)$ at 3.9°S–50°W from model run NAS + SA during January 25 to February 7 (solid curve) and July 17–31 (dashed curve).

show high concentrations of tropospheric ozone over the southeastern tropical Atlantic Ocean during the months of August through November that are associated with biomass burning in southern Africa. The same satellite data sets show no corresponding high concentrations of tropospheric ozone during the burning season of northern Africa. However, ozonesonde measurements at Ascension Island (8°S, 14°W) indicate the presence of elevated tropospheric ozone concentrations between 2–4 km (≈ 800–650 mbar) during both burning seasons. Our results suggest, even though CO_2 unlike ozone is a passive tracer, that elevated ozone levels over the tropical Atlantic Ocean should be observed during both burning seasons.

6. Conclusions

Our transport model simulations indicate that biomass burning in the north African savannas significantly influences atmospheric CO_2 concentrations in South America. The effect is more pronounced during the period from January through March (dry season in north Africa), when biomass burning in South America is nearly nonexistent. During this period the atmospheric CO_2 concentration in parts of South America may increase by 0.5 to 0.75 ppm at 970 mbar. Later in the year, when biomass burning occurs in South America, the effect of north African savanna fires becomes relatively small (about 10–15% of the effect of South American fires), yet not negligible. From May through September the effect of biomass burning in southern Africa (forests as well as savannas) may be substantial in South America; the resulting CO_2 concentration increase at 3.9°S–50°W and 970 mbar is as large (1 ppm) as the increase due to local fires. In the extreme northern and southern parts of the continent where there is little or no local burning at this time, the effect of southern Africa fires may be 2–3 times larger than the effect of South American fires. Even in the central part of the continent, where biomass burning is most severe, southern African fires contribute to at least 15% of the CO_2 concentration increase at 970 mbar. These results suggest that surface CO_2 concentration measurements in South America should be interpreted with care, for they may not represent the effect of local CO_2 emissions by biomass burning, even when the measurements are made during the "fire season." At lower pressure levels, less CO_2 from north African savanna fires reaches South America, and at 100 mbar no significant amount of CO_2 is transported across the Atlantic Ocean.

The simulated effect of savanna fires on atmospheric CO_2 concentration in South America appears to be real and not merely the result of uncertainties in CO_2 emissions, as comparisons of model runs with CO_2 emissions estimated from two distinct studies suggest. Even though the discrepancies between the two estimates are large (linear correlation coefficient of 0.2 and standard deviation of about 80% of the average values), the difference in the CO_2 increases in South America is only 0.1–0.2 ppm (the sources are very remote), well below the effect of the sources themselves. It was not possible to perform the same type of comparisons for other biomass-burning sources, because independent estimates were not available for those sources. This explains why our study focuses on north African savannas. Similar conclusions about the effect of southern African fires, however, are probably justified.

The vertical structure of the CO_2 increases due to biomass burning is quite different when the sources are local (South America) or remote (e.g., north African savannas). A pronounced maximum in the lower layers characterizes the effect of local sources and more homogenous profiles characterize the effect of remote sources (due to processes that take place during the transport from the source region). In the upper layers, therefore, remote effects may dominate.

No additional CO_2 sink(s) associated with the increased CO_2 emissions from biomass burning were included in the model simulations presented here due to our lack of knowledge in correctly specifying these sinks. To minimize any errors associated with the omission of these "extra" sink terms, the model was run with the biomass-burning sources for only 1 year after spin-up. As a result the seasonal cycle of CO_2 increase after 1 year may not be in equilibrium,

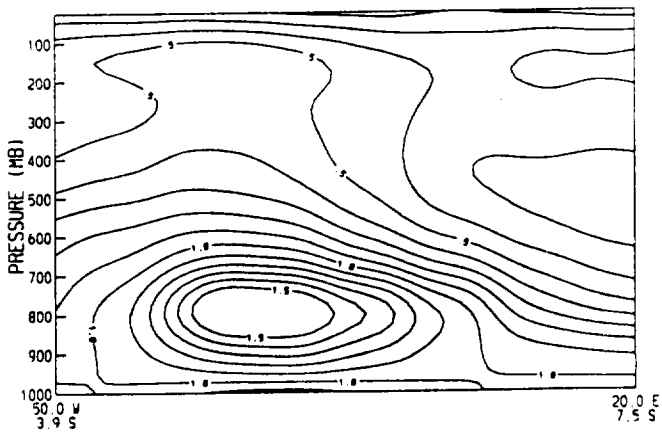

Figure 9. The vertical cross section of $dC(z)/dC(z = 0)$ along a path from 3.9°S–50°W to 7.5°N–20°E from model run NAS + SA. The data shown are a mean over the period January 25 to February 7.

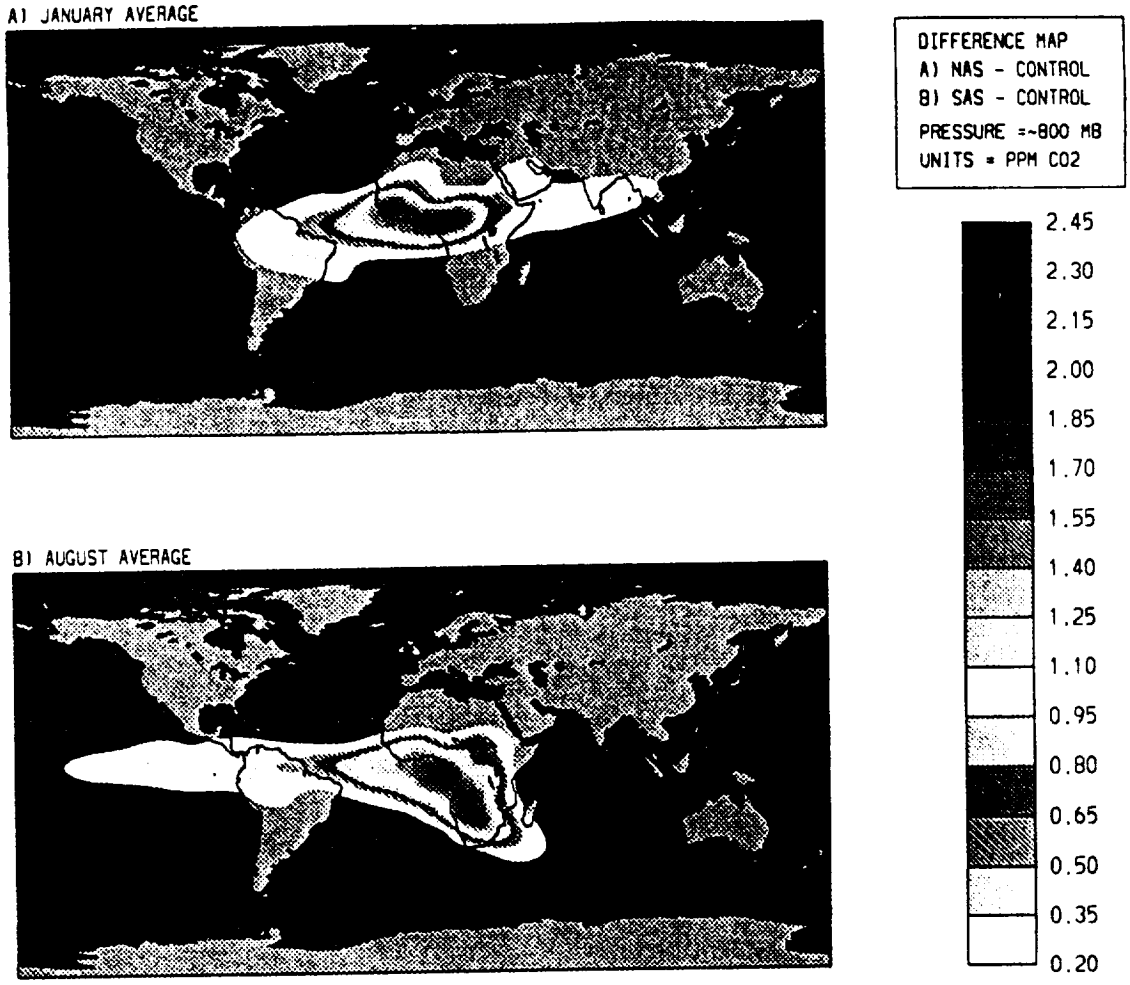

Plate 6. (a) The average difference during January between CO_2 concentrations (ppm) at 800 mbar from model run NAS and model run CONTROL. (b) The average difference during August between CO_2 concentrations (ppm) at 800 mbar from model run SAS and model run CONTROL.

particularly at grid points affected by emissions occurring at the end of the model year (September). Running the transport model with biomass-burning sources and sinks during several years after spin-up, until equilibrium is reached, would probably provide more realistic simulated CO_2 effects since biomass burning of the current magnitude, mostly resulting from human activity, has been occurring for many years. Nevertheless, our results are strongly indicative of the effects expected, which may not differ substantially from those obtained in the equilibrium state.

Acknowledgments. The authors thank Charles David Keeling of the Scripps Institution of Oceanography, La Jolla, California, for making available their transport model and Pierre-Yves Deschamps of the University of Lille, France, for helpful discussions. The comments and suggestions of M. O. Andreae, H. Cachier, J. G. Goldammer, G. Helas, J. P. Malingreau, A. Setzer and an anonymous reviewer greatly improved the original manuscript. This work has been supported by the National Aeronautics and Space Administration under grants NAGW-2727 and NAGW-2987, the Department of Energy under grant DE-FG03-90-ER61061, the University of California and Digital Equipment Corporation under research grant 1243, and by a consortium of government and industrial partners.

References

Andreae, M. O., R. W. Talbot, H. Berresheim, and K. M. Beecher, Precipitation chemistry in central Amazonia, *J. Geophys. Res.*, *95*, 16,987–16,999, 1990.

Boden, T. A., R. J. Sepanski, and F. W. Stos, Trends '91: A compendium of data on global change, *Publ. ORNL/CDIAC-46*, 665 pp., Carbon Dioxide Inf. Anal. Cent., Oak Ridge, Tenn., 1991.

Cahoon, D. R., Jr., B. J. Stocks, J. S. Levine, W. R. Cofer III, and K. P. O'Neill, Seasonal distribution of African savanna fires, *Nature*, *359*, 812–815, 1992.

Crutzen, P. J., and M. O. Andreae, Biomass burning in the tropics: Impact on atmospheric chemistry and biogeochemical cycles, *Science*, *250*, 1669–1678, 1990.

Delmas, R., A. Marenco, J. P. Tathy, B. Cros, and J. G. R. Baudet, Sources and sinks of methane in the African savanna: CH_4 emissions from biomass burning, *J. Geophys. Res.*, *96*, 7287–7299, 1991.

Fishman, J., V. G. Brackett, and K. Fakhruzzaman, Distribution of tropospheric ozone in the tropics from satellite and ozonesonde measurements, *J. Atmos. Terr. Phys.*, *54*, 589–597, 1992.

Hansen, J., G. Russell, D. Rind, P. Stone, A. Lacis, S. Ledebeff, R. Ruedy, and L. Travis, Efficient three-dimensional global models for climate studies: Models I and II, *Mon. Weather Rev.*, *111*, 609–662, 1983.

Hao, W. M., M. Liu, and P. J. Crutzen, Estimates of annual and

regional releases of CO_2 and other trace gases to the atmosphere from fires in the tropics, based on the FAO statistics for the period 1975–1980, in *Fire in the Tropical Biota*, edited by J. G. Goldammer, pp. 440–462, Springer-Verlag, New York, 1990.

Heimann, M., and C. D. Keeling, Aspects of climate variability in the Pacific and the western Americas, *Geophys. Monogr. Ser.*, vol. 55, edited by D. H. Peterson, pp. 237–275, AGU, Washington, D. C., 1989.

Houghton, R. A., J. E. Hobbie, J. M. Melillo, B. Moore, B. J. Peterson, J. R. Shaver, and G. M. Woodwell, The flux of carbon from terrestrial ecosystems to the atmosphere in 1980 due to changes in land use: Geographic distribution of the global flux, *Tellus*, *39*(B), 122–139, 1987.

Lanly, J. P., Tropical forest resources, *FAO Pap. 30*, Food and Agric. Organ., Rome, 1982.

Levine, J. S., Global biomass burning: Atmospheric, climatic, and biospheric implications, in *Global Biomass Burning*, edited by J. S. Levine, pp. xxv–xxx, MIT Press, Cambridge, Mass., 1991.

Loudjani, P., Cartographie de la production primaire des zones savanicoles d'Afrique de l'Ouest a partir de données satellitaires, Comparaison avec des données de terrain, Mem. de DEA en Ecol., Univ. de Paris-Sud, Orsay, France, 1988.

Menaut, J. C., L. Abbadie, F. Lavenu, P. Loudjani, and A. Podaire, Biomass burning in west African savannas, in *Global Biomass Burning*, edited by J. S. Levine, pp. 133–144, MIT Press, Cambridge, Mass., 1991.

Prospero, J. M., R. A. Glaccum, and R. T. Nees, Atmospheric transport of soil dust from Africa to South America, *Nature*, *289*, 570–572, 1981.

Razafimpanilo, H., Interprétation des campagnes physico-chimiques aéroportées dans la troposphère (STRATOZ-TROPOZ) par trajectographie de masse d'air et télédétection spatiale, PhD. thesis, 209 pp., Univ. Paul Sabatier, France, 1991.

Russell, G. L., and J. A. Lerner, A new finite-differencing scheme for the tracer transport equation, *J. Appl. Meteorol.*, *20*, 1483–1498, 1981.

Seiler, W., and P. J. Crutzen, Estimates of gross and net fluxes of carbon between the biosphere and the atmosphere from biomass burning, *Clim. Change*, *2*, 207–247, 1980.

Talbot, R. W., M. O. Andreae, H. Berresheim, P. Artaxo, M. Garstang, R. C. Harriss, K. M. Beecher, and S. M. Li, Aerosol chemistry during the wet season in central Amozonia: The influence of long-range transport, *J. Geophys. Res.*, *95*, 16,955–16,969, 1990.

Ward, D. E., R. A. Susott, J. B. Kauffman, R. E. Babbitt, D. L. Cummings, B. Dias, B. N. Holben, Y. J. Kaufman, R. A. Rasmussen, and A. W. Setzer, Smoke and fire characteristics for cerrado and deforestation burns in Brazil: BASE B experiment, *J. Geophys. Res.*, *97*, 14,601–14,619, 1992.

R. Frouin, S. F. Iacobellis, S. C. Piper, H. Razafimpanilo, and R. C. J. Somerville, Scripps Institution of Oceanography, Climate Research Division, 9500 Gilman Drive, Department 0224, La Jolla, CA 92093-0224.

(Received July 14, 1993; revised November 9, 1993; accepted November 23, 1993.)

- APPENDIX 2 -

"Estimating Burned Area from AVHRR Reflectance Data"
H. Razafimpanilo, R. Frouin, S. F. Iacobellis, and R. C. J. Somerville
Rem. Sen. Environ., to be submitted

ESTIMATING BURNED AREA FROM AVHRR REFLECTANCE DATA

Herisoa Razafimpanilo*, Robert Frouin*
Samuel F. Iacobellis+, Richard C. J. Somerville+

Scripps Institution of Oceanography
University of california San Diego
La Jolla, California

(*Remote Sensing of the Environment,* to be submitted)

August 1994

*California Space Institute
+Climate Research Division

ABSTRACT

Two methods to determine burned area from Advanced Very High Resolution (AVHRR) data are described. The first method, or the "linear method" employs AVHRR channel 2 (0.68-1.09 μm) reflectance and is based on the nearly linear relationship $P=f(R_2)$ between percentage of pixel burned, P, and channel 2 reflectance, R_2. The second method, referred to as the "non-linear" method, employs the Normalized Difference Vegetation Index (NDVI) derived from AVHRR channel 1 and channel 2 reflectances. The coefficients of the non-linear equation $P=f(NDVI)$, a polynomial of degree 2, are found to be a function of the NDVI of the background before the fire event. Radiative transfer simulations indicate that the linear method, unlike the non-linear method, must be applied to top-of-atmosphere reflectances that have been corrected for atmospheric influence. Theoretical studies suggest that the methods are subject to some limitations. To avoid discontinuity problems, the initial background (just before the fires) must be characterized by an AVHRR channel 2 reflectance above 9% and by a positive NDVI. To separate the useful signal from atmospheric effects, the fire scar must occupy at least 12 and 20% of the pixel size in the case of savanna and green vegetation (e.g., forest), respectively. For the average fire scar of 0.88 km^2 characteristic of African savannas, Low Area Coverage (LAC) data at 1 km resolution are adapted to the problem, but not Global Area Coverage (GAC) data at 4 km resolution. Using GAC data, the fire scar must occupy at least 3 km^2 to yield accurate estimates of burned area. The error on the percentage of area burned due to calibration of $P=f(R_2)$ is typically 10%. An additional 10% error is due to uncertainties in the reflectance of the totally burned area taken as a reference. When applied to homogeneous pixels, the mean relative error on the percentage of area burned is about 20% for the linear method and 10% for the non-linear method. The linear method gives better results for heterogeneous pixels, but both methods cannot be used when the pixel contains low reflectance backgrounds (e.g., water).

1. INTRODUCTION

It is well recognized that global fire activity needs to be monitored closely, because of its potential impact on climate and the environment, (Levine, 1991). In recent years, satellite remote sensing and field works have been combined to study the varied aspects of biomass burning, but mostly on a local scale (Goldammer, 1990; Levine, 1991). Currently, joint efforts are being developed by the international scientific community to identify a research program that will improve satellite fire monitoring, provide global fire detection products, and quantify the effects of fires (atmospheric chemistry, climate, deforestation, ecology). In this context, several interdisciplinary projects have been or are being carried out, namely the Transport and Atmospheric Chemistry Experiment - Atlantic (TRACE-A), the Dynamique et Chimie Atmosphérique en forêt Equatoriale (DECAFE), the Southern Africa Fire/ Atmosphere Research Initiative (SAFARI), the Savanne à Long Terme (SALT) (see Delmas, 1990 for a description of these programs), and the Fire In global Resource and Environmental monitoring (FIRE), a project of the Commission of the European communities, Joint Research Centre (Malingreau, 1993, personal communication).

Biomass burning studies are lacking quantitative information on the spatio-temporal variability of fires at regional and global scales. Applying local results to larger scales may give a rough idea of the global fire patterns (i.e., distribution of fires, amount of area burned, and carbon emission rates), but such a generalization brings significant inaccuracy to the estimates (Hao et al. 1990; Menaut et al. 1991; Iacobellis et al. 1994). Ground-based observations are not conceivable on very large scales, making it necessary to exploit the capabilities of earth-observing satellites, which appear as a solution to the in-situ sampling problem. Satellite-based techniques, however, require ground-based measurements to evaluate their performance.

Fire-related studies using satellite data include obtaining pre-fire information (e.g., vegetation fuel content), detecting active fires and smoke plumes, and obtaining post-fire information (e.g., burned areas, vegetation regeneration). In the last ten years, several studies have demonstrated the utility of remote sensing to fire monitoring. Various remote sensing systems, including the AVHRR aboard NOAA, the TM and MSS aboard LANDSAT, the HRV aboard SPOT, the VAS aboard GOES, the VISSR aboard DMSP, and the SAR aboard ERS-1 and JERS-1 can be used. Justice et al. (1993) have discussed the

potential and limitations of these systems and have outlined the current trends in this field of research. Robinson (1991) has reviewed the problems related to the detection of fire signals, instrumentation, and atmospheric interference. The choice of satellite depends on the extent and spectral characteristics of the fire signal. The high cost of the data, as well as their low frequency in time, limit to local monitoring the use of high resolution radiometers such as TM and HRV. The AVHRR provides daily data that are adapted to regional studies. Kennedy (1992) has recently discussed the ability of AVHRR to detect fires. Local Area Coverage (LAC) data at 1 km resolution and sampled Global Area Coverage (GAC) at 4 km resolution are available for this purpose. GAC data are more convenient to use on a global scale, but they are not recommended for quantitative studies related to fires (Kennedy et al. 1993).

The detection of active fires is usually accomplished with thermal infrared sensors. The technique is based on the sensitivity of the 3-5 μm window to fire radiative energy, and also on the sensitivity of the thermal 8-12 μm window to high temperature. Owing to the amplification of the fire signal at 3.7 μm, fires occupying even a small fraction of the pixel can be detected, allowing the use of low resolution satellites, such as NOAA, to detect

active fires. However, limitations exist due to saturation of the detectors, obscuration by clouds or smoke, and confusion with other bright targets (see Robinson, 1992 for a comprehensive review of fire detection using infrared remote sensing). Various methods have been developed to enhance the detection capability (Matson and Holben, 1987; Lee and Tag, 1990; Malingreau, 1990; Kaufman et al., 1990; Brustet et al., 1991; Langaas, 1993; Franca et al., 1993; Kendall, 1993). Images acquired at night may be used to detect active fires (Langaas, 1992), but the results might not represent the actual burnings since biomass burning can be masked by effects due to nocturnal weather conditions (Langaas, 1993b). Nevertheless, studies such as those of Cahoon et al. (1992), who processed DMSP night time images of Africa, suggest that useful information on the temporal and spatial distribution of fires can be obtained using available techniques.

While the detection of active fires has been studied extensively in recent years (e.g., IGBP,1992), much less research has focused on the spectral characteristics of burn scars and the areas actually burned. Matson and Dozier (1981) described a method to deduce sub-pixel fire size and temperature using LAC data. Since this method relies on the accurate knowledge of the

background surface temperature of the pixel affected by fire, its use is limited to local scales. Pereira et al. (1991) used AVHRR fire counts to estimate burned areas from active fires assuming that the fire occupies the entire pixel. Their results, when compared to those from higher resolution TM images, show an overestimate of the fire size by 43% on average and an underestimate of the fire size for long, continuously burning fires.

After a fire, the area burnt is covered by ash and appears darker. This results in changes of the top-of-atmosphere radiance at visible, near-infrared and thermal infrared wavelengths, as well as in the derived NDVI, providing the basis of methods to detect burned areas from space. Studies have shown that MSS data (Lavenu, 1984; Tanaka et al., 1993) or TM data (Chuvieco and Congalton, 1988; Pereira and Seltzer, 1993) can be used to identify burned areas. Discrimination between burned and unburned areas, however, is limited by other surfaces that give a similar response than burned surfaces (i.e., water) and, in the case of savanna ecosystems, by the rapid regrowth of vegetation just a few days after the fire (Langaas, 1989; Frederiksen et al., 1990). For such ecosystems, the studies suggest that data should be used with higher frequency in time (e.g., once a day). Radiances in the visible and near-infrared channels of

AVHRR (channels 1 and 2, respectively) and the derived NDVI have been used in Senegal, and were found sensitive to fire-affected areas. A net decrease in the reflectance of AVHRR channel 2 has been observed by Malingreau (1990) in the Central Congo Basin. AVHRR LAC data have also been used to study burned areas in Boreal forests, where burned scars remain longer (several months) after the fire event (Kasischke et al., 1992).

The existing techniques to estimate burned areas, when applied to coarse resolution satellites, assume that a pixel is either totally burned or totally unburned. The burned area is then estimated visually or numerically, by counting the number of pixels classified as burned or unburned. The procedure is accurate for fire extents larger than the satellite resolution (Lavenu, 1984; Kasischke et al., 1992), but becomes unreliable when a large number of partially burned pixels is present within a scene, which is often the case with coarse resolution sensors. There is a need to explore and develop schemes that treat partially burned pixels properly, in order to enhance the accuracy of burned area estimates.

In the present study, we describe and discuss methodologies to estimate burned areas using data from AVHRR-type sensors. We focus on savanna fires

because of their large contribution to carbon dioxide and trace gas emissions to the atmosphere (e.g., Hao et al. 1990; Menaut et al. 1991), but the methodologies proposed may also be applicable to other types of ecosystems (e.g., forests). The methodologies utilize either near-infrared radiances or derived NDVIs, quantities that have been shown to be sensitive to fire scars (see the above references). They result from simulations of the top-of-atmosphere signal for varied pixel characteristics, taking into account the contribution of partially burned pixels. The effects of factors such as atmospheric influence, pixel heterogeneity, and ground resolution are investigated, not only to devise the best strategies regarding the retrieval of area burnt, but also to quantify the accuracy of the estimates and assess the general applicability of the algorithms. Test calculations using actual satellite data, necessary to validate the theoretical findings, are not presented in this article (Part I of a 2-part series). They are the object of Part II (Razafimpanilo et al. 1994), which reports on results obtained with AVHRR data acquired over West African savannas.

2. SIMULATIONS AT THE TOP OF THE ATMOSPHERE

The purpose of this section is to examine the influence of the atmosphere conditions and viewing geometry on burned-area detection. At visible and near-infrared wavelengths, satellite radiances or, equivalently, reflectances are affected by scattering and absorption by atmospheric gases and aerosol particles. These processes modify the contrast between burned and unburned targets, when these targets are viewed from the satellite altitude. Furthermore, their effect is variable with atmospheric composition and solar and viewing angles. The question is: do atmospheric characteristics impact significantly the difference between radiometric signals originating from the two types of target? Depending on the answer, strategies may be devised to perform atmospheric corrections that yield accurate burned-area estimates.

The top-of-atmosphere reflectance in AVHRR channels 1 and 2 and the derived NDVIs of a totally burned area and its unburned background, savanna or green vegetation, are simulated using the Simulation of the Satellite Signal in the Solar Spectrum (5S) code (Tanré et al. 1990). Modeling of the atmospheric effects in the 5S code includes absorption by atmospheric gases and aerosols, scattering by molecules and aerosols, and interaction between the two

processes. The simulations are expected to provide information on our ability to distinguish a totally burned area from its background, taking into account the presence of the atmosphere while keeping in mind that intermediate values of reflectances (or NDVI) may correspond to partially burned areas. The two extreme values of reflectance or NDVI (totally burned and unburned areas) must be distinct in order to determine partially burned areas within a satellite pixel.

The 5S code requires a knowledge of the target's ground reflectance at the appropriate wavelengths. We used values reported by Frederiksen et al. (1990), who measured in Senegal the ground reflectance of both a totally burned area and savanna within wavebands close to those of AVHRR channels 1 and 2. During the first day of fire, the reflectance of burnt areas observed in the red and near-infrared were low, about 5.4% and 5.9%, respectively. Such low values, i.e. 4% and 4.9%, respectively, were also observed by Vickos et al. (1988) in Ivory coast. Both experiments revealed a sharp reflectance decrease immediately after the fire, and a reflectance increase a few days after the fire. In the simulations presented below, the reflectance of savanna used as background reference is 12.1% in channel 1 and 18.9% in channel 2

(Frederiksen et al. 1990). These values are similar to those measured by Vickos et al. (1988) just before fire events. As for the surface reflectance of green vegetation, we use 10.4% and 51.8% in the red and near-infrared, respectively, values provided by the 5S code.

The variations of reflectance and NDVI with atmospheric visibility (changing from 5 to 25 km), aerosol type (continental or maritime), water vapor content (changing from 0 to 6 g/cm^2), and view angle (changing from 0 to 50º) are computed for three different types of homogeneous targets (totally burned area, savanna, and green vegetation). In all the simulations, the sun zenith angle is fixed at 30º and the relative azimuth angle is 90º. The selected ranges for the atmospheric and geometric variables represent the variability expected in tropical Africa, although values outside those ranges may occasionally be encountered. Figures 1 (a-c), 2 (a-c), and 3 (a-c) display the results of the top-of-atmosphere simulations (thin lines) together with the surface values (thick lines) for channel 1, and channel 2, respectively, and NDVI. The standard conditions used for the non-varying parameters are indicated are: a visibility of 15 Km, a water vapor content of 4.1 g/cm^2, a view angle of 30º, and continental-type aerosols.

To facilitate the discussion, the difference between the reflectance or NDVI of the background and the reflectance or NDVI of a totally burned area (top-of atmosphere and surface) are also formed and normalized by the surface reflectance or NDVI of the background. The relative differences obtained for channel 1, channel 2, and NDVI are displayed in Table1. The minimum and maximum values at the top of the atmosphere are for all the atmospheric conditions considered (see above).

The relative difference in channel 1 reflectance is lower than the relative difference in channel 2 reflectance and in NDVI (Table1). The highest difference in channel 1 reflectance is obtained at the surface for savanna, and is only 55% of the background reflectance. The corresponding difference in channel 2 reflectance, the surface value of the relative difference is 69% for savanna and 89% for green vegetation. For NDVI, the figures become 80% and 93%, respectively. In the case of channel 1 and 2, the relative contrast is degraded at the top of the atmosphere, with relative differences lower than those at the surface by factors ranging between 0.6 and 0.9. Since the actual reflectance of the background is small in channel 1 compared to that in channel 2 (Figures 1 and 2), the absolute contrast (in reflectance) is too small in channel

Surface Type	Parameter	$(Y_{bg}-Y_{bn})/Y_{bgo}$		
		Surface	Top-of-Atmosphere	
			Min	*Max*
SAVANNA	CH 1 reflectance	55.4%	33.1%	47.9%
	CH 2 reflectance	68.8%	40.7%	58.7%
	NDVI	79.8%	83.3%	106.7%
GREEN VEGETATION	CH 1 reflectance	48.1%	28.8%	41.3%
	CH 2 reflectance	88.6%	54.4%	77.4%
	NDVI	93.4%	98.3%	106.2%

Table 1: *Relative difference between the reflectance or NDVI of the background (savanna or green vegetation), Y_{bg}, and of a totally burned area, R_{bn}. The normalization factor is the reflectance or NDVI at the surface (no atmosphere), Y_{bgo}. Minimum and maximum values obtained for a wide range of atmospheric conditions and radiation geometries (see text) are given, as well as the values at the surface.*

1. In fact, the atmospheric effects in channel 1 are similar in magnitude to the reflectance of the background and burned area, making it difficult to distinguish the two types of surface. Interestingly, the atmospheric effects of the burned area reflectance are negligible in channel 2 (Fig. 2). These negligible effects result from the compensating influence of scattering by the atmosphere (tends to increase the top-of-atmosphere signal) and attenuation along the sun-atmosphere-surface-satellite path (tends to decrease the top-of-atmosphere signal). Using channel 2, the atmospheric conditions that give the best contrast correspond to visibilities above 15 km, water vapor content below $3 g/cm^2$, view angle below 25º, and maritime-type aerosols. The contrast is affected in decreasing order by visibility, satellite view angle, aerosol type, and water vapor content. In the case of NDVI, the relative contrast at the top of the atmosphere is comparable to the one at the surface, but higher, and may exceed 100% (see Table 1). Thus, atmospheric conditions tend to amplify the contrast between the NDVI of the background and the NDVI of a totally burned area. Values for green vegetation are generally higher than those for savanna. Unlike the channels 1 or 2 reflectance contrast, the NDVI contrast varies little with atmospheric characteristics. The atmospheric influence depends in

decreasing order on visibility, aerosol type, water vapor content, and view angle.

According to above simulations, channel 2 and NDVI are more suitable than Channel 1 to detect burned areas without atmospheric corrections. The channel 2 reflectance and the NDVI of a totally burned area can be easily distinguished from the reflectance and NDVI of the background. In channel 1, the difference between the reflectance of a burned area and that of its background, either at the top of the atmosphere or on the ground, is too low to allow meaningful burned area estimates. The effect of the atmosphere, related to the conditions studied, may be large in channel 2 for the typical backgrounds considered, but remains practically negligible for burned areas. However, for some extreme conditions, $\theta_S = 60^\circ$, $\theta_V = 50^\circ$, and visibilities below 10 km, the effect of the atmosphere is not negligible, and the top-of-atmosphere channel 2 reflectance of a totally burned area may exceed 10%. For the same geometrical conditions and higher visibilities, the top-of-atmosphere channel 2 reflectance of a totally burned area remains below 10%. The NDVI contrast between background and burned area does not appear to depend significantly on atmospheric characteristics. These findings are instrumental to devise

strategies regarding burned area retrieval. Because of the channel 1 limitations, the remainder of the study will focus on methodologies using channel 2 and/or NDVI.

3. METHODOLOGIES TO ESTIMATE PERCENT OF AREA BURNED

In this section, two methods to estimate percent of area burnt are described and evaluated. One method utillizes the channel 2 reflectance, the other the NDVI. The background is assumed to be either savanna, green vegetation, or a combination of both. Pixels containing both savanna and green vegetation, however, are considered homogeneous. The effect of background heterogeneity is investigated in a separate section (section 4.1).

3.1. Linear method using AVHRR Channel 2 reflectance

3.1.1. Description

Vickos (1986), using TM data averaged over 1 km^2, has shown that the relationship between reflectance in the near infrared band (~0.85μm), R_2, and percentage of area burned, P, is nearly linear. This is not surprising since, to a good degree of approximation, the top-of-atmosphere reflectance is proportional to the number of burned TM pixels within the 1 km^2 area (effects

of contrast between burned and unburned pixels are secondary). This linearity provides the basis for the method developed in this study to estimate P from AVHRR channel 2 data. Once the relationship $R_2=f(P)$ is determined, P can be estimated from the reflectance R_2 measured after the area has burned.

Determination of the relationship $R_2=f(P)$, either at the surface (reference) or at the top of the atmosphere (simulated by 5S), requires knowledge of two R_2, P pairs. We assume that the abscissa 0% of area burned corresponds to an ordinate characterizing the background (first pair), and that the abscissa 100% of area burned corresponds to an ordinate characterizing a totally burned surface (second pair). The reflectance of the background is obtained from Eq. (4), and remains constant in the calculation of the reflectance of the area burned (Eq. 2). Figure 4 shows how the linear function $R_2=f(P)$ depends on atmospheric conditions. The large variation in the slope of the curves suggest that $R_2=f(P)$ has to be determined for each case. In other words, the relationship $R_2=f(P)$ needs to be calibrated in order to be applicable 1) to varied atmospheric and viewing conditions and 2) to varied types of initial backgrounds.

To calibrate $R_2=f(P)$, a knowledge of the reflectance of the totally burned area, and of the unburned, initial background is necessary. In practice, the latter is directly deduced from the data available over the target prior to the fire event. This approach is not suitable, however, because (1) a totally burned area is not easy to find and to classify in the satellite imagery and (2) its reflectance may vary with geometric and atmospheric conditions (Figs. 2 and 4). Since the channel 2 reflectance of a totally burned area in the absence of atmosphere is known and can be considered as constant irrespective of the nature of the initial cover, it is taken as a reference. All the top-of-atmosphere measurements (initial background, burned area) are then transformed to surface reflectances or, in other words, are corrected for atmospheric effects.

Detailed information about aerosol amount and type and water vapor amount is needed to perform optimum atmospheric corrections. In-situ data can be used as input to the models, but are not always available over large regions. Climatological data can be used instead, but they might not be representative of a specific time and location, leading to incorrect results. The errors due to inadequate atmospheric corrections must therefore be calculated to evaluate the accuracy of the method. For that purpose, standard atmospheric

corrections (i.e., using the characteristics of a typical atmosphere) are performed on channel 2 reflectance simulated for a wide range of atmospheric conditions. The resulting errors in the relationship $R2=f(P)$ and, hence, the estimated P, are then quantified (see below).

3.1.2. Evaluation

Atmospheric corrections on the simulated data set are performed using the 5S code (Tanré et al., 1986). In this code, the top-of-atmosphere reflectance is expressed as:

$$R^* = \{R_a + [R_S/(1-R_S S_a)]\ T_a\} T_g \qquad (1)$$

where R^* is the apparent reflectance, R_a is the Rayleigh aerosol reflectance, R_S is the surface reflectance, S_a is the spherical albedo of the atmosphere, T_a is the scattering transmittance, and T_g is the gaseous transmittance. The R_a, T_a, S_a, and T_g functions computed by the 5S code do not depend on surface reflectance R_S, they vary only with the characteristics of the atmosphere. As a result, inversion of Eq. (1) is possible, allowing one to estimate the surface reflectance R_S from the apparent reflectance R^* for given atmospheric conditions. Since the

actual atmospheric conditions are not known at the time of the measurements, a standard tropical atmosphere is used to compute the atmospheric functions and invert Eq. (1) for each geometrical condition in the simulated dataset. The standard atmosphere is characterized by continental aerosols, a water vapor content 4.1 $g.cm^{-2}$, and a visibility of 15 Km.

The simulated dataset includes cases of visibility ranging from 5 to 25 km, continental and maritime aerosols, water vapor content ranging from 1 to 5 $g.cm^{-2}$, viewing zenith angle varying from 0 to 50º, and sun zenith angle ranging from 0 to 60º. The calculated slopes are compared to the initial slope on the surface without atmosphere, respectively for savanna and green vegetation. Table 2 gives the minimum and the maximum values of the ratio between the calculated slope and the slope on the surface. Figure 5 illustrates the results obtained for savanna and green vegetation with and without atmospheric effects. In all the cases, the presence of the atmosphere tends to attenuate the initial (surface) slope by a factor of at least 0.87. The smallest ratios, about 0.6, corresponding to a maximum attenuation of the slope, are obtained for low visibilities, continental type aerosols, high water vapor content and high solar and viewing angles.

	CALCULATED SLOPE/SURFACE SLOPE (Min - Max)	
PARAMETERS (range of variations)	SAVANNA	GREEN VEGETATION
Visiblility (5-25 km)	0.59 - 0.73	0.61 - 0.73
Water vapor (1 - 5 $g.cm^{-2}$)	0.69 - 0.77	0.70 - 0.79
Aerosol type (C -M)	$0.59 - 0.77^{c}$	$0.61 - 0.79^{c}$
	$0.67 - 0.81^{m}$	$0.69 - 0.83^{m}$
View angle (0° - 50°)	$0.67 - 0.73^{(0°)}$	$0.69 - 0.74^{(0°)}$
	$0.67 - 0.71^{(30°)}$	$0.68 - 0.73^{(30°)}$
	$0.60 - 0.64^{(60°)}$	$0.62 - 0.66^{(60°)}$

Table 2: *Minimum and maximum values of the ratio between the calculated slope at the top of the atmosphere and the slope on the surface for different atmospheric and geometrical conditions. The range of the variations of atmospheric and geometrical conditions are indicated in parenthesis in the first column. The variations with aerosol type include the variations of the other parameters in the first column. Standard values are taken for undisplayed values of parameters. The variations with the view angle were calculated for different values of the solar zenith angle (θ_S= 0, 30, and 60°). (c): continental aerosols, (m): maritime aerosols.*

The errors in the calibration of $R_2=f(P)$ are related to errors due to inadequate atmospheric corrections. As suggested and described in the first section, the calibration of $R_2=f(P)$ consists in (1) assuming that the reflectance of a totally burned area (100% burned) without atmosphere is constant (2) correcting the measured reflectance of the background (0% burned) from atmospheric and geometrical effects, and (3) joining the two R_2, P points (background and totally burned area) to get $R_2=f(P)$. Standard atmospheric corrections do not permit retrieval of the actual reflectance of the background without atmosphere. Errors due to atmospheric corrections lead to errors on $R_2=f(P)$. To quantify these errors, top-of-atmosphere reflectances of savanna and green vegetation, for which optical proprieties are known, are first simulated by the 5S code for various conditions. The simulated reflectances are corrected for standard atmospheric effects by inverting Eq. (1) as described above. The corrected reflectances, as well as the corresponding slopes, are finally compared with the initial surface reflectance and the surface slope, respectively. Extreme atmospheric and geometrical conditions are used to cover the error range and evaluate the maximum errors. Table 3 gives the reflectance R_c after atmospheric corrections, its deviation ΔR from the surface reflectance

SAVANNA

Solar zenith angle = 0°, View angle = 0°

Visibility (km)	H2O ($g.cm^{-2}$)	Aerosol type	R_C	ΔR (R_C-R_S)	ΔS (%) (S_C-S_S)	$\Delta S/S_S$ (%)
5.	1.	C	0.203	0.014	-0.144	10.5
5.	1.	M	0.240	0.051	-0.181	39.4
5.	5.	C	0.181	-0.008	-0.122	-6.4
5.	5.	M	0.215	0.026	-0.156	19.7
15.	1.	C	0.209	0.020	-0.150	15.1
15.	1.	M	0.232	0.043	-0.173	33.1
15.	5.	C	0.186	-0.003	-0.127	-2.3
15.	5.	M	0.207	0.018	-0.148	14.0
25.	1.	C	0.210	0.021	-0.151	16.1
25.	1.	M	0.229	0.040	-0.170	30.5
25.	5.	C	0.187	-0.002	-0.128	-1.4
25.	5.	M	0.204	0.015	-0.145	11.6
Mean				0.020	-0.150	15.0

Solar zenith angle = 60°, View angle = 50°

Visibility (km)	H2O ($g.cm^{-2}$)	Aerosol type	R_C	ΔR (R_C-R_S)	ΔS (%) (S_C-S_S)	$\Delta S/S_S$ (%)
5.	1.	C	0.237	0.048	-0.178	36.8
5.	1.	M	0.301	0.112	-0.242	86.3
5.	5.	C	0.203	0.014	-0.144	10.9
5.	5.	M	0.260	0.071	-0.201	54.6
15.	1.	C	0.217	0.028	-0.158	21.5
15.	1.	M	0.241	0.052	-0.182	39.7
15.	5.	C	0.185	-0.004	-0.126	-2.9
15.	5.	M	0.206	0.017	-0.147	13.2
25.	1.	C	0.215	0.026	-0.156	20.0
25.	1.	M	0.230	0.041	-0.171	31.6
25.	5.	C	0.184	-0.005	-0.125	-4.2
25.	5.	M	0.197	0.008	-0.138	6.0
Mean				0.034	-0.164	26.1

Table 3 (a): *Estimated error on the slope $\Delta S/S_S$ due to standard atmospheric corrections for different extreme conditions of visibility, water vapor content of the atmosphere, aerosol type (C: continental, M: maritime), and geometry. $\Delta S=S_C-S_S$ where Sc is the slope calculated after standard atmospheric corrections, S_S the surface slope. R_C is the reflectance corrected from atmospheric corrections. Its deviation ΔR from the ground reflectance R_S is given by ΔR ($\Delta R=R_C-R_S$). ($R_S=0.189$, $S_S=-0.0013$).*

GREEN VEGETATION

Solar zenith angle = 0°, View angle = 0°

Visibility (km)	H2O ($g.cm^{-2}$)	Aerosol type	R_C	ΔR (R_C-R_S)	ΔS (%) (S_C-S_S)	$\Delta S/S_S$ (%)
5.	1.	C	0.523	0.005	-0.464	1.1
5.	1.	M	0.604	0.086	-0.545	18.7
5.	5.	C	0.471	-0.047	-0.412	-10.3
5.	5.	M	0.544	0.026	-0.485	5.7
15.	1.	C	0.567	0.049	-0.508	10.6
15.	1.	M	0.609	0.091	-0.550	19.7
15.	5.	C	0.510	-0.008	-0.451	-1.7
15.	5.	M	0.548	0.030	-0.489	6.6
25.	1.	C	0.575	0.057	-0.516	12.4
25.	1.	M	0.607	0.089	-0.548	19.3
25.	5.	C	0.518	0.000	-0.459	0.0
25.	5.	M	0.547	0.029	-0.488	6.3
Mean				0.034	-0.493	7.3

Solar zenith angle = 60°, View angle = 50°

Visibility (km)	H2O ($g.cm^{-2}$)	Aerosol type	R_C	ΔR (R_C-R_S)	ΔS (%) (S_C-S_S)	$\Delta S/S_S$ (%)
5.	1.	C	0.519	0.001	-0.460	0.1
5.	1.	M	0.638	0.120	-0.579	26.1
5.	5.	C	0.453	-0.065	-0.394	-14.1
5.	5.	M	0.559	0.041	-0.500	9.0
15.	1.	C	0.581	0.063	-0.522	13.6
15.	1.	M	0.630	0.112	-0.571	24.4
15.	5.	C	0.508	-0.010	-0.449	-2.1
15.	5.	M	0.552	0.034	-0.493	7.4
25.	1.	C	0.598	0.080	-0.539	17.5
25.	1.	M	0.632	0.114	-0.573	24.7
25.	5.	C	0.524	0.006	-0.465	1.3
25.	5.	M	0.554	0.036	-0.495	7.8
Mean				0.044	-0.503	9.5

Table 3 (b): *Estimated error on the slope $\Delta S/S_S$ due to standard atmospheric corrections for green vegetation . (R_S=0.518, S_S=-0.00459). (cf Table 3(a))*

($\Delta R = R_C - R_S$), the calculated slope S_C, and the error $\Delta S/S_S$ on the calculated slope when compared with the surface slope S_S ($\Delta S = S_C - S_S$). Negative errors correspond to an underestimation of the reflectance, which translates into an underestimation of the slope, whereas positive errors correspond to an overestimation of the reflectance and slope. The slopes are generally overestimated by about 15 to 26% for savanna, and about 7 to 10% for green vegetation. The highest errors correspond to small visibilities, small water vapor content, and maritime type aerosols.

As shown above, the calibration of $R_2 = f(P)$ using atmospheric corrections for a standard or climatological atmosphere introduce errors in the calibration of $R_2 = f(P)$ at the surface. The corrected top-of-atmosphere reflectances (initial background and area burned) are subject to errors because the standard atmospheric corrections applied do not take into account the real conditions at the time of observations. Since two independent successive observations are needed to apply the method, the reflectance of the area burned corrected for atmospheric effects does not necessarily correspond to the calibrated equation $R_2 = f(P)$ (atmospheric conditions may have changed between the observations). Errors then result in the determination of the percentage of area burned. To

quantify these errors, the maximum absolute error on the percentage of area burned is calculated as a function of the error on the slope, compared to the surface slope. When the slope is underestimated, we assume that the maximum error on the percentage of area burned is given by Δp_u (Fig. 6). When the slope is overestimated the maximum error is given by Δp_o. Figure 7 displays the maximum error on the percent of area burned as a function of the error on the slope determined (doted lines). Note that an overestimation of the slope by 100% leads to an error of only 50% on area burned. When the slope is overestimated, the error on area burned becomes 100% when the reflectance goes infinity. When the slope is underestimated, the corresponding error on area burned is linear. The maximum errors on the slope obtained from Table 3 are reported in Figure 7 (thick curves). Since the slopes are usually overestimated, we see that the errors are higher for initial backgrounds with lower reflectances (e.g., savannas). The maximum error on the percentage of burned area estimates, linked to differences in the atmospheric conditions of successive observations, does not exceed 45% (Fig.7). This error corresponds to extreme atmospheric and geometrical initial conditions (visibility: 5 km, water vapor content: 1 $g.cm^{-2}$, maritime aerosols, $\theta_S=60^\circ$, $\theta_V=50^\circ$). When two

observations giving two extreme errors are compared, R_C=0.301 and R_C=0.181 in Table 3(a) and R_C=0.638 and R_C=0.453 in Table 3(b), instead of compared to the surface, the corresponding maximum errors are about 50% and 30%, respectively, for savanna and green vegetation. Both pairs of observations generally correspond to extreme geometrical conditions (θ_S=60°, θ_V=50°). Between each pair of observations, the visibility is poor (5 km), the water vapor content changes from 1 to 5 g.cm^{-2}, and there is a change in the aerosol type (maritime to continental). Since successive observations are made within a few days, we assume that these cases are unrealistic in practice, unless very rare.

The mean errors on the slope estimate, about 20% for savanna and 8% for green vegetation, correspond to errors on the percent of area burned of about 15 and 5%, respectively. An additional error of about 10% may be added to the estimate of the percentage of burned area, due to the uncertainty on the reflectance of a totally burned area taken as a reference.

Assuming a percentage P_{true} of the area is burned, the corresponding reflectance is calculated at the top of the atmosphere for given atmospheric conditions. Standard atmospheric corrections are performed on the calculated

reflectance as well as on the reflectance of the unburned initial background. The method using channel 2 is applied to estimate the percentage of area burned, P_{cal}. In Fig. 8, P_{cal} is plotted as a function of the initial percentage, P_{true}, for different atmospheric and geometrical conditions. Since we assume that atmospheric conditions are the same before and after burning, the reflectance is unchanged when the background is unburned (p=0), and the initial percentage is retrieved (no error). The maximum difference between the percentage calculated, P_{cal}, and the initial percentage applied, P_{true}, is about 25% of the initial percentage for mean geometrical conditions (θ_S= 0º, θ_V= 0º, θ_S= 30º, θ_V= 30º), and about 45% for extreme geometrical conditions (θ_S= 60º, θ_V= 50º). Maximum relative differences corresponding to low percentages (below 20%) are 5% higher than of higher percentages.

The validity of the linear method is limited by the ability to distinguish a burned area from its background. For the method to be applied, it is necessary that a reflectance change due to burning is distinguished from that due to fluctuations of the background signal caused by atmospheric effects. Below a channel 2 reflectance limit (initial background), determined by the fluctuations of the signal due to incorrect atmospheric corrections, it is not possible to get

accurate results. The mean standard deviation of these fluctuations, mainly due to the change in atmospheric and viewing conditions between two observations, is calculated for each background type and added to the surface reflectance of a totally burned area to get the channel 2 reflectance limit of the initial background. Depending on the type of background considered, savanna or green vegetation, the limit represents 10 to 15% of its initial reflectance. These percentages correspond to a limit of about 0.03 and 0.05 for savanna and green vegetation, respectively. Thus the linear method is only applicable for initial backgrounds with a channel 2 reflectance above 0.09. This threshold eliminates initial background reflectances that are lower than the reflectance of a totally burned area. In that case, a change in the slope sign occurs, and the validity of the method becomes questionable.

3.2. Non linear method using AVHRR-derived NDVI

3.2.1. Description

The NDVI of a given background is calculated as a function of the percentage burned P, varying from 0 to 100%. The background is supposed to be homogeneous and composed by savanna, green vegetation, or a mixture of

both. The first step of the calculations consists in evaluating the reflectances in both channels 1 and 2, as a function of P:

$$R_i(p) = p*Rbn_i + (1-p)*Rbg_i \quad (2)$$

where Rbn_i (i=1,2) is the reflectance of a burned area in channel i, and Rbg_i (i=1,2) is the reflectance of the homogeneous background in channel i. Rbg_i can be expressed as:

$$Rbg_i = (1-\alpha)Rsv_i + \alpha\, Rvg_i \quad (3)$$

where Rsv_i and Rvg_i are respectively the reflectance of savanna and the reflectance of green vegetation in channel i, respectively, and α is the portion of green vegetation ($0<\alpha<1$).

The NDVI as a function of p is then computed from (2) as:

$$NDVI(p) = (R_2-R_1)/(R_2+R_1) \quad (4)$$

Extreme conditions of visibility, geometry, and water vapor content of the atmosphere are used to simulate the effects of the atmosphere on the results. These results, displayed in Figure 9, show the non-linearity of the equation p=f(NDVI), and the possible effects of the atmosphere for a given background.

Atmospheric effects are not negligible for the same type of background. However, eventual atmospheric corrections may introduce errors in the calculations, since a slight change in the reflectances value in either channel leads to a large change on the NDVI value. The latter is particularly justified for very low reflectance areas such as totally burned areas. Note that on the ground, a change of 15% in the channel 2 reflectance leads to a change of about 200% in the NDVI value. In addition to that, the NDVI of a totally burned area on the ground is not well known, and the fact that two channels are involved for atmospheric corrections may bring additional errors. As a result, atmospheric corrections are not conceivable and not recommended when using this method. Although the effects of the atmosphere are not negligible on the NDVI values, the shapes of the curves seem to be a function of the background NDVI (NDVI for p=0).

A large number of atmospheric and viewing conditions are considered to calibrate the relationship between the percentage of area burned and the NDVI. The simulated data were fitted by the following two dimensional equation:

$$p(NDVIbn) = A_0 + A_1 * NDVIbn + A_2 * NDVIbn^2 \qquad (5)$$

where NDVIbn is the NDVI of the burned area (which is equal to the NDVI of the background for p=0), A_0, A_1, and A_2 are the coefficients of the second-order polynomial to be determined as a function of the NDVI of the background. Figure 10 (a-c) show the variation of these coefficients as a function of the background NDVI for three viewing conditions and for extreme atmospheric conditions. The effects of geometrical conditions are outlined in Figures 10 (a), (b) and (c). The discrepancy of the coefficient values (A1 and A2) for low background NDVI suggests that the method may not be valid below a limit to be determined. The simulated coefficients A_0, A_1, and A_2, to be determined theoretically, are described respectively by polynomials, of order four (Fig.10(a)), three (Fig. 10(b)), and two (Fig. 10(c)) in NDVIbg, the NDVI of the background before the fire.

The coefficients of the polynomials are obtained by fitting the results of the simulations (see Figures 10(a), (b) and (c)). We assume that these relationships may be valid for all types of background.

3.2.2. Evaluation

Since no atmospheric corrections are needed to apply the nonlinear method, its evaluation is limited to the effect of the atmosphere on the determination of the percentage of area burned. As for channel 2, the percentage calculated, P_{cal}, after applying the method is compared to the initial percentage applied, $Ptrue$. The method using NDVI relies on the nonlinear relationship p=f(NDVI), which coefficients are a function of the NDVI of the background (see Fig. 10). Since these coefficients are obtained by fitting the results from different atmospheric and geometrical conditions, the error obtained using the method will vary with each individual condition. For each individual condition, the NDVI of the burned area (NDVIb) is calculated from Eq. (2), (3), and (4), with p=P_{true}). The NDVI of the background before the fire (Eq.(4)) allows to determine the coefficients A0, A1 and A2 from Fig. 10. The percentage P_{cal} is then deduced from Eq.(5), where p(NDVIb)=P_{cal}. Figure 11 displays P_{cal} as a function of P_{true}, with the same atmospheric and geometrical conditions as for channel 2 (Fig. 7). The relative maximum differences between P_{cal} and P_{true} are generally lower than of the linear method. These maximum differences are up to 60% of the initial percentage applied for low percentages burned (below 20%), but decrease to 10% when the percentage burned is above

80%. When the percentage burned ranges between 30 and 70%, the relative maximum difference is about 15% (25% for the linear method) for mean geometrical conditions (θ_S= 0º, θ_V= 0º, θ_S= 30º, θ_V= 30º), and ranges from 30 to 40% (45% for the linear method) for extreme geometrical conditions (θ_S= 60º, θ_V= 50º).

The mean deviations of the percentages calculated from the initial percentages applied are calculated as a function of the initial percentage burned as follows:

$$M.D= [\Sigma (P_{cal}-P_{true})^2]/N \qquad (6)$$

where N is the number of atmospheric conditions considered for each percentage. The mean deviations obtained are calculated relatively to the initial percentage applied, for both methods, and reported in Fig. 12. This Figure shows that even if the maximum deviation corresponding to the nonlinear method is usually lower than of the linear method, the mean deviations are higher when using the nonlinear method for low percentages. The linear method gives better results for low percentages burned, and for the same aerosol type as the one used for standard atmospheric corrections (continental aerosols). For the nonlinear method, the mean deviation decreases as a function

of increasing percentage, but ranges from only 5 to 15% for percentages below 20%. The nonlinear method seems to be more reliable for individual cases, and for unknown atmospheric conditions. However, for several cases and percentages burned below 60%, the linear method gives better results.

For the nonlinear method to be applied, it is necessary to distinguish the fluctuations of NDVI due to the atmosphere from the difference of NDVI due to burning. The mean standard deviation of these fluctuations, used to evaluate the background NDVI limit for the nonlinear method is 0.01, irrespective of the background type. The NDVI of the initial background should be at least 0.01 above that of the totally burned area to be reasonably distinguished. Since the top-of-atmosphere NDVI of a totally burned area is negative (Fig. 3), and discontinuities occur for very low values of the background NDVI (change in backgrounds with positive NDVI.

4. PROBLEMS AND LIMITATIONS

4.1. Case of heterogeneous pixels

So far only homogeneous pixels have been considered. The case of mixed pixels, containing vegetation and another type of background is now investigated. In a first set of simulations, the portion occupied by vegetation, considered as a potential fuel, varies and is totally burned in the simulations, the portion occupied by the other background type being left unburned. In a second set of simulations, the portion occupied by the potential fuel within the pixel is maintained constant and is partially burned, step by step. For the linear method, surface reflectances in channel 2 are directly used to eliminate the errors due to atmospheric contaminations and only compute the errors due to pixel heterogeneity. For the nonlinear method, the coefficients A_0, A_1 and A_2 are fitted using standard tropical atmospheric conditions (see section 2).

4.1.1. Totally burned vegetation

Assuming that a portion α of the pixel (α varying from 0 to 1) is occupied by the potential fuel (background A: savanna, or green vegetation), and that the remaining portion ($1-\alpha$) is occupied by another type of background

(background B: savanna, green vegetation, or sand), The background reflectance and NDVI of the mixed pixel can be expressed as:

$$Rbg_i = \alpha * Ra_i + (1-\alpha) * Rb_i \quad (7)$$

$$NDVIbg = (Rbg_2 - Rbg_1)/(Rbg_2 + Rbg_1) \quad (8)$$

where Ra_i and Rb_i are the reflectances of backgrounds A and B, respectively, in channel i (i=1,2). As the portion α composed by the potential fuel is assumed to burn totally within the pixel, the characteristics of background A are replaced by those of a totally burned area. The reflectances and NDVI of the pixel become:

$$Rbn_i = p_o * Rtb_i + (1-p_o) * Rb_i \quad (9)$$

$$NDVIbn = (Rbn2 - Rbn1)/(Rbn2 + Rbn1) \quad (10)$$

In Eq. (9) and (10), Rbn_i (i=1, 2), and NDVIbn are the channel i reflectance and the NDVI of the pixel after burning, respectively, Rtb_i is the reflectance of the burned portion of the pixel, and p_o is the portion burned, with $p_0=\alpha$. The background channel 2 reflectance (Rbg_2), and the background NDVI (NDVIbg) determined in Eq. 7 and 8, respectively, allow one to calibrate $R_2=f(p)$ and to calculate the coefficients of p=f(NDVI). The percentage burned, noted p_c, is recalculated using each method, by reporting Rbn_2 and NDVIbn (from Eq. 10

and 11), respectively, in the relationships $R_2=f(p)$ and $p=f(NDVI)$. The resulting error, Δp, is obtained by subtracting the percentage initially applied, p_o, from the percentage found, p_c. Thus, positive errors correspond to an overestimate of the percentage burned after applying the method, as negative errors correspond to an underestimate of the percentage burned.

Figures 13 and 14 show the results obtained for the method using channel 2 and for the method using NDVI, respectively. They indicate that no errors are associated with homogeneous pixels (pixels covered by the same type of background), which confirms that the error calculations are limited to the heterogeneity of the pixel.

For the linear method, the theoretical error is a function of p_o, and is given by the following formula:

$$\Delta p\ (p_o) = (Rtb_2-Ra_2)*p_o/(Rtb_2-p_o*Ra_2-(1-p_o)*Rb_2) - p_o \qquad (11)$$

where $p_o \in [0,1]$. For the nonlinear method, the dependence of the theoretical error with p_o is much more complex, but can be indirectly expressed as a function of the background NDVI, NDVIbg, and the NDVI after burning, NDVIbn, which are both a function of p_o (Eq. 12).

$$\Delta p\ (p_o) = A_o(NDVIbg) + A_1(NDVIbg)NDVIbn + A_2(NDVIbg)NDVIbn^2 \qquad (12)$$

In Eq.12, the coefficients A_i (i=0,2) can be determined from Fig. 10. For the linear method, extreme values of p_o (p_o=0, or p_o=1) give a null error (Δp=0), which confirms that when nothing is burned within the pixel, the reflectance or the NDVI of the background measured is unchanged (no atmospheric effects or errors due to successive observations have been considered). Thus, when everything is homogeneously burned within the pixel, the reflectance and the NDVI of a totally burned area are theoretically retrieved. For the nonlinear method, fitting the coefficients A_o, A_1, A_2 introduce slight errors, that do not permit to retrieve the exact NDVI of the background when nothing is burned (Fig. 16), or perfectly null error for an homogeneous pixel (Fig 14(b)), but they are negligible for the length of errors computed.

In Fig. 13(a) and 14(a), low reflective savanna associated with a higher reflectance background (sand or vegetation) is burned. When the same pixel, with the same percentage burned, is supposed homogeneous, its reflectance after burning is higher than that of the heterogeneous pixel ($Rbg_i > Rb_i$ in Eq. 9). The lower values of reflectances obtained in the heterogeneous case give lower values of the percentage burned, i.e. negative errors. Inversely, when highly reflective green vegetation is associated with a lower reflective

background the reflectance of an homogeneous pixel after burning is lower than that of an heterogeneous pixel ($Rbg_i < Rb_i$ in Eq. 9), and the percentage burned calculated is overestimated.

The higher the spectral difference between the two backgrounds within the heterogeneous pixel, the higher the errors on the percentage of area burned calculated. Relative errors are high ($\Delta p/p_o$ >100%) with both methods when green vegetation is burned within a pixel containing more than 50% of savanna. However, this might not be a problem, since savanna is more likely to burn than green vegetation. The method using channel 2 gives better results than of the method using NDVI for heterogeneous pixels, especially when the background with the lowest reflectance (e.g., savanna) is burned within pixels containing a higher reflectance background (e.g., green vegetation). The method using NDVI is not valid when the gap of NDVI between the two backgrounds is above 10%, and when the background with the lowest NDVI is burned. On the other hand, relative errors remain below 50% when more than 60% of the background with the higher reflectance (i.e., green vegetation) is burned.

4.1.2. *Partially burned vegetation*

The effect of burning partially one of the two backgrounds is studied following the same steps as above, assuming that the potential fuel occupies a constant percentage of the pixel, and that a percentage, $p_o \in [0, x]$, of the entire pixel burns.

For the linear method, the channel 2 reflectance and the absolute error on area burned, Δp, after burning the percentage p_o, can be expressed as:

$$Rbn_2 = x*Rb_2 + p_o* Ra_2 + (1-(x+p_o)*Ra_2 \quad (13)$$

$$\Delta p = \{(Rtb_2-Ra_2)*p_o/(Rtb_2-(1-x)*Ra_2-x*Rb_2)\} - p_o \quad (14)$$

Equation 14 shows that for a constant x Δp is a linear function of p_o. The variations of Δp with p_o obtained for x=50% are reported in Fig. 15 (linear method) and 16 (nonlinear method).

The relative errors ($\Delta p/p_o$) are constant for each background combination when using channel 2, and are basically the same when the potential fuel (background A) is totally burned within the heterogeneous pixel (Fig.15). These errors are up to 55% when the difference between the channel 2 reflectances of the two initial backgrounds is greater than 30% (mixture of savanna and green vegetation), whatever the background burned. Applying the linear

method to heterogeneous pixels, in which one of the backgrounds is partially burned, does not introduce additional errors on the percentage determined.

The relative errors obtained with NDVI are greater than 60% when the difference between the NDVI of the two initial backgrounds is above 40%, and the background with the highest NDVI (green vegetation) is burned. Applying the NDVI-based method to forests ecosystems, however, should not give large errors, since forests are generally homogeneous. Lower relative errors (30 to 40%) are found when the difference between the NDVI of the two backgrounds is less than 10% (mixture of savanna and sand). The nonlinear method should be used only for heterogeneous pixels that have not-too-different NDVI characteristics initial backgrounds.

The results of Figs 15 and 16 suggest that backgrounds of low channel 2 reflectance and NDVI within the pixel may increase the error on the estimated percentage of area burned. Targets such as water, clouds, or shadows may contribute to lower the reflectance and NDVI of the entire pixel. Thus the suitability of both methods depends upon the initial background characteristics, which should be at least above those of a totally burned area. In practice, the

lowest limit for channel 2 reflectance and NDVI determined earlier (see section 3.) should take the contribution of such targets into account.

4.2. Effect of satellite resolution

Due to atmospheric and geometric effects, which cannot be connected entirely in the methods, there is a limit in percentage of pixel burnt below which the effect of area burnt cannot be detected. To examine this limit, The differences between the channel 2 reflectance or NDVI of the initial background (savanna or green vegetation) and of the area burned are calculated as a function of the percentage of the pixel burnt. Surface reflectances are used in the method using channel 2, and top-of-atmosphere NDVI obtained for standard atmospheric and viewing conditions are used in the method using NDVI. The results are displayed in Figs. 17 and 18, respectively. In order to distinguish the burned area from its background, their spectral or NDVI differences must be at least higher than the thresholds determined in section 3., characterized by the mean standard deviation of the fluctuations, mainly due to the change in atmospheric and viewing conditions between two observations, of the initial background signal. These thresholds, reported in the figures for each background type, indicate that the reflectance or NDVI

signature of a pixel having less than 20% (savanna) and 10% (green vegetation) of its area burnt cannot be detected.

Now, depending on the spatial resolution of the satellite instrument, the detectable percentage of area burnt may translate into different detectable areas burnt (in units of length squared). For the methods to provide good estimates of area burnt, the detectable area burnt should be smaller than the average size of the fire scars. This average size may vary depending on the ecosystem.

In the case of African savannas, Vickos (1991) reported that the average length of a fire front is about 1140 m, and occupies 2 AVHRR pixels in average. Similar results were obtained by Langaas (1992), who indicated, after scanning 26 NOAA evening and early morning images, that more than 70% of the fire agglomerations consisted of one or two fire pixels. The number of fire-affected pixels however does not give an indication on the area actually burned. Depending on its temperature, an active fire has to occupy only 10^{-4} to 10^{-3} of the AVHRR pixel to be detectable (Kaufman et al., 1991). On the other hand, when drygrass areas are affected by fire, they often contain unburned areas (Hopkins, 1965; Frederiksen et al., 1991). Hopkins (1965) suggested that the

percentage of area burnt may be used as an indicator of the severity of the fire. Experimental fires in the early dry season (December) gave low values of 25% for the percentage of cover burnt. Later burnings (between January and March) gave values between 64 and 96% of with a mean of 84%, as the vegetation gets dryer at the end of the dry season. Frederiksen et al. (1991), using photographs taken during field experiments in northern and central Senegal, gave the relative frequency of fractional cover burnt in class intervals of 10%. Théir results indicate an average of about 80% of burned drygrass. Assuming that a AVHRR pixel of 1.1 km resolution is actually burned with an average of 80% for drygrass, the average size of an individual surface burned would be about 0.9 km^2. Since fire size and shape depend on factors such as wind direction and strength during the burning, the landscape or the vegetation type, such an estimate is rather crude, yet sufficiently accurate for studying spatial resolution effects.

Using LAC data at 1 km resolution, the average fire scar of 0.88 km^2 determined above for African savanna ecosystems corresponds to 80% of the pixel burned. Both channel 2 reflectance and NDVI differences are above the limits permitted (Figs. 17 and 18). LAC data at 1 km resolution seem to be well

adapted and sufficiently sensitive to the average area burned of this range. Using GAC data at 4 km resolution, however, the average area burnt corresponds to only 5.5% of the pixel size. The corresponding channel 2 reflectance and NDVI differences are both significantly below the detectable limit (Figs. 17 and 18). Therefore, GAC data are not recommended to study burned scars in African savanna ecosystems, unless the study is focused on large fires occupying at least 20% (i.e., 3.2 km^2) of the pixel. The lowest resolution of the satellite that can be used to detect scars left by savanna fires is about 2 km. Lower resolution may be used for green vegetation (if the fire scars have the same size), but the difference is not so large to be further discussed. In any case, the greener the vegetation, the higher the contrast between the background and the area burned signals.

5. SUMMARY AND CONCLUSION

Considering a wide range of realistic atmospheric and viewing conditions, the top-of-atmosphere simulations showed that either near-infrared radiances or derived NDVIs can be used to estimate area burned, taking into account the contribution of partially burned pixels. The higher the contrast between the totally burned and unburned targets, the more accurate the estimates. In wavebands corresponding to AVHRR channel 2, the top-of-atmosphere spectral difference between the two types of backgrounds ranges from 40.7 to 77.4% of the background surface reflectance (it ranges from 68.8 to 88.6% at the surface). As for NDVI, the top-of-atmosphere difference ranges from 83.3 to 106.2% (from 79.8 to 93.4% at the surface).

The two methods proposed to deduce the area actually burned are based on relationships between the near-infrared reflectance (channel 2 of AVHRR) or NDVI, and the percentage burned. For both methods, knowledge of the background reflectance and NDVI, respectively, prior to the fire event is necessary to calibrate the relationships: $R_2=f(P)$ and $P=f(NDVI)$. Since the near-infrared surface reflectance of a totally burned area is well-known, it can be used to calibrate the linear relationship $R_2=f(P)$. The difficulty in determining

its reflectance at the top of the atmosphere resides on the facts that totally burned areas are not easy to classify, some areas often remain unburned, and atmospheric and viewing conditions modify the reflectance. It is then preferable to use the surface reflectance as a reference for the area totally burned, and to correct the top-of-atmosphere data from atmospheric effects to have comparable and compatible values. Standard atmospheric corrections, necessary to calibrate $R_2=f(P)$, are subject to an average error on area burned of about 10%, with errors up to 46% for extreme conditions when compared to the standard condition specify the standard condition.

When applied to homogeneous backgrounds, the nonlinear method is found to be more accurate than the linear method. The mean relative errors associated are about 20% and 10% of the area burned, respectively. For heterogeneous targets, with a high spectral difference between the different background components, the linear method gives better results, especially when the background with the lowest reflectance is burned (e.g., when dry grass is burned, and greener trees remain unburned).

The method using NDVI is not valid for heterogeneous pixels, unless the NDVI difference between the different backgrounds is below 0.1, and the

background with the lowest NDVI is burned. Both methods are not applicable when the target contains very low reflectance backgrounds (e.g., water). The presence of such backgrounds considerably lower the reflectance or NDVI of the initial background, making it difficult to distinguish the background from a totally burned area. The reflectance or NDVI, of the background may even be lower than of the totally burned area, resulting in a sign change of the slope for the linear method, and a discontinuity for the nonlinear method. As a result, lowest limits for the initial background reflectance and NDVI have been determined as for applying the methods. The initial background reflectance has to be at least equal to 0.09 in order to apply the linear method. As for the nonlinear method, the NDVI of the initial background has to be positive.

Considering an average fire size of 0.88 km^2 in African savannas, the lowest satellite resolution that can be used is 2 km. Lower resolution (3 km) can be used for greener vegetation (e.g., forest). GAC data at 4 km resolution can be used to study large fires, but are not appropriate to compute area burned for the average fire size of 0.88 km^2. In addition, the lower the resolution, the more heterogeneous the pixel may get. One should therefore be careful before generalizing the methods to larger scales. A knowledge of the

characteristics of the ecosystem studied is preferable in order to be able to interpret the results obtained using the two methods. The accuracy of the methods rely on the pixel composition and homogeneity, the greenness of the vegetation, and the satellite resolution. The greenness of the vegetation and the burning efficiency may have compensatory effects: green vegetation may not entirely burn (low percentage burned), but the area burned can be determined with a good accuracy. On the contrary, dry vegetation gives lower accuracy, but the percentage burned is expected to be higher. The higher the percentage burned, the lowest the error, especially for heterogeneous pixels.

Symbol	Parameter
R_i	NOAA-AVHRR channel i reflectance (i=1,2)
P	Percentage of area burned
V	visibility (km)
UH2O	Water vapor content of the atmosphere ($g.cm^{-2}$)
θ_v	Satellite view angle (º)
θ_s	Sun view angle (º)
R^*	Apparent reflectance
R_a	Rayleigh aerosol reflectance
R_s	Surface reflectance
S_a	Spherical albedo of the atmosphere
T_a	Scattering transmittance
T_g	Gaseous transmittance
R_c	Channel 2 reflectance after atmospheric corrections
S_c	Slope calculated using the corrected reflectance R_c
S_s	Slope calculated using the surface reflectance R_s
Δp_u	Maximum absolute error on the percentage of area burned (slope underestimated)
Δp_o	Maximum absolute error on the percentage of area burned (slope overestimated)
P_{true}	Percentage of area burned initially applied
P_{cal}	Percentage of area burned calculated using either method
Rbn_i	Reflectance of a burned area in channel i(i=1,2)
Rbg_i	Reflectance of an homogeneous background in channel i(i=1,2)
α	Portion of green vegetation in a given pixel
Rsv_i	Savanna reflectance in channel i(i=1,2)
Rvg_i	Reflectance of green vegetation in channel i(i=1,2)
NDVIbn	NDVI after burning the area

Ra_i	Reflectances of background A in channel $i(i=1,2)$
Rb_i	Reflectances of background B in channel $i(i=1,2)$
Rbg_i	Reflectances of the heterogeneous background B in channel $i(i=1,2)$
NDVIbg	NDVI of the heterogeneous background
Rtb_i	Reflectance of a totally burned area
po	Percentage of the heterogeneous pixel burned
x	Fixed percentage of the heterogeneous pixel containing vegetation

References:

Brustet, J.M., Vickos,J.B., Fontan, J., Manissadjan, K., Podaire, A., and Lavenu, F. (1991) Remote sensing of Biomass burning in West Africa with NOAA-AVHRR. In: *Global Biomass burning*, The MIT Press Cambridge, Massachusssetts, edited by Joel S. Levine, pp. 47-52.

Cahoon, D.R.Jr., Stocks, B.J., Levine, J.S., Cofer, W.R. III and O'Neill, K.P. (1992) Seasonal distribution of African savanna fires, *Nature*, 359:812-815.

Chuvieco E. and Congleton R.G. (1988) Mapping and inventory of forest fires from digital processing of TM data. *Geocarto Int.*, 4(4),41-53.

Delmas, R.A. (1990) Research activities in Africa related to the IGAC programme, IGAC *Newsletter*, 2.

Franca, J.R.A., Brustet, J.M., and Fontan, J. (1993) A multispectral remote sensing of biomass burning in West Africa, *Journal of atmospheric Chemistry (In press).*

Frederiksen, P.S., Langaas S. and Mbaye, M. (1990) NOAA AVHRR and GIS-based monitoring of fire activity in Senegal - a provisional methodology and potential applications. In: *Fires in the tropical biota*, Ecological studies 84, edited by Goldammer, J.G, pp. 400-417.

Goldammer, J.G. (1990) Fire in the tropical biota, In: *Fire in the Tropical Biota*, Ecological studies 84, edited by Goldammer, J.G.

Hao, W.M., Liu, M., and Crutzen, P.J. (1990) Estimates of annual and regional releases of CO_2 and other trace gases to the atmosphere from fires in the

tropics, based on the FAO statistics for the period 1975-1980, In: *Fire in the Tropical Biota*, Ecological studies 84, edited by Goldammer, J.G, pp. 440-462.

Hopkins-B (1965) Observations on savanna burning in the Olokemeji Forest Reserve. *J. Appl. Ecol* 2:367-381.

Iacobellis, S.F., Frouin, R., Razafimpanilo, H., and Sommerville, R.C.J. (1993) Biomass burning in the savannas of North Africa and atmospheric carbon dioxide. *Jour. Geoph. Res.* (in-press).

IGBP-DIS Workshop on Algorithms for Remotely Sensed Fire Detection, held at NASA-Goddard Space Flight Center, February 1993, Greenbelt, Maryland.

Justice, C.O., Malingreau J.P. and Seltzer, A.W. (1993) Remote sensing of fires: potential and limitations. In: *Fire in the Environment:* the ecological , atmospheric and climatic importance of vegetation fires. Dahlem Workshop, Berlin, March 15-20 1992. pp.77-88.

Kasischke, E.S., Harrell, P., Ustin, S.L. and Barry, D. (1992) Monitoring of wildfires in boreal forests using AVHRR Large Area Coverage imagery. *Remote sensing of the environment* (submitted).

Kaufman, Y.J., Setzer, A., Justice, C.O., Tucker, C.J., Pereira, M.C. and Fung I. (1990) Remote sensing of biomass burning in the tropics. In: In: *Fires in the tropical biota*, Ecological studies 84, edited by Goldammer, J.G, pp. 371-399.

Kendall, J. (1993) 1km Operational active fire detection, presented at the IGBP-DIS Workshop on Algorithms for Remotely Sensed Fire Detection, held at NASA-Goddard Space Flight Center, February 1993, Greenbelt, Maryland.

Kennedy, P.J. (1992) Biomass burning studies: the use of remote sensing, *Ecological Bulletins*, 42:133-148.

Kennedy, P.J., Belward, A., and Gregoire J.M. (1993) An improved approach to fire monitoring in West Africa using AVHRR data, submitted to *Int. J. Remote Sensing*.

Langaas, S. (1989) A study of spectral characteristics of burnt areas in Senegal, with recommendations for an AVHRR based bushfire monitoring methodology, Dept. of Surveying, Agric. Univ. of Norway, Aas.

Langaas, S. (1992) Temporal and spatial distribution of savanna fires in Senegal and the Gambia, West Africa, 1989-90, derived from multi-temporal AVHRR night images, *Int. J. Wildland Fire* 2(1): 21-36.

Langaas, S. (1993a) A parametrised bispectral model for savanna fire detection using AVHRR night images, *Int. J. of Remote sensing*, 14(12): 2245-2262.

Langaas, S. (1993b) Diurnal cycles in savanna fires. *Nature* Vol. 363, 13 May. page 120 (Scientific Correspondence).

Lavenu, F (1984) Teledetection et vegetation tropicale: Exemple du nord-est de la Cote d'Ivoire. Ph.D. Theses No2966, Univ. Paul Sabatier, Toulouse, France, 190 pp.

Lee, T.F. and Tag, P.M. (1990) Improved detection of hotspots using the AVHRR 3.7 μm channel. *Bulletin of the American Meteorological Society*, 71(12):1722-1730.

Levine, J.S. (1991) Global biomass burning: atmospheric, climatic, and biospheric implications. In: *Global Biomass Burning*, Cambridge, MA: The MIT press, edited by Levine, J.S.

Malingreau, J.P. (1990) The contribution of remote sensing to the global monitoring of fires in tropical and sub-tropical ecosystems. In: In: *Fires in the tropical biota*, Ecological studies 84, edited by Goldammer, J.G, pp. 337-368.

Matson, M. and Dozier, J. (1981) Identification of subresolution high temperature sources using a thermal IR sensor, *Photo. Engr. and Remote Sensing*, 47(9): 1311-1318.

Matson, M. and Holben, B. (1987) Satellite detection of tropical burning in Brazil, *Int. J. Remote Sensing*, 8(3): 509-516.S

Menaut, J.C., Abbadie, L., Lavenu, F., Lodjani, P., and Podaire, A. (1991) Biomass burning in West African savannas, In: *Global Biomass Burning*, Cambridge, MA: The MIT press, edited by Levine, J.S, pp. 133-144.

Pereira, M.C., Alfredo, C., Setzer, A.W. and Joao R. dos Santos (1991) Fire estimates in savannas of central Brazil with thermal AVHRR/NOAA calibrated by TM/Landsat. Proceedings 24th International Symposium on Remote Sensing of the Environment, Rio de Janeiro, Brazil, May, 27-31, 1991.

Pereira, M.C and A.W. Setzer (1993) Spectral caracteristics of fire scars in Landsat 5 TM images of Amazonia. *Int. J. Remote Sensing*, (In-press)

Robinson, J.M. (1991) Problems in global fire evaluation: Is remote sensing the solution?, In: *Global Biomass Burning*, Cambridge, MA: The MIT press, edited by Levine, J.S.

Robinson, J.M. (1992) Fire from space: Global fire evaluation using infrared remote sensing, *Int. J. Remote Sensing*, 12(1):3-24.

Tanaka, S., Kimura, H. and Suga, Y. (1983) Preparation of a 1:25 000 Landsat map for assessment of burnt area on Etajima Island, *Int. J. Remote Sensing*, 4:17-31.

Tanre, D., Deroo, C., Duhaut, P., Herman, M., Morcrette, J.J., Perbos, J. and Deshamps (1990) Technical Note - Description of a computer code to simulate the satellite signal in the solar spectrum: The 5S code, *Int. J. Remote Sensing*, 11: 659-668.

Vickos, J.B. (1986) Etude des feux de savannes. Diplome d'Etudes Approfondies, Université Paul Sabatier, Toulouse, France.

Vickos, J.B., Deshamps P.Y., Podaire A., and Lavenu F. (1988) Remote sensing of bush fires . ISLSCP Symposium Niamey Niger, April 25 - 29, 1988.

Vickos, J.B. (1991) Télédétection des feux de végétation en Afrique intertropicale et estimation des émissions de constituants ayant un intérêt atmosphérique. Ph.D. Thesis, Université Paul Sabatier, Toulouse, France, 148 pp.

Figure captions:

Figure 1 (a-c): Simulations of the AVHRR channel 1 top-of-atnmosphere reflectance for homogeneous targets (totally burned area, savanna, and green vegetation). The mean conditions for invariant parameters are the following: continental aerosols, 15 km visibility, water vapor content of 4.1 g.cm^{-2}, and a view angle of 30º. The solar zenith angle θ_S and the azimuthal angle difference ($\varphi=\varphi_V-\varphi_S$) are considered constant and equal respectively to 30º and 90º. Channel 1 reflectance is plotted as a function of (a) visibility (5 to 25 km) (b) water vapor content (0 to 6 g.cm^{-2}), and (c) view angle θ_V (0 to 50º).

Figure 2 (a-c): Simulations of the AVHRR channel 2 top-of-atnmosphere reflectance. Atmospheric conditions are the same as for Fig. 1. Channel 2 reflectance is plotted as a function of (a) visibility (5 to 25 km) (b) water vapor content (0 to 6 g.cm^{-2}), and (c) view angle θ_V (0 to 50º).

Figure 3 (a-c): Simulations of the AVHRR-derived NDVI at the top of the atmosphere. Atmospheric conditions are the same as for Fig. 1. The derived NDVI is plotted as a function of (a) visibility (5 to 25 km) (b) water vapor content (0 to 6 g.cm^{-2}), and (c) view angle θ_V (0 to 50º).

Figure 4: Variation of the linear function $R_2=f(P)$ with atmospheric conditions and viewing geometry for savanna and green vegetation. (1) $\theta_S=0º$, $\theta_V=0º$, UH2O=1 g.cm^{-2}, maritime aerosols, V=5 km (2) $\theta_S=60º$, $\theta_V=50º$, UH2O=1 g.cm^{-2}, maritime aerosols, V=5 km (3) $\theta_S=30º$, $\theta_V=30º$, UH2O=4 g.cm^{-2}, continental aerosols, V=15 km.

Figure 5 (a-c): Variations of the slope of the relationship $R_2=f(P)$ with atmospheric conditions. Atmospheric conditions are the same as for Fig. 1. The slope is plotted as a function of (a) visibility (5 to 25 km) (b) water vapor content (0 to 6 g.cm^{-2}), and (c) view angle θ_V (0 to 50º).

Figure 6: General calculation of maximum errors due to changes in atmospheric conditions between successive observations for a given slope (or a given channel 2 reflectance corrected for atmospheric effects). When the slope is underestimated, compared to the surface reference, the maximum absolute

error on the percentage of area burned is given by Δp_u. When the slope is overestimated, the absolute error is given by Δp_o.

Figure 7: Maximum absolute error on the percentage of area burned as a function of the error on the slope estimate due to calibration of $R_2=f(P)$ (see Fig.6 for the calculation of the maximum error). The maximum errors on the slope estimate for savanna and green vegetation are taken from Table 3 (a) and (b), respectively.

Figure 8: Percentage calculated, P_{cal}, as a function of the exact initial percentage applied using the linear method. Different atmospheric and geometrical conditions are considered, as well as different homogeneous backgrounds composed of savanna and green vegetation.

Figure 9: Variation of the nonlinear function p=f(NDVI) with atmospheric conditions and viewing geometry for savanna and green vegetation. Atmospheric conditions (labels) are the same as for the linear method (see Fig.4).

Figure 10 (a-c): Variation of the coefficients A0, A1, and A2 with the background NDVI. A0, A1 and A2 are the coefficients of the non-linear equation p=f(NDVI) described in Figure 9.

Figure 11: percentage calculated, using the nonlinear method, versus exact initial percentage applied. The combinations of the background, atmospheric and geometrical conditions are the same as for Figure 8.

Figure 12: Mean deviation, relative to the initial percentage burned, between the percentage calculated and the exact percentage applied for Figs. 8 and 11.

Figure 13 (a-b): Absolute error on area burned after applying the linear method to heterogeneous pixels. The error is calculated as a function of the percentage of (a) savanna or (b) green vegetation, which is totally burned within the heterogeneous pixel. Positive errors correspond to an overestimate of the initial percentage applied, as negative errors correspond to its underestimate.

Figure 14 (a-b): Absolute error on area burned after applying the nonlinear method to heterogeneous pixels. The error is calculated as a function of the percentage of (a) savanna or (b) green vegetation, totally burned, within the heterogeneous pixel. This Figure is comparable to Fig. 13.

Figure 15 (a-b): Absolute error on area burned after applying the linear method to heterogeneous pixels composed by 50% of vegetation. The error is calculated as a function of the percentage of (a) savanna or (b) green vegetation, partially burned, within the heterogeneous pixel.

Figure 16(a-b): Absolute error on area burned after applying the nonlinear method to heterogeneous pixels composed by 50% of vegetation. The error is calculated as a function of the percentage of (a) savanna or (b) green vegetation, partially burned, within the heterogeneous pixel. This Figure is comparable to Fig.15.

Figure 17: Reflectance channel 2 difference between the initial background (savanna or green vegetation) and the area burned as a function of the surface resolution burned. The lowest limit is characterized by the mean standard deviation of the fluctuations due to the change in atmospheric and viewing conditions between two observations.

Figure 18: NDVI difference between the initial background (savanna or green vegetation) and the area burned as a function of the surface resolution burned. As for Fig. 16, the lowest limit is characterized by the mean standard deviation of the fluctuations due to the change in atmospheric and viewing conditions between two observations. This Figure is comparable to Fig.17.

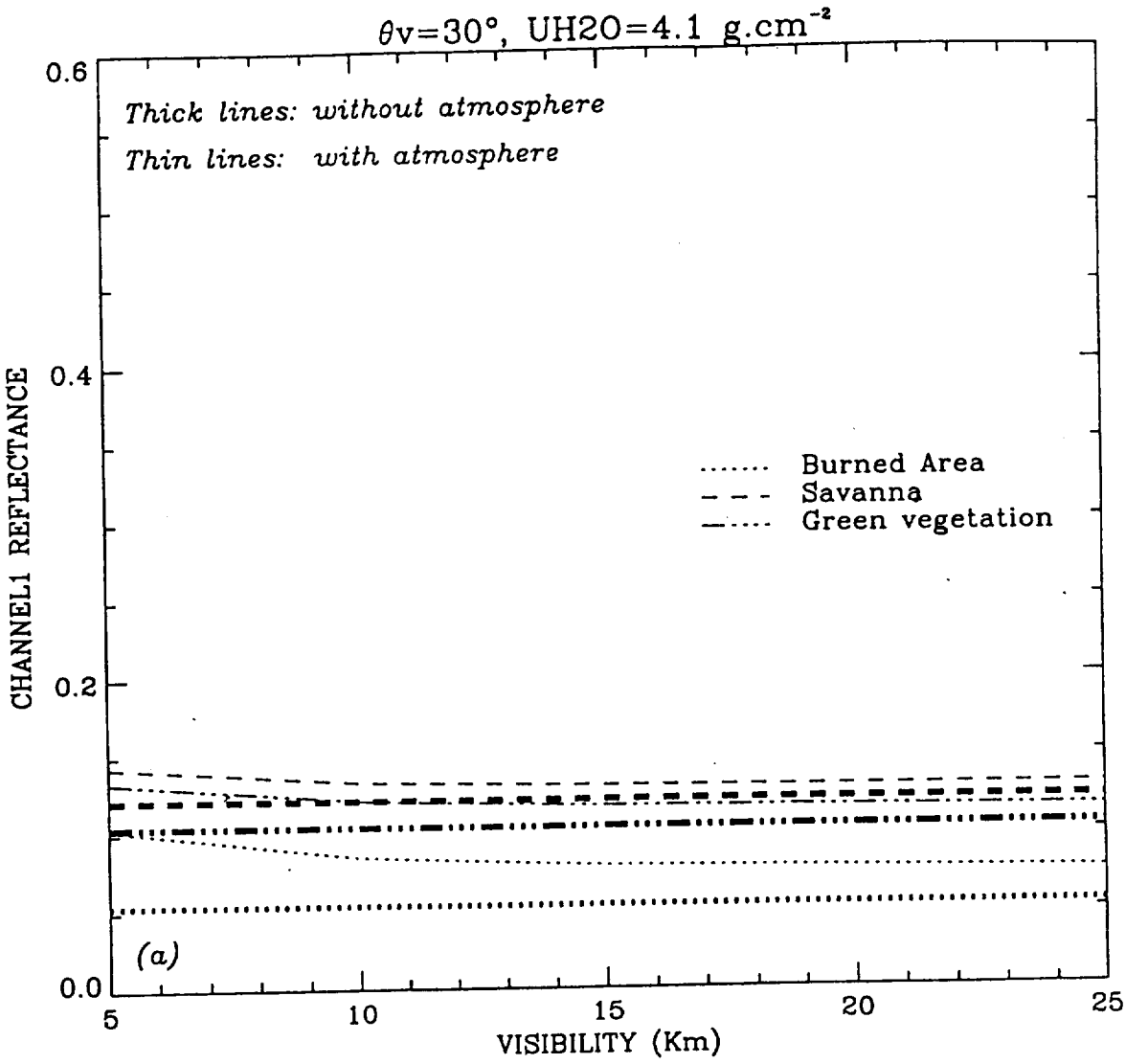
θv=30°, UH2O=4.1 g.cm⁻²
Thick lines: without atmosphere
Thin lines: with atmosphere
Burned Area
Savanna
Green vegetation
(a)
CHANNEL1 REFLECTANCE
VISIBILITY (Km)
0.0
0.2
0.4
0.6
5
10
15
20
25

Fig. 1 (a)

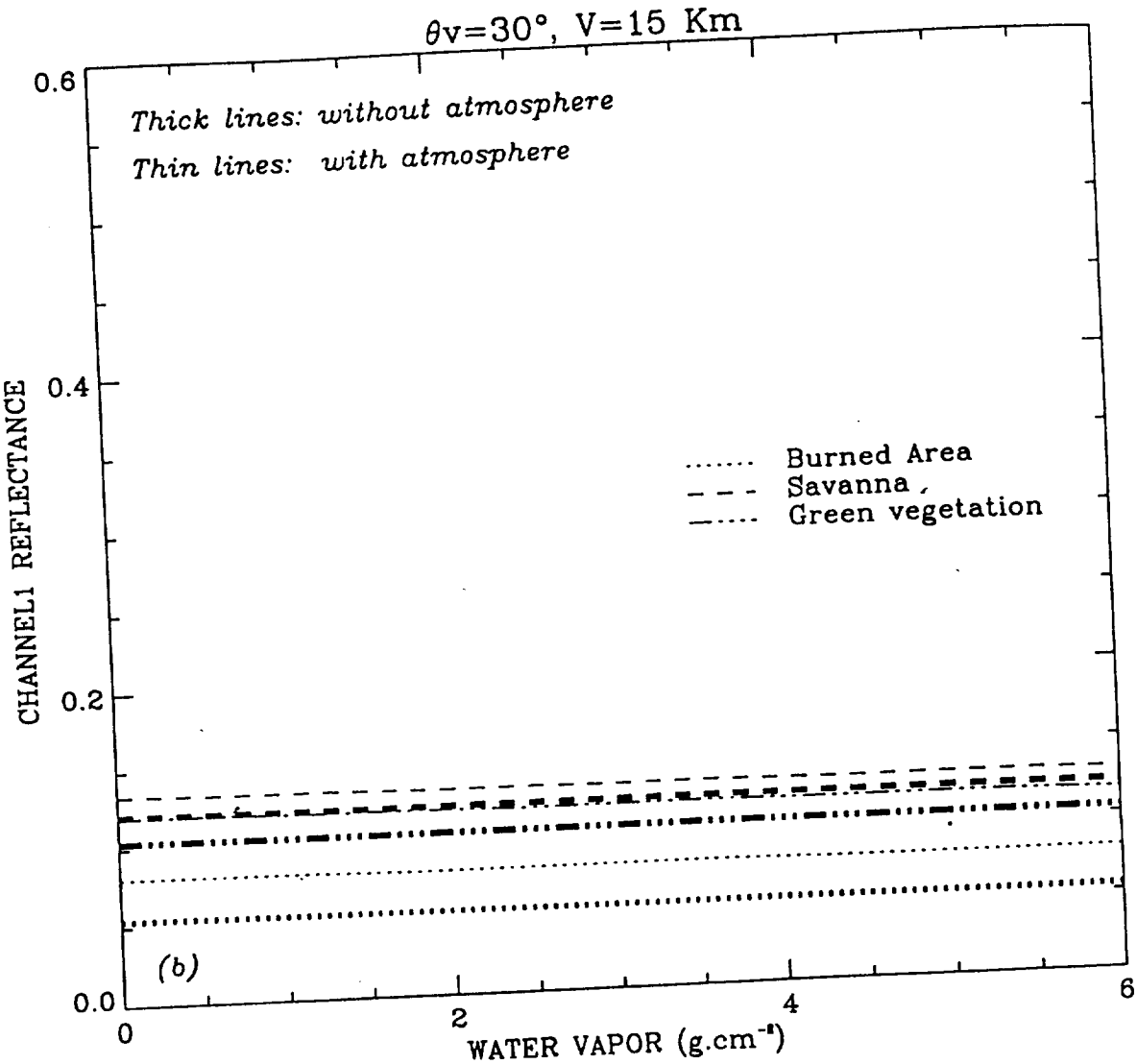
θv=30°, V=15 Km
Thick lines: without atmosphere
Thin lines: with atmosphere
Burned Area
Savanna
Green vegetation
(b)
CHANNEL1 REFLECTANCE
WATER VAPOR (g.cm⁻²)
0.0
0.2
0.4
0.6
0
2
4
6

Fig. 1 (b)

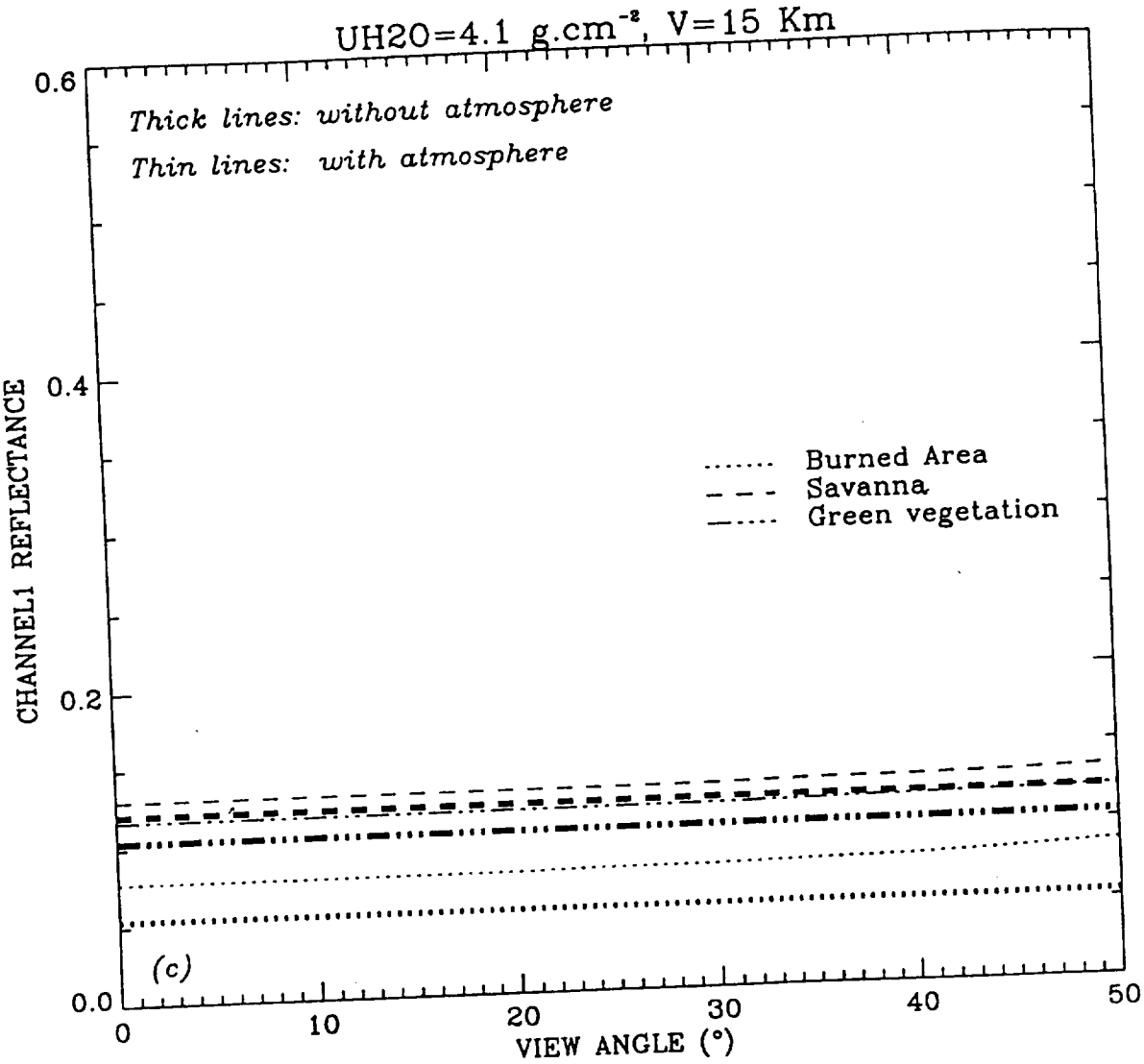
UH20=4.1 g.cm^{-2}, V=15 Km
Thick lines: without atmosphere
Thin lines: with atmosphere
Burned Area
Savanna
Green vegetation
(c)
CHANNEL1 REFLECTANCE
VIEW ANGLE (°)
0.0
0.2
0.4
0.6
0
10
20
30
40
50

Fig. 1 (c)

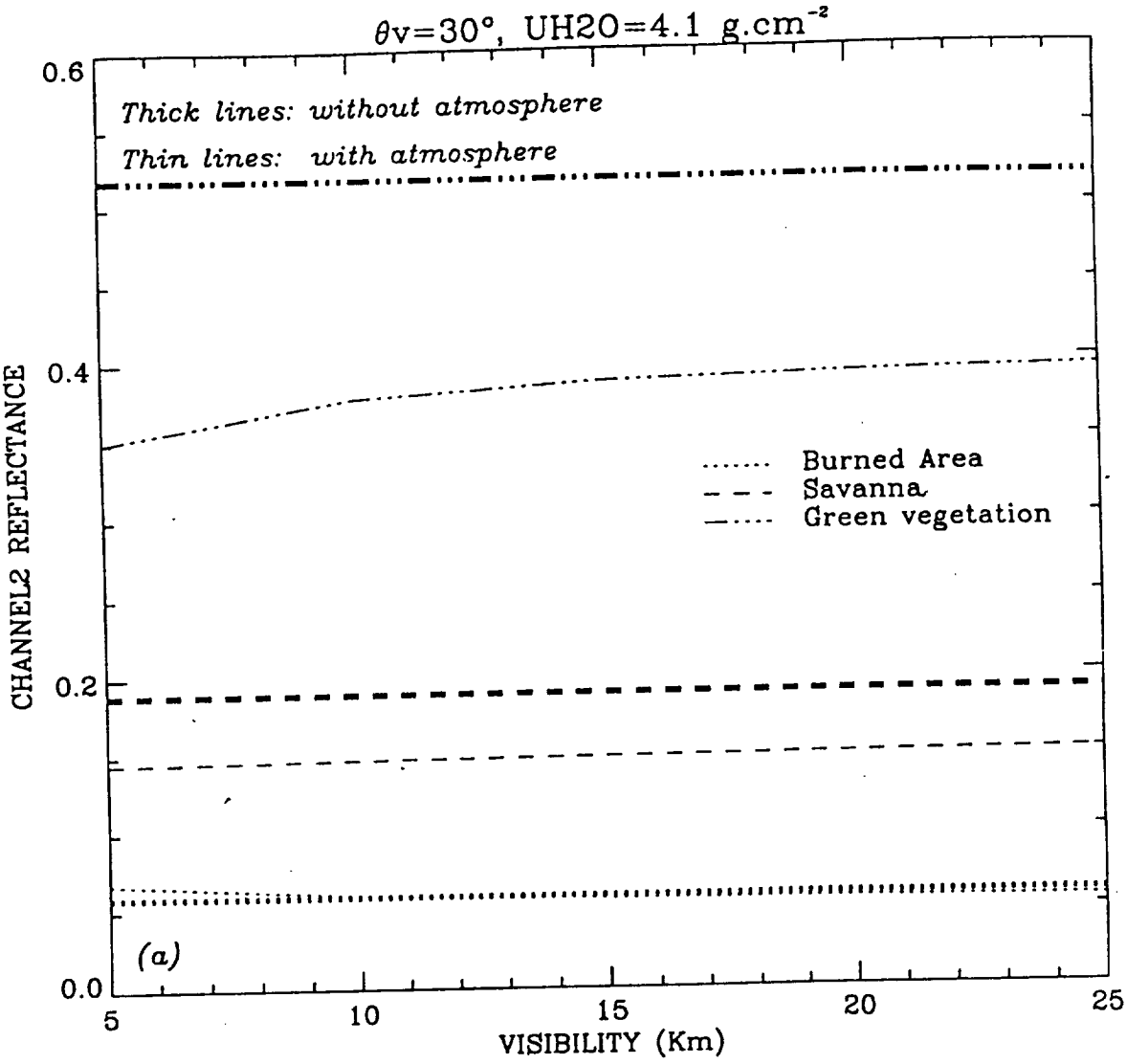
θv=30°, UH2O=4.1 g.cm⁻²
Thick lines: without atmosphere
Thin lines: with atmosphere
Burned Area
Savanna
Green vegetation
(a)
CHANNEL2 REFLECTANCE
VISIBILITY (Km)
0.0
0.2
0.4
0.6
5
10
15
20
25

Fig. 2 (a)

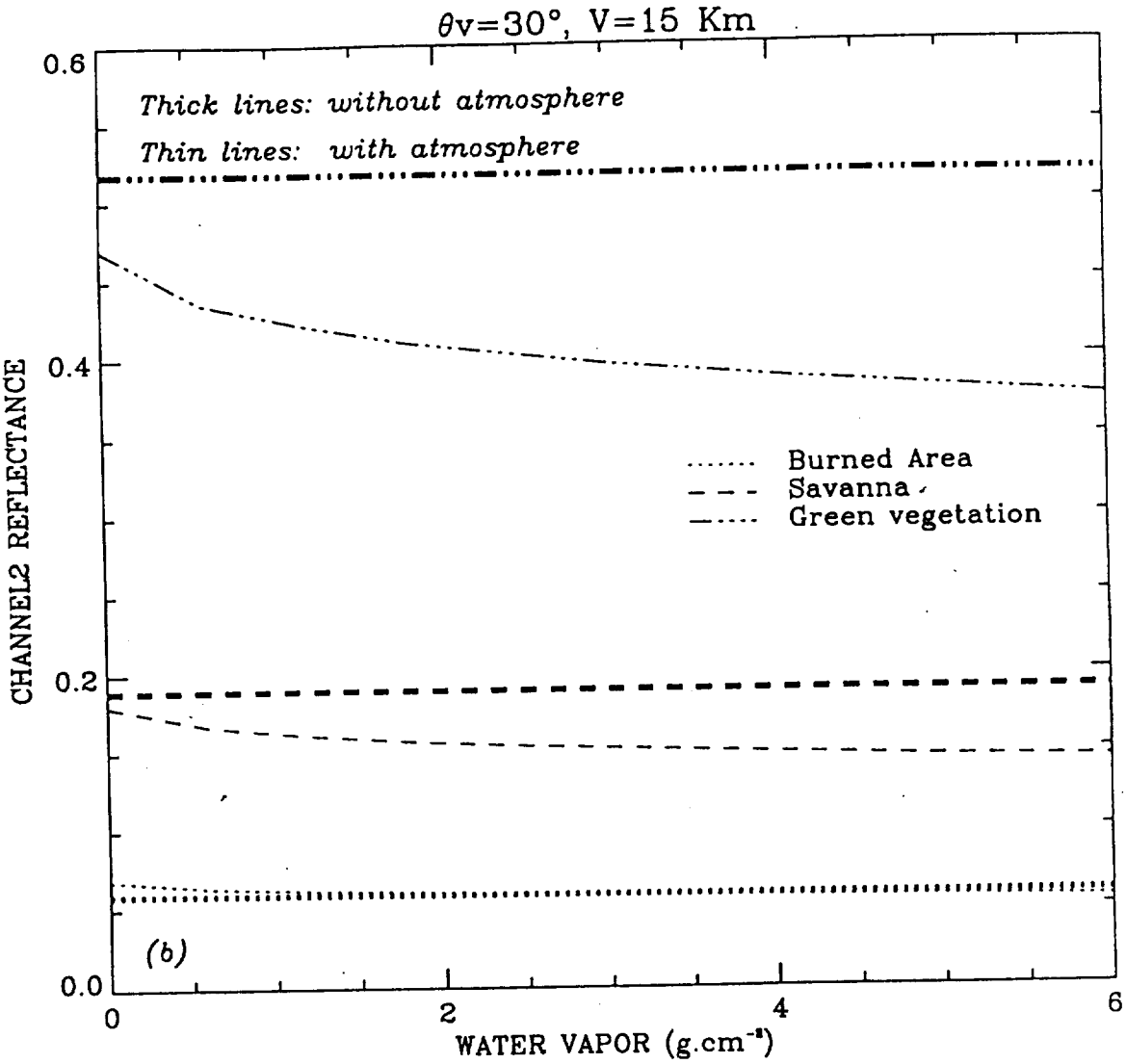
θv=30°, V=15 Km
Thick lines: without atmosphere
Thin lines: with atmosphere
Burned Area
Savanna
Green vegetation
(b)
CHANNEL2 REFLECTANCE
WATER VAPOR (g.cm⁻²)
0.0
0.2
0.4
0.6
0
2
4
6

Fig. 2(b)

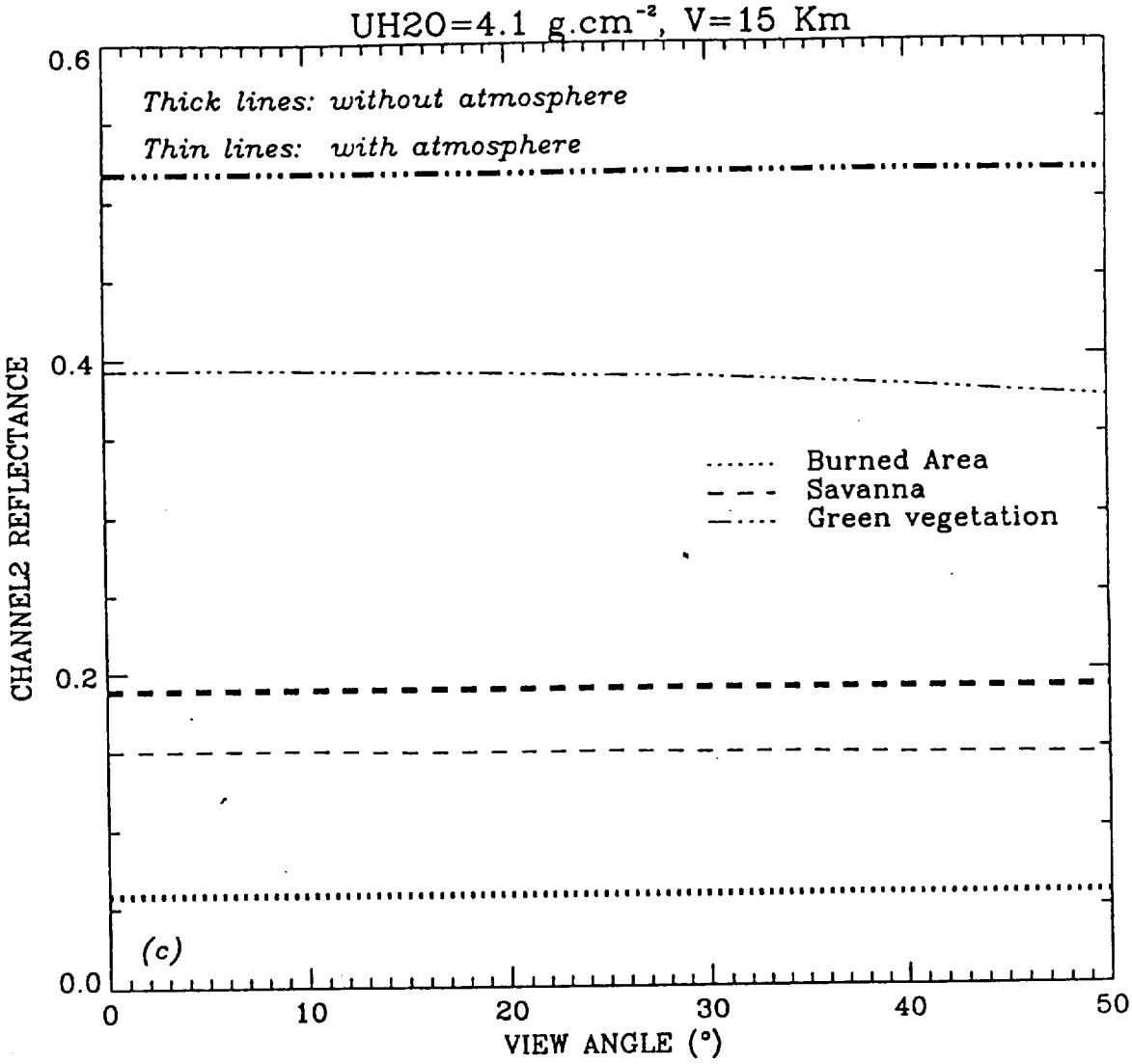
UH20=4.1 g.cm^{-2}, V=15 Km
Thick lines: without atmosphere
Thin lines: with atmosphere
Burned Area
Savanna
Green vegetation
(c)
CHANNEL2 REFLECTANCE
VIEW ANGLE (°)
0.0
0.2
0.4
0.6
0
10
20
30
40
50

Fig. 2 (c)

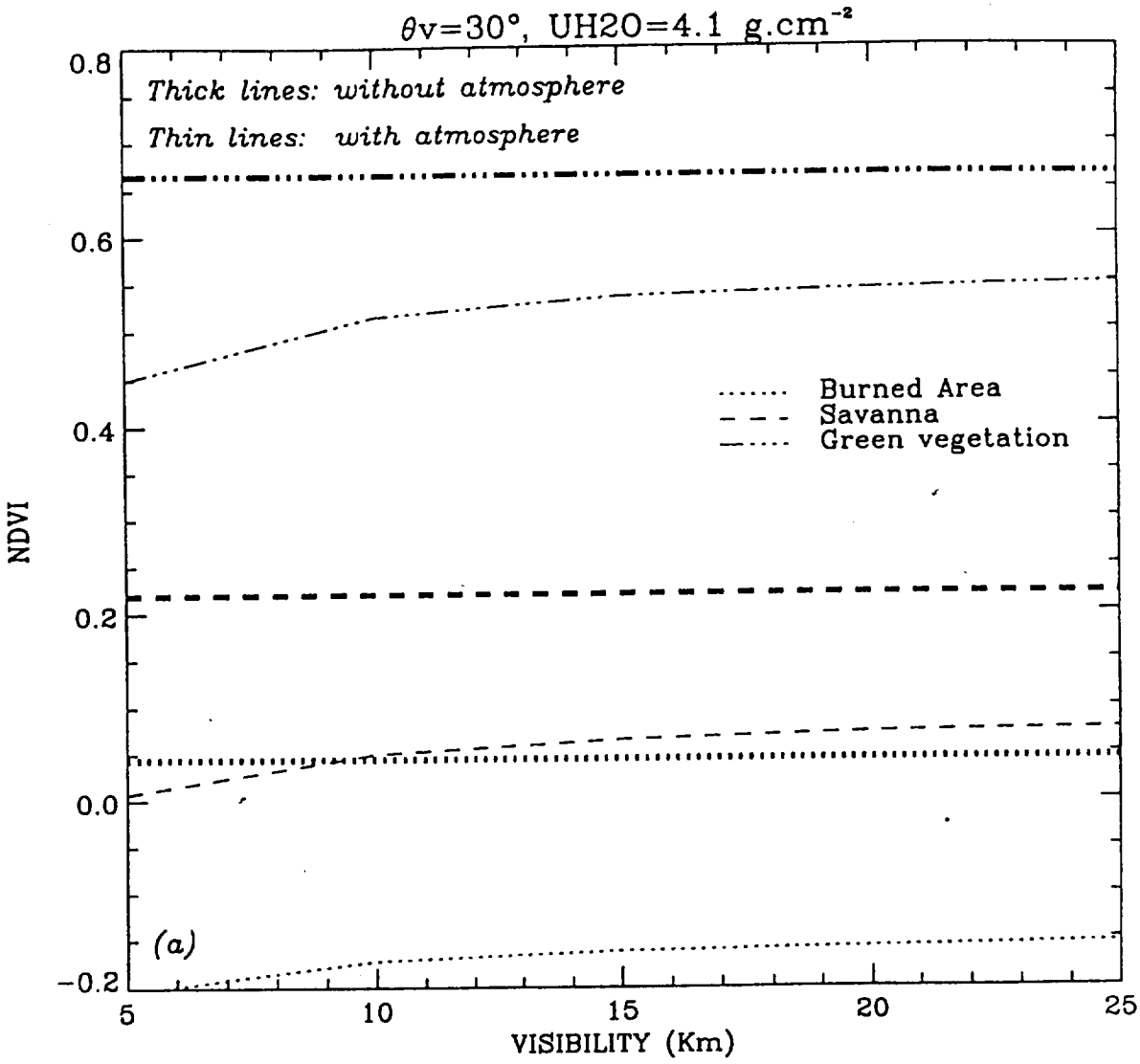
θv=30°, UH2O=4.1 g.cm⁻²
Thick lines: without atmosphere
Thin lines: with atmosphere
Burned Area
Savanna
Green vegetation
NDVI
VISIBILITY (Km)
(a)
0.8
0.6
0.4
0.2
0.0
-0.2
5
10
15
20
25

Fig. 3 (a)

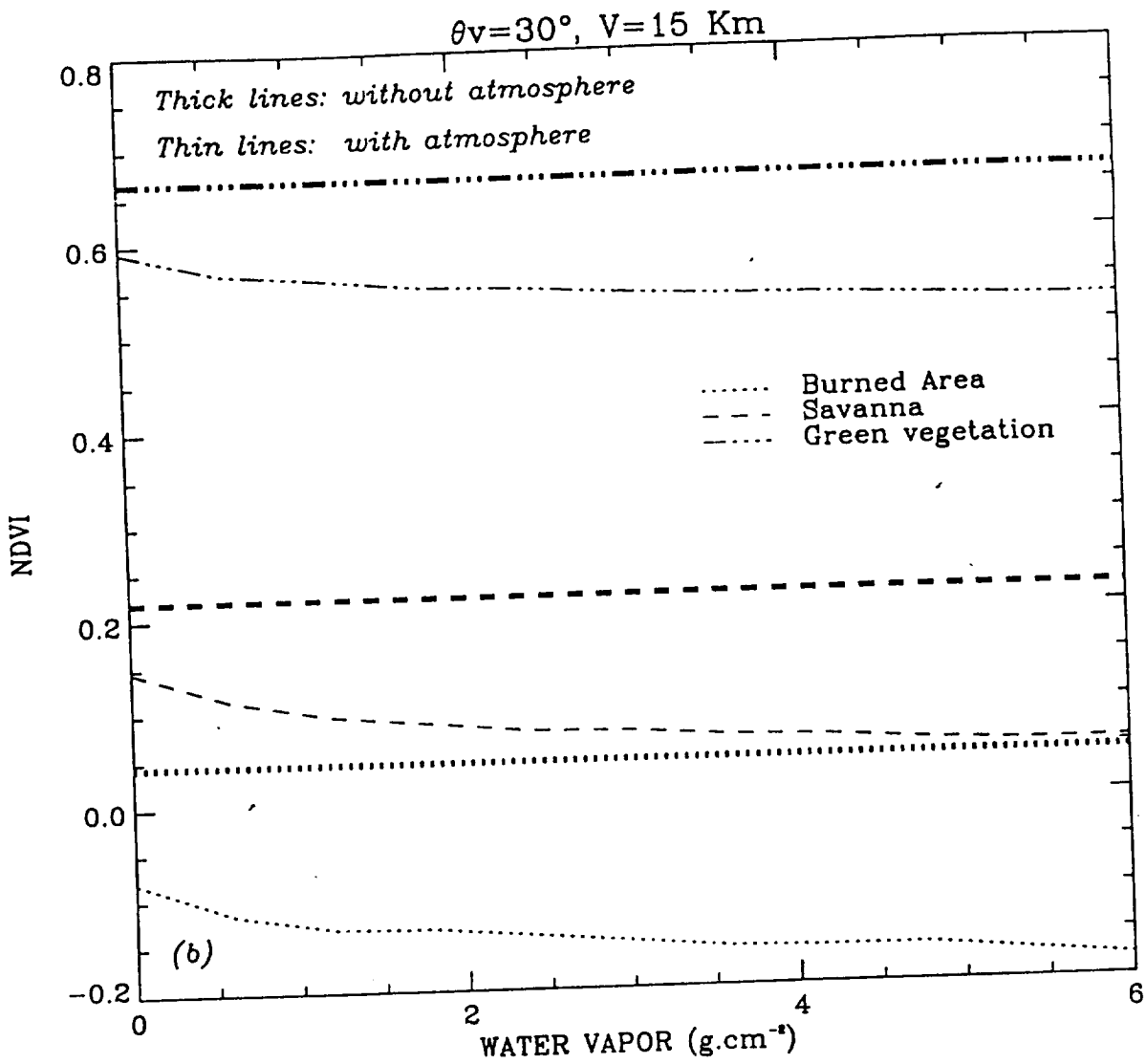
θv=30°, V=15 Km
Thick lines: without atmosphere
Thin lines: with atmosphere
Burned Area
Savanna
Green vegetation
NDVI
0.8
0.6
0.4
0.2
0.0
-0.2
0
2
4
6
WATER VAPOR (g.cm⁻²)
(b)

Fig. 3(b)

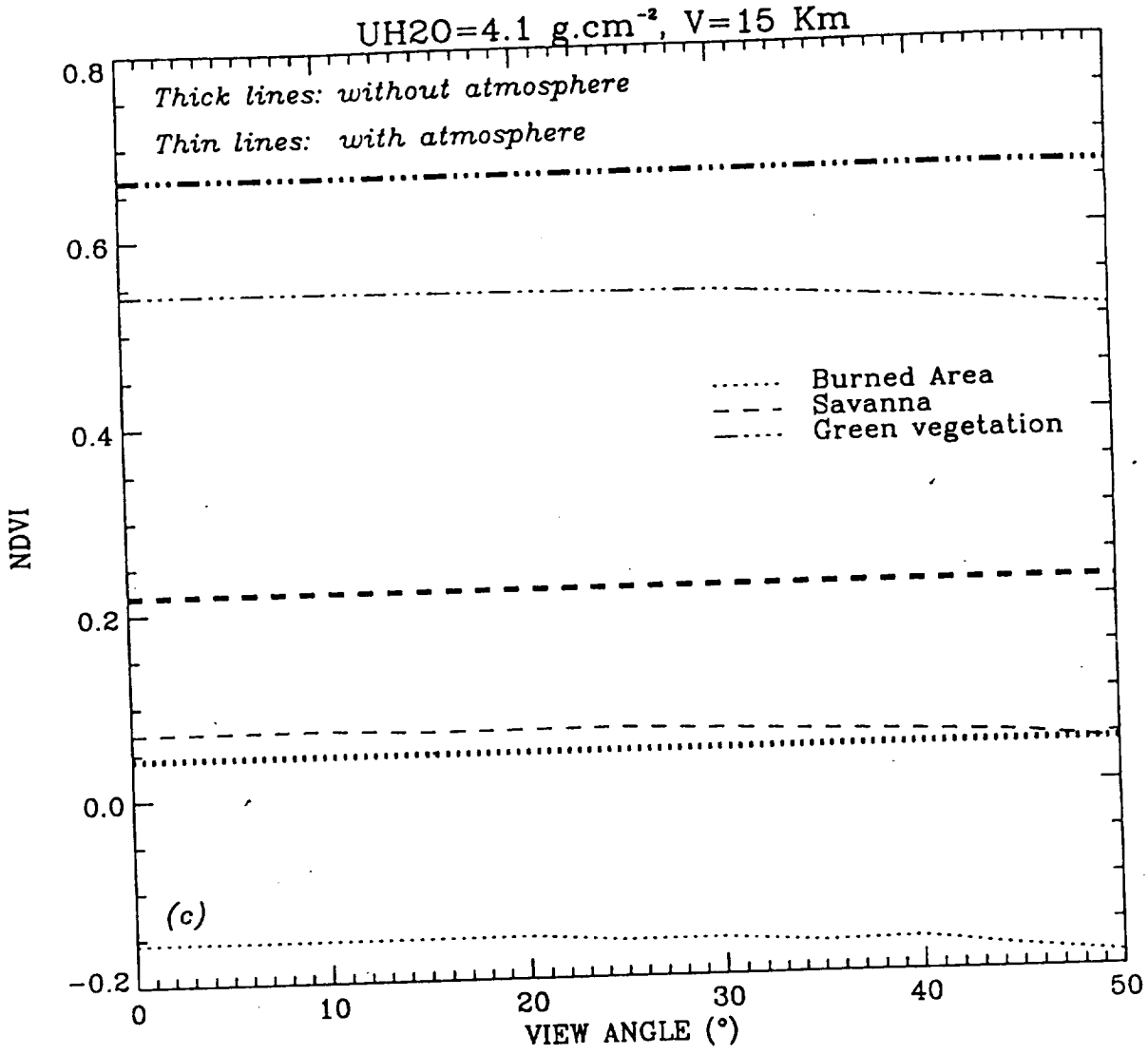
UH20=4.1 g.cm⁻², V=15 Km
Thick lines: without atmosphere
Thin lines: with atmosphere
Burned Area
Savanna
Green vegetation
(c)
NDVI
VIEW ANGLE (°)
0.8
0.6
0.4
0.2
0.0
-0.2
0
10
20
30
40
50

Fig. 3 (c)

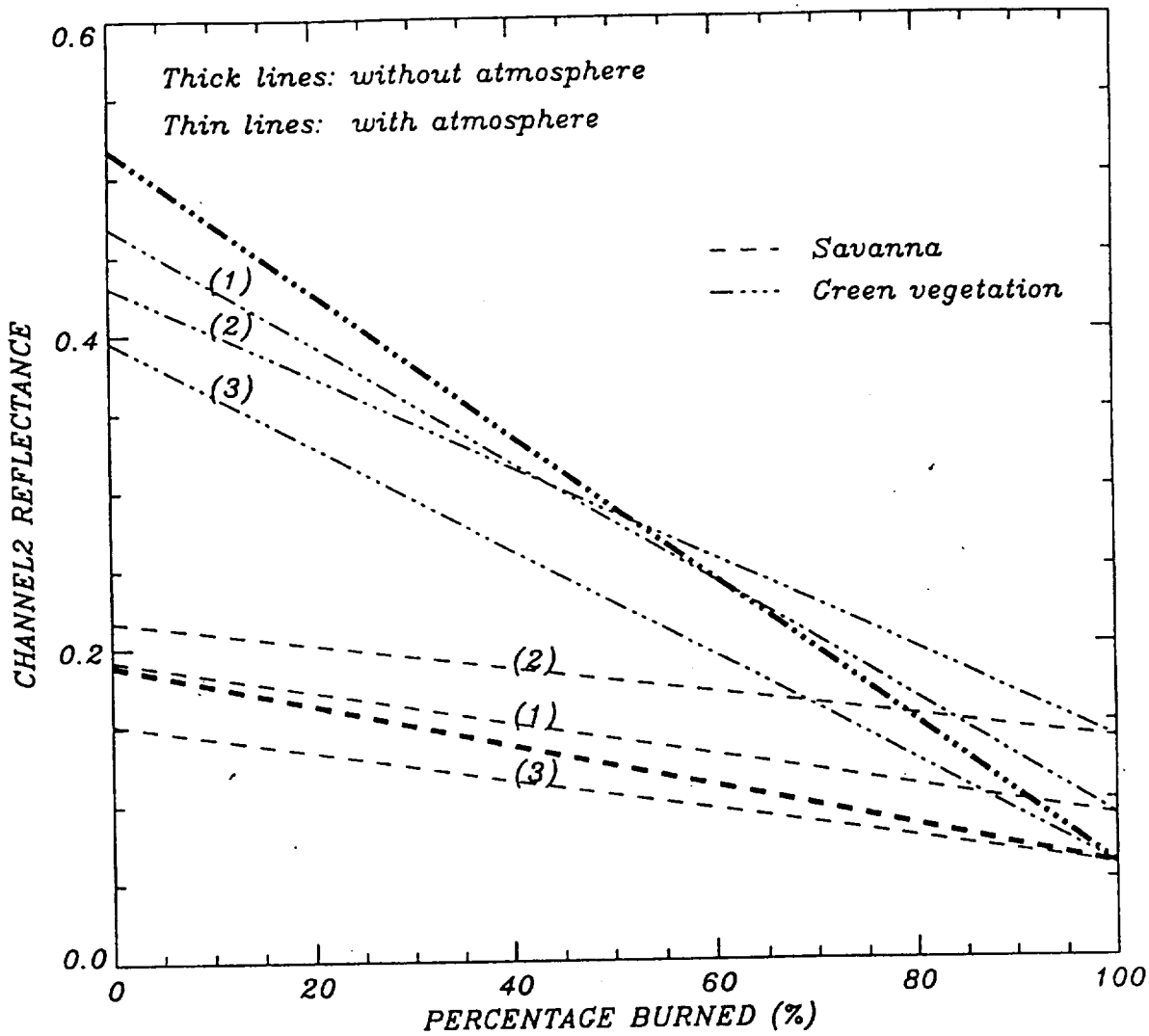
Thick lines: without atmosphere
Thin lines: with atmosphere
Savanna
Green vegetation
(1)
(2)
(3)
(2)
(1)
(3)
CHANNEL2 REFLECTANCE
0.6
0.4
0.2
0.0
0
20
40
60
80
100
PERCENTAGE BURNED (%)

Fig. 4

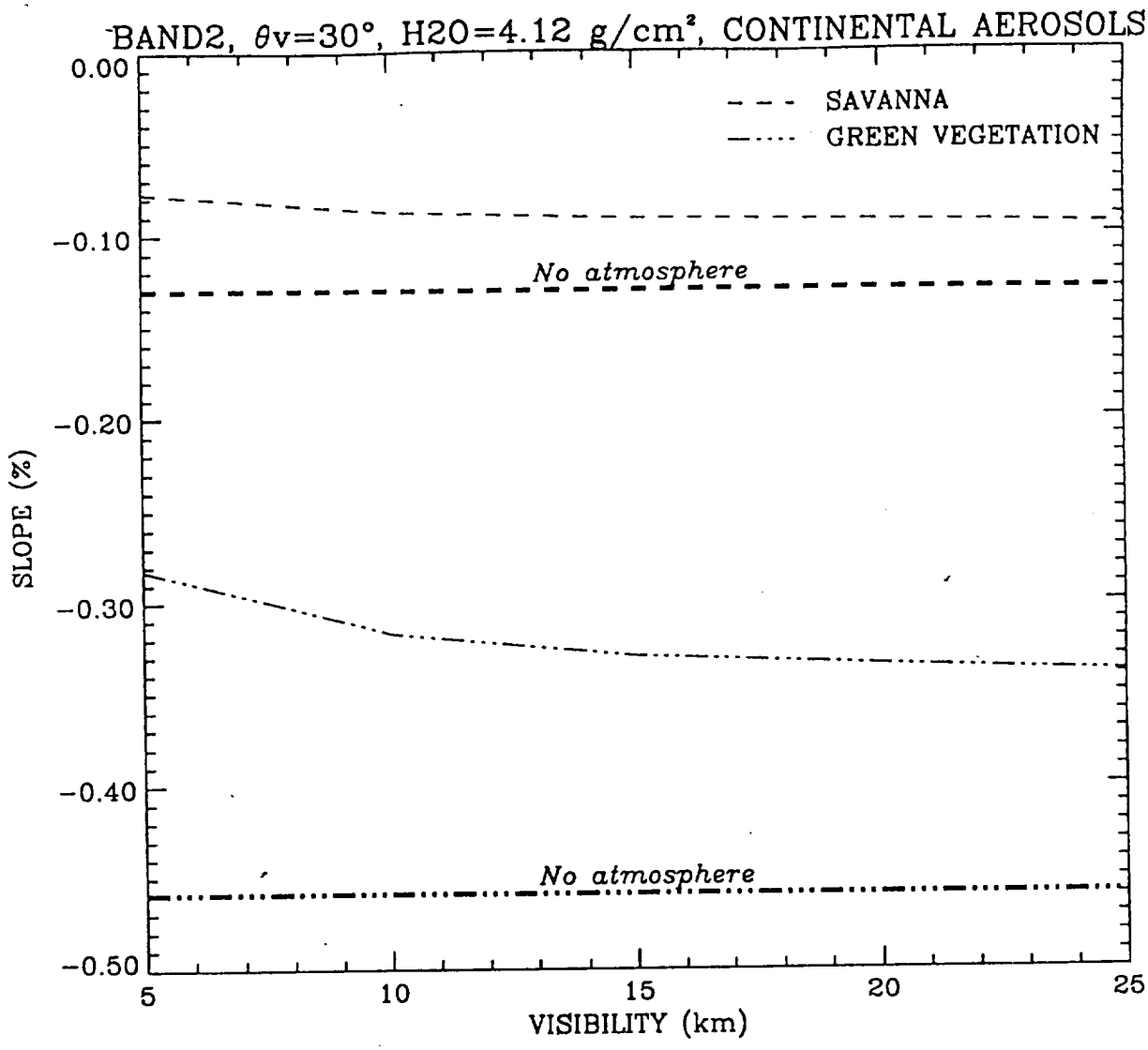
BAND2, θv=30°, H2O=4.12 g/cm², CONTINENTAL AEROSOLS
SAVANNA
GREEN VEGETATION
No atmosphere
No atmosphere
SLOPE (%)
0.00
-0.10
-0.20
-0.30
-0.40
-0.50
5
10
15
20
25
VISIBILITY (km)

Fig. 5(a)

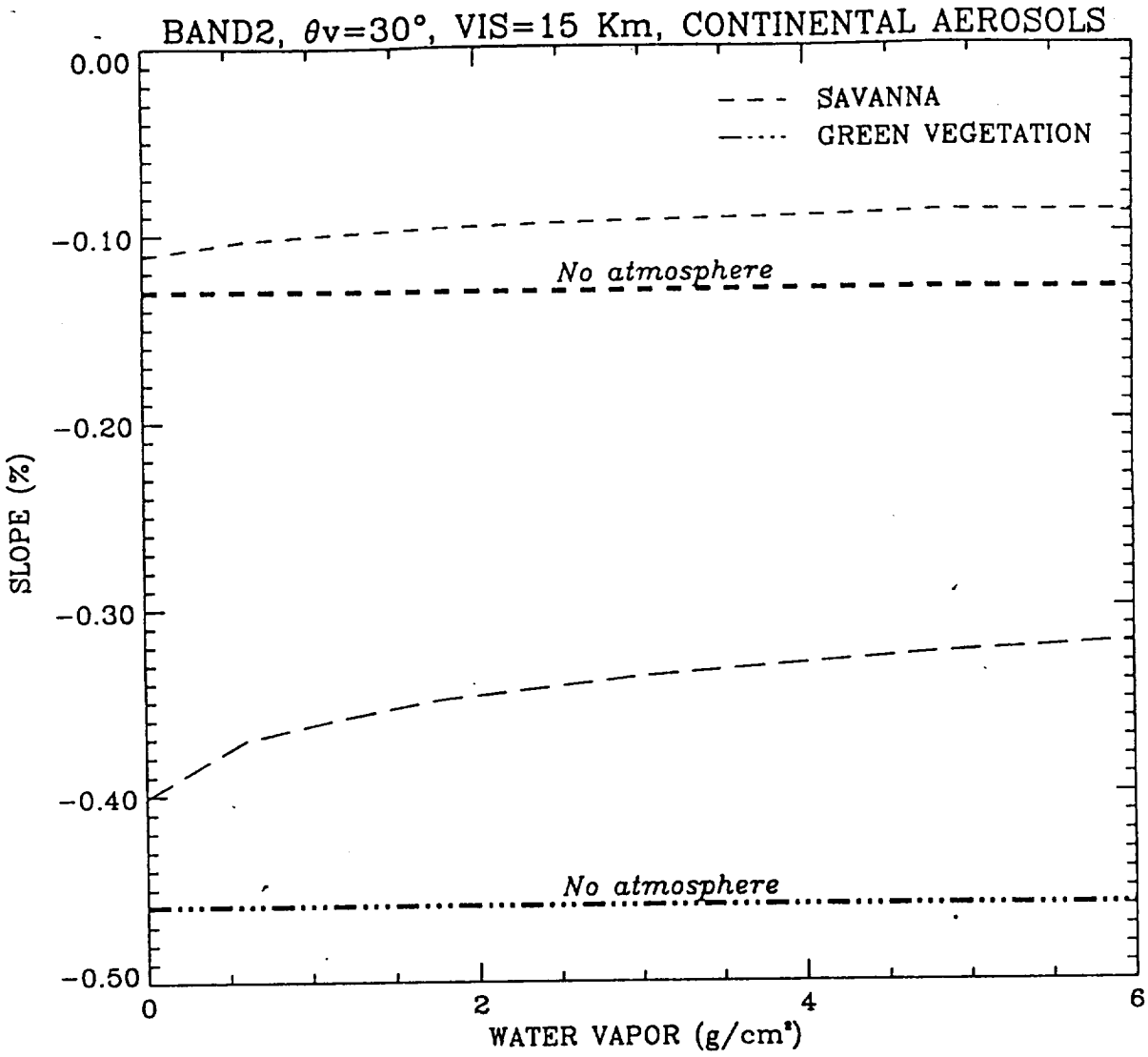
BAND2, θv=30°, VIS=15 Km, CONTINENTAL AEROSOLS
SAVANNA
GREEN VEGETATION
No atmosphere
No atmosphere
SLOPE (%)
0.00
-0.10
-0.20
-0.30
-0.40
-0.50
0
2
4
6
WATER VAPOR (g/cm²)

Fig. 5 (b)

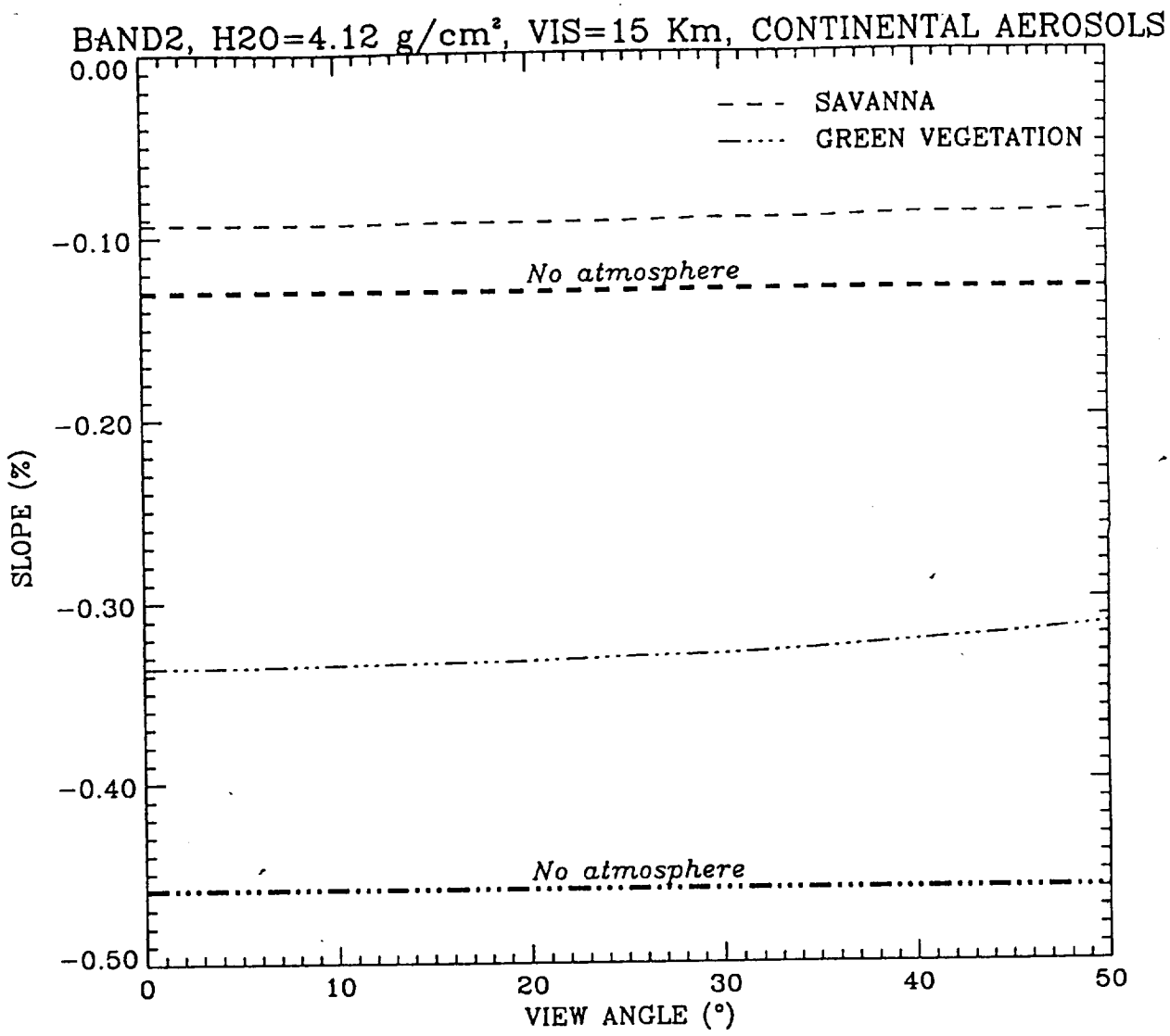
BAND2, H2O=4.12 g/cm², VIS=15 Km, CONTINENTAL AEROSOLS
SAVANNA
GREEN VEGETATION
No atmosphere
No atmosphere
SLOPE (%)
0.00
-0.10
-0.20
-0.30
-0.40
-0.50
0
10
20
30
40
50
VIEW ANGLE (°)

Fig. 5(c)

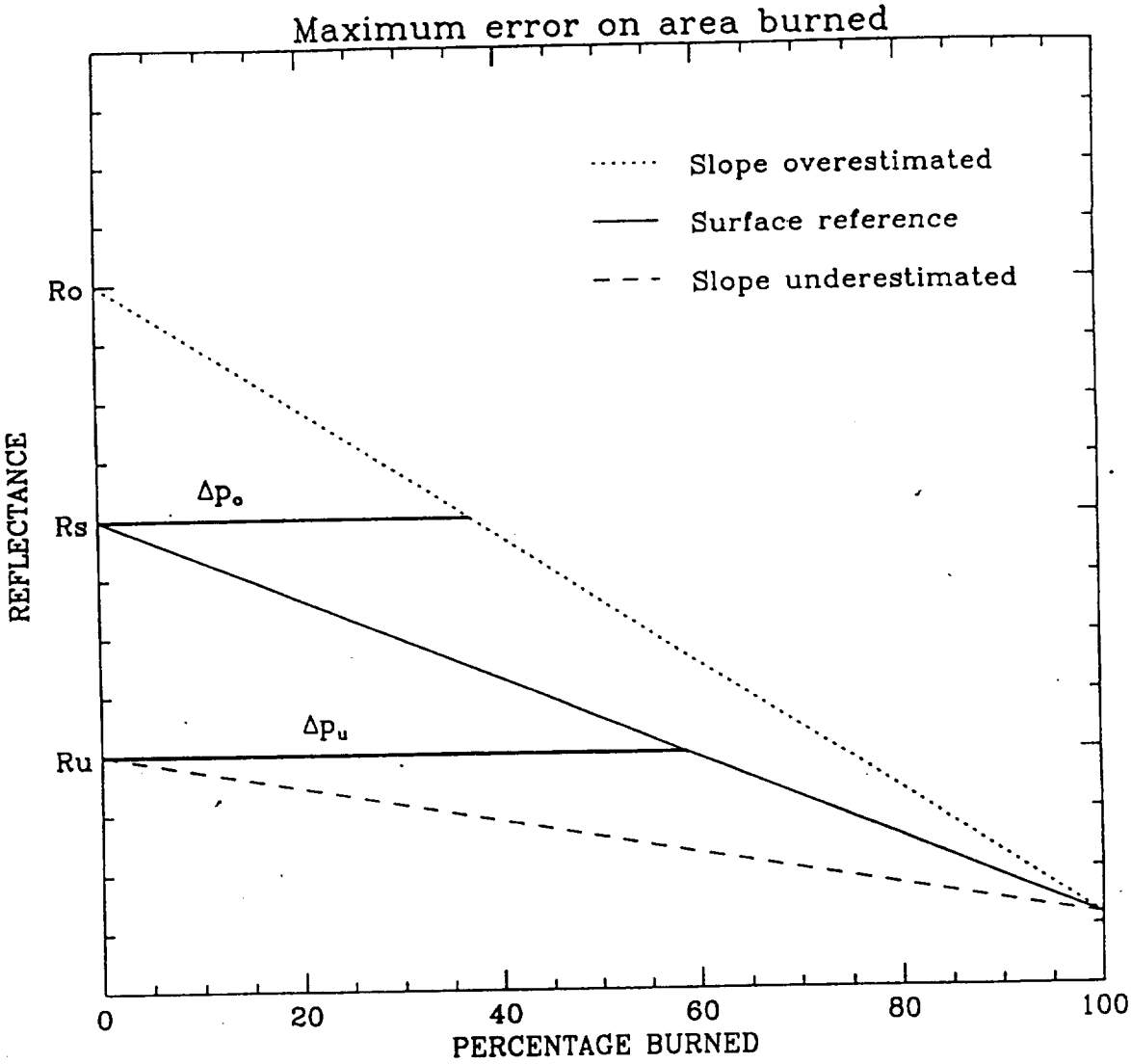
Maximum error on area burned
Slope overestimated
Surface reference
Slope underestimated
Ro
Rs
Ru
Δp_o
Δp_u
REFLECTANCE
0
20
40
60
80
100
PERCENTAGE BURNED

Fig. 6

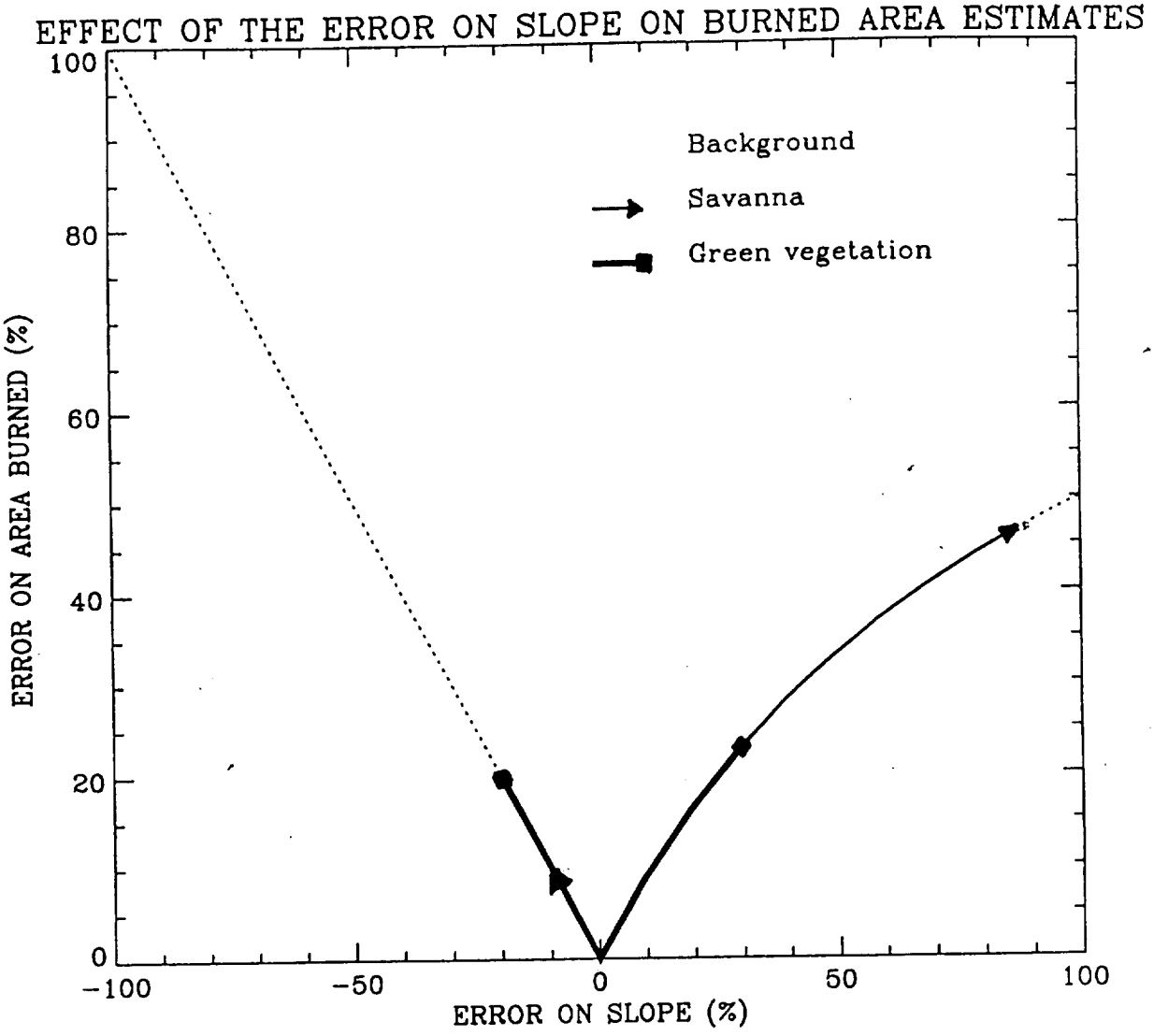
EFFECT OF THE ERROR ON SLOPE ON BURNED AREA ESTIMATES
Background
Savanna
Green vegetation
ERROR ON AREA BURNED (%)
ERROR ON SLOPE (%)
100
80
60
40
20
0
-100
-50
0
50
100

Fig. 7

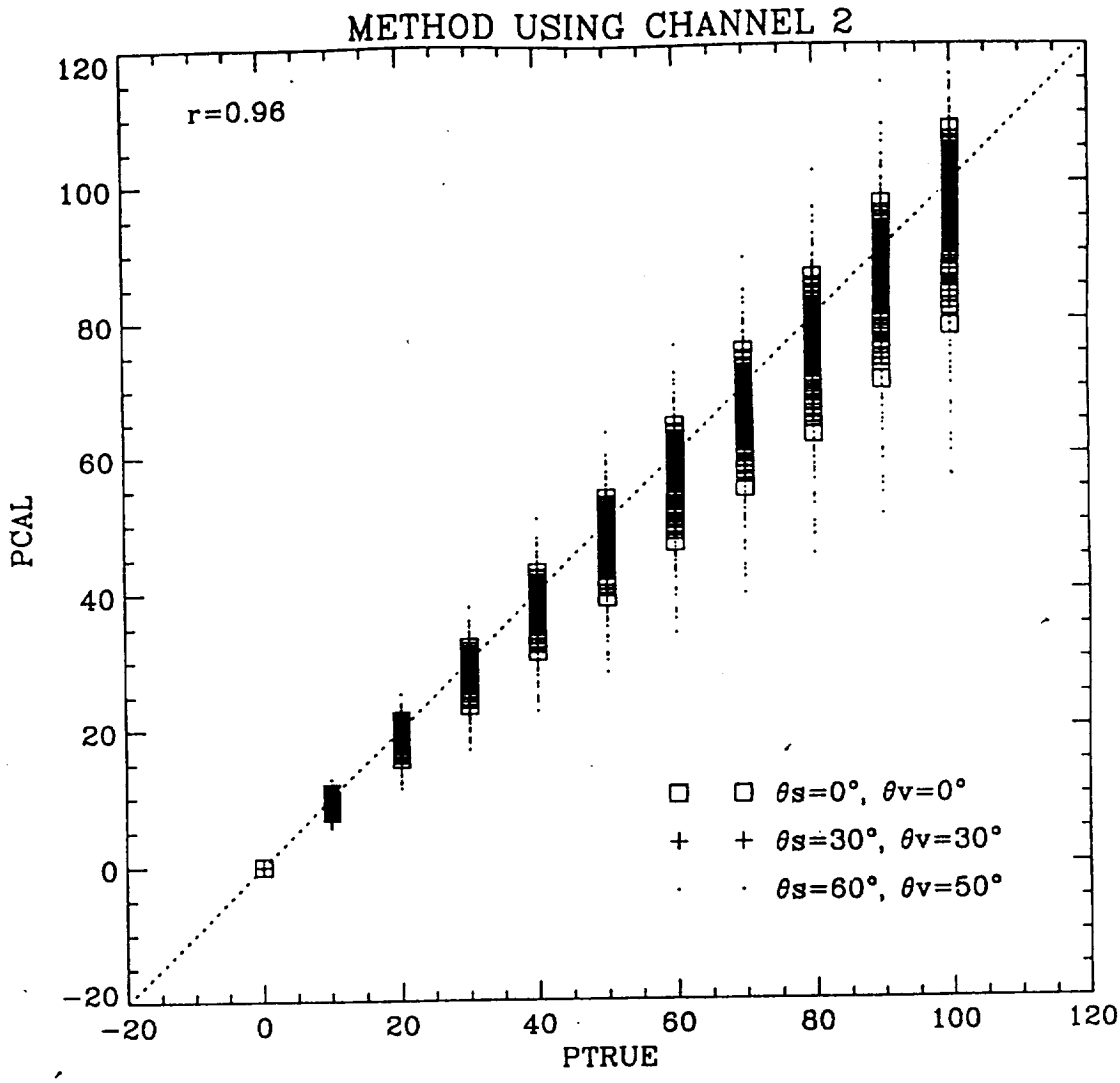
METHOD USING CHANNEL 2
r=0.96
PCAL
PTRUE
120
100
80
60
40
20
0
-20
-20
0
20
40
60
80
100
120
θs=0°, θv=0°
θs=30°, θv=30°
θs=60°, θv=50°

Fig. 8

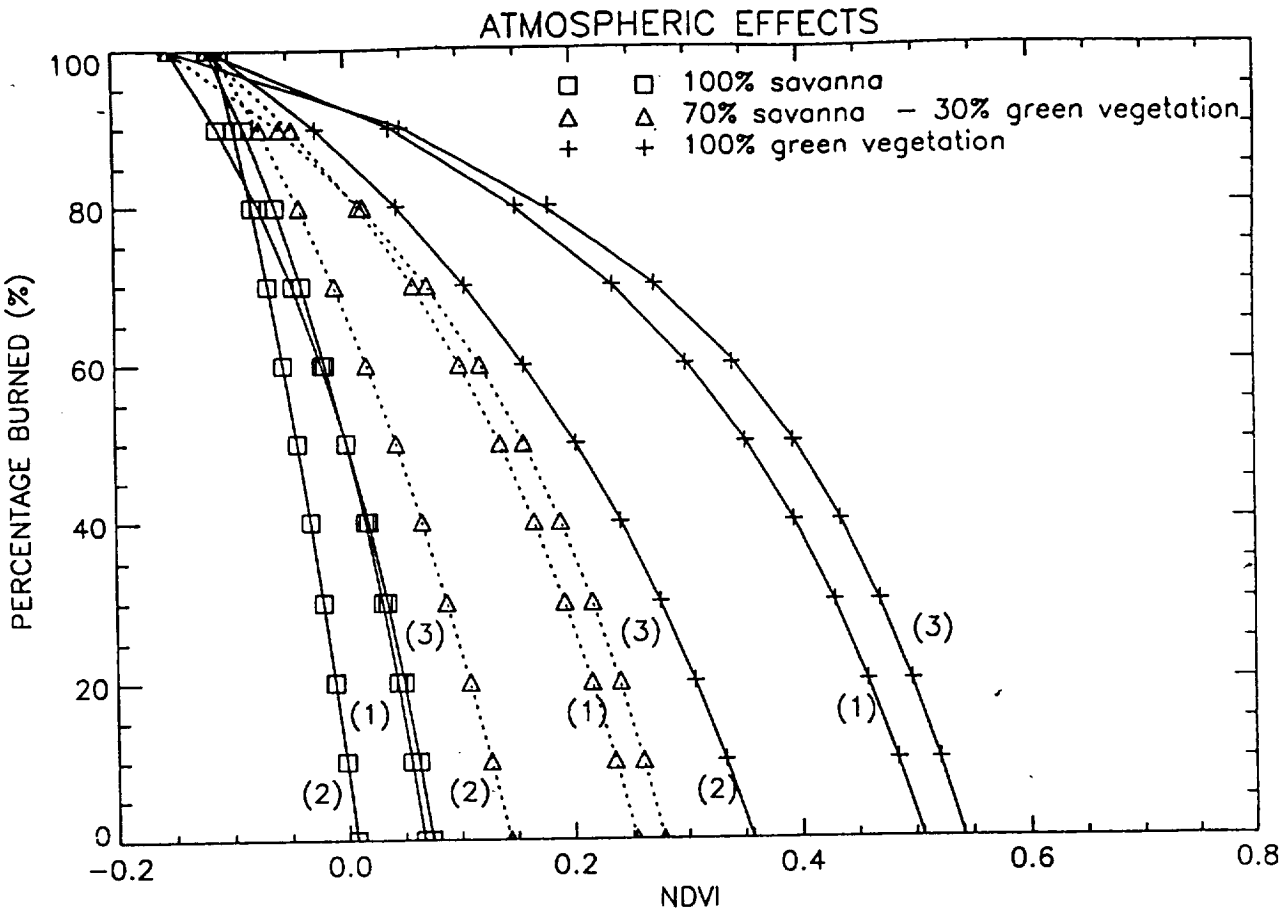
ATMOSPHERIC EFFECTS
100% savanna
70% savanna – 30% green vegetation
100% green vegetation
PERCENTAGE BURNED (%)
NDVI
100
80
60
40
20
0
−0.2
0.0
0.2
0.4
0.6
0.8
(1)
(2)
(3)

Fig. 9

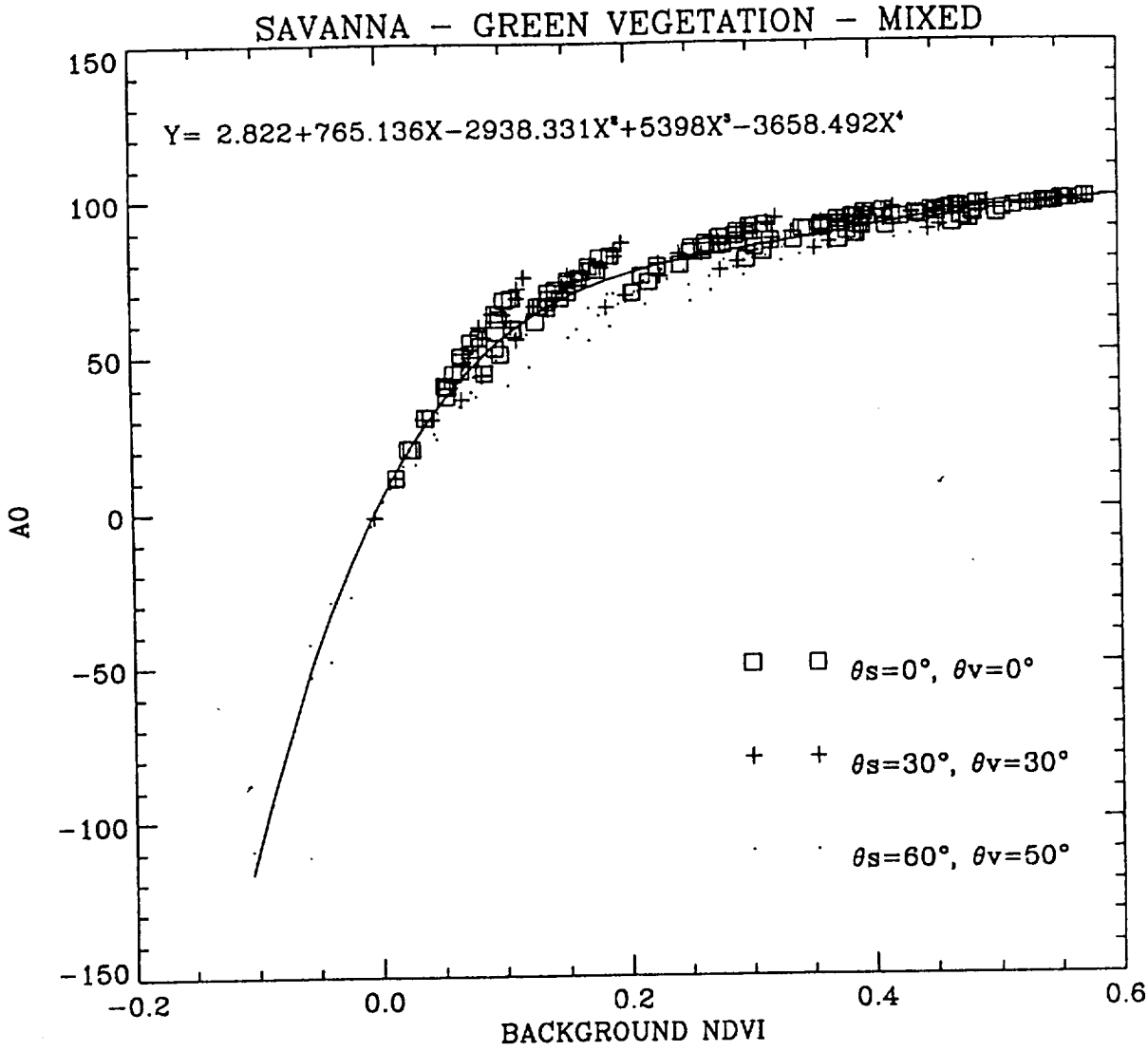
SAVANNA – GREEN VEGETATION – MIXED
Y= 2.822+765.136X−2938.331X²+5398X³−3658.492X⁴
150
100
50
0
−50
−100
−150
AO
−0.2
0.0
0.2
0.4
0.6
BACKGROUND NDVI
θs=0°, θv=0°
θs=30°, θv=30°
θs=60°, θv=50°

Fig. 10 (a)

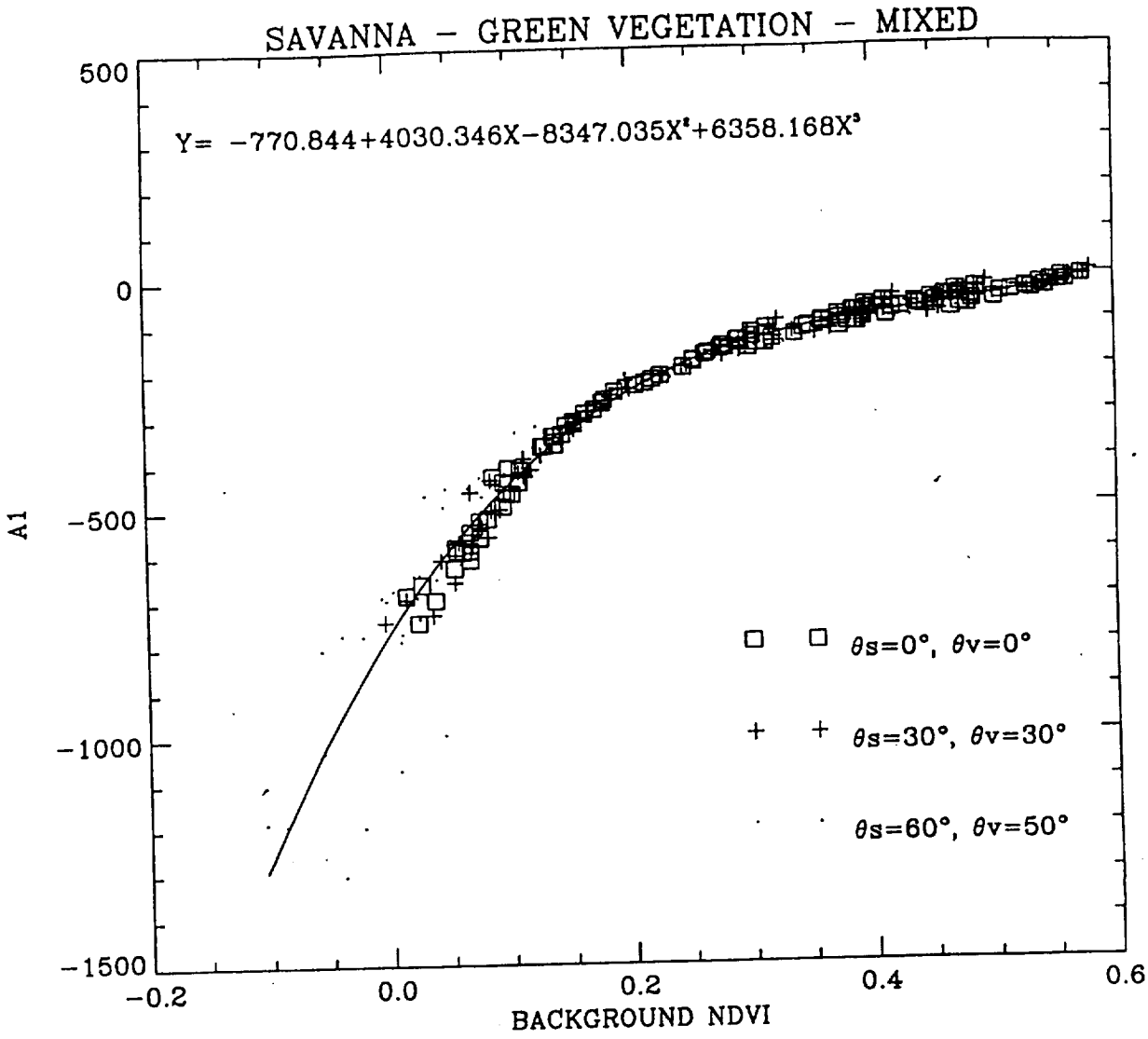
SAVANNA – GREEN VEGETATION – MIXED
Y= −770.844+4030.346X−8347.035X²+6358.168X³
500
0
−500
−1000
−1500
A1
−0.2
0.0
0.2
0.4
0.6
BACKGROUND NDVI
θs=0°, θv=0°
θs=30°, θv=30°
θs=60°, θv=50°

Fig.10 (b)

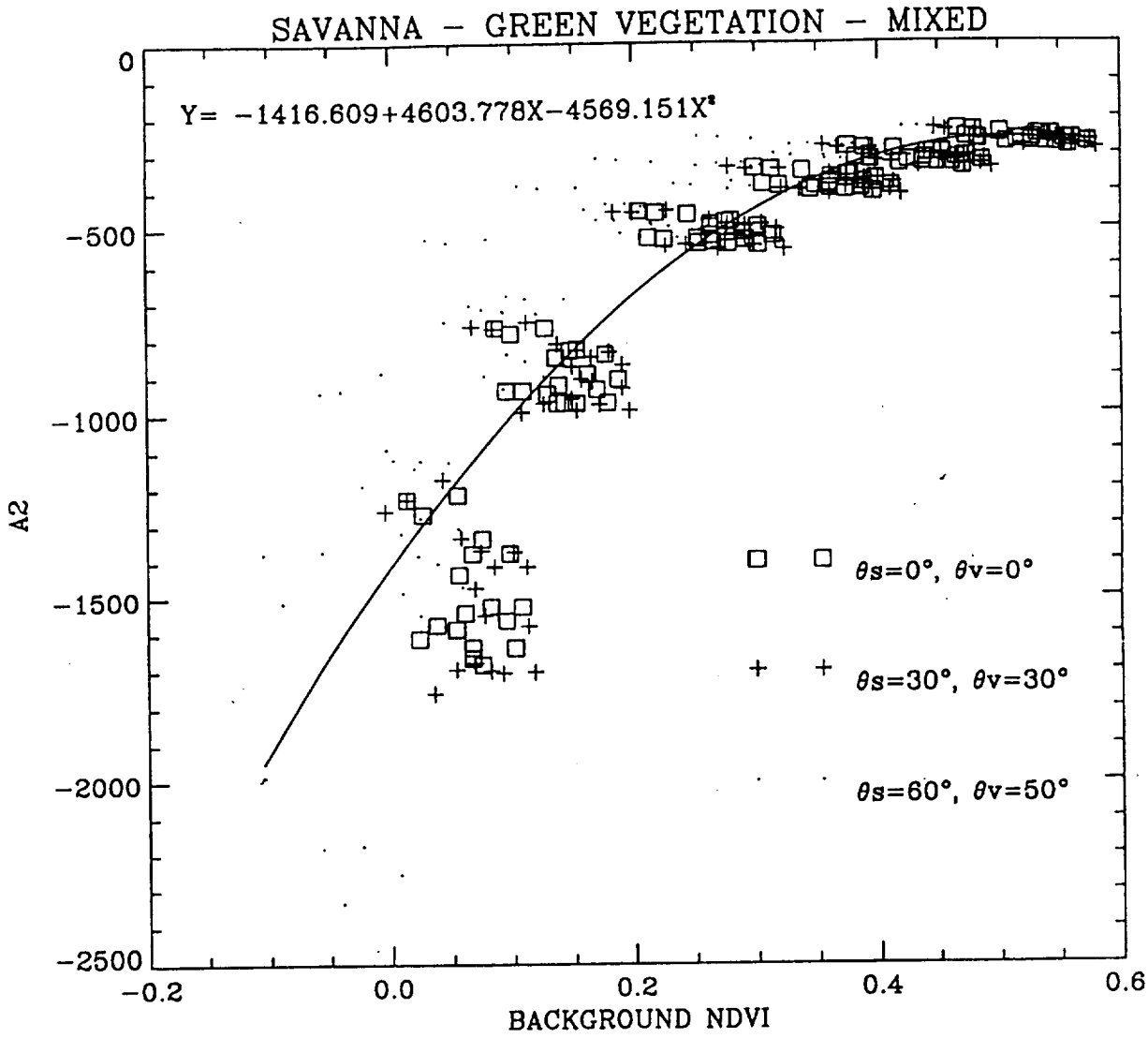
SAVANNA – GREEN VEGETATION – MIXED
Y= −1416.609+4603.778X−4569.151X²
A2
BACKGROUND NDVI
0
−500
−1000
−1500
−2000
−2500
−0.2
0.0
0.2
0.4
0.6
θs=0°, θv=0°
θs=30°, θv=30°
θs=60°, θv=50°

Fig. 10 (c)

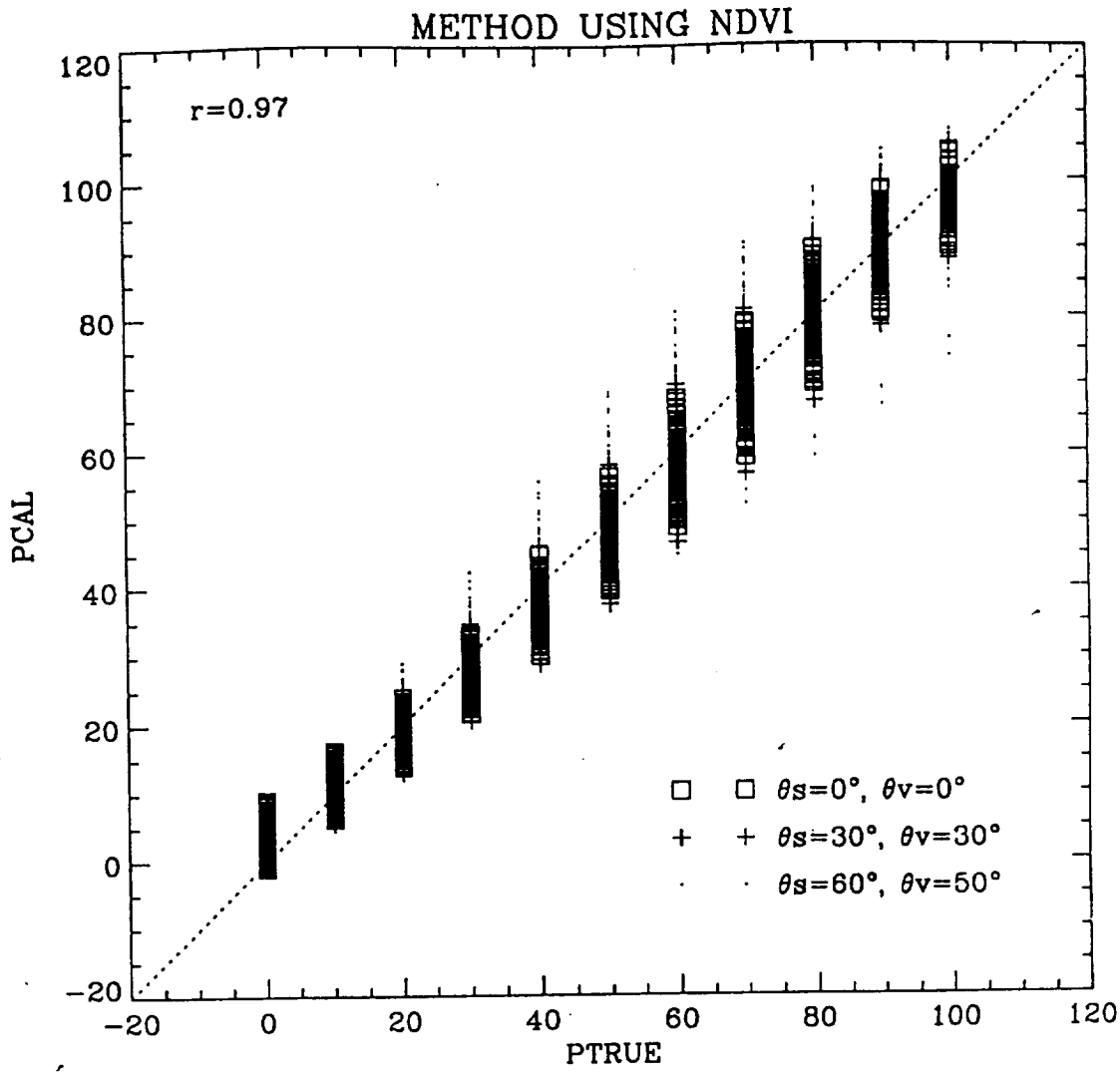
METHOD USING NDVI
r=0.97
PCAL
PTRUE
120
100
80
60
40
20
0
-20
-20
0
20
40
60
80
100
120
θs=0°, θv=0°
θs=30°, θv=30°
θs=60°, θv=50°

Fig. 11

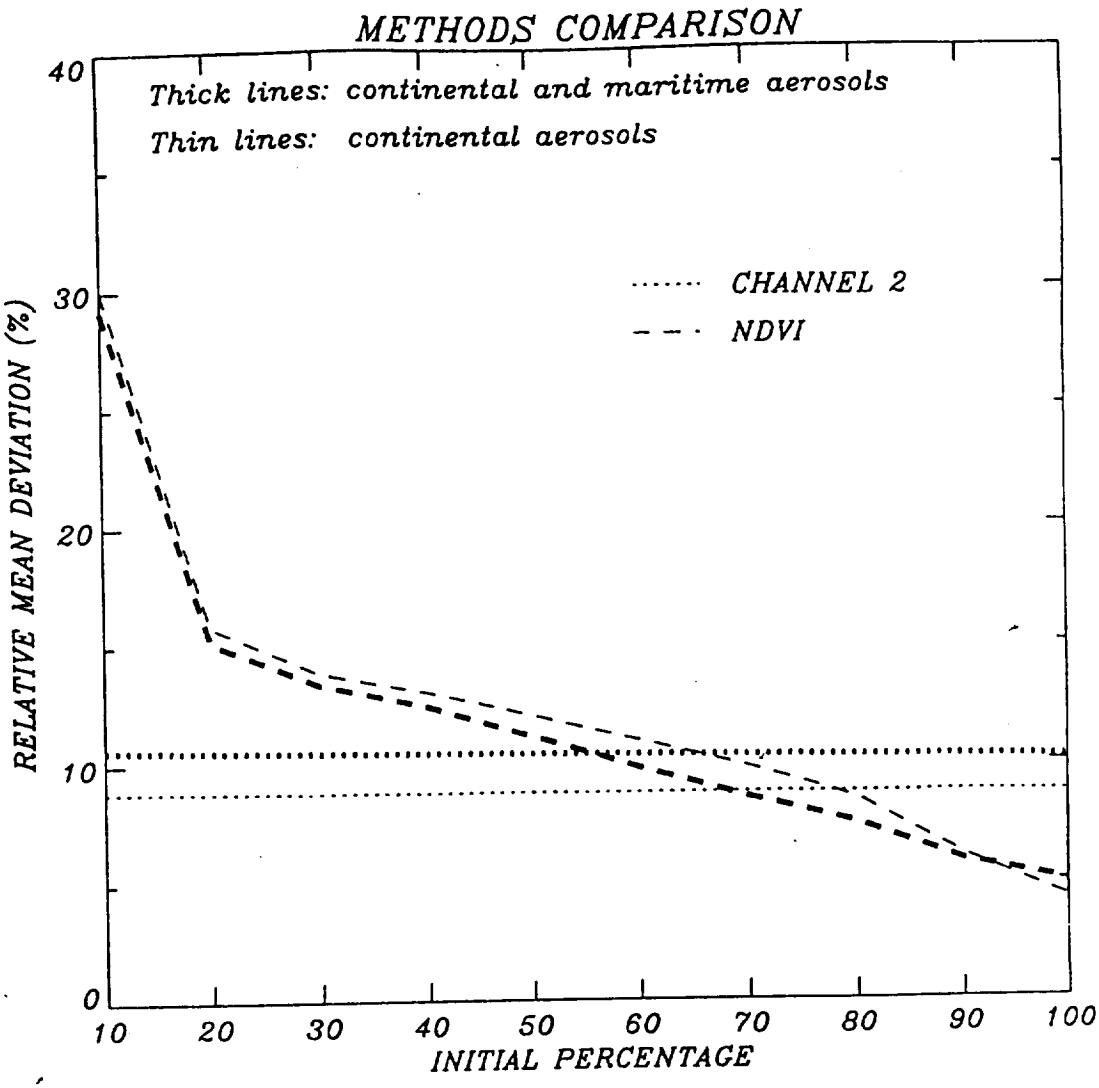
METHODS COMPARISON
Thick lines: continental and maritime aerosols
Thin lines: continental aerosols
CHANNEL 2
NDVI
RELATIVE MEAN DEVIATION (%)
INITIAL PERCENTAGE
0
10
20
30
40
10
20
30
40
50
60
70
80
90
100

Fig. 12

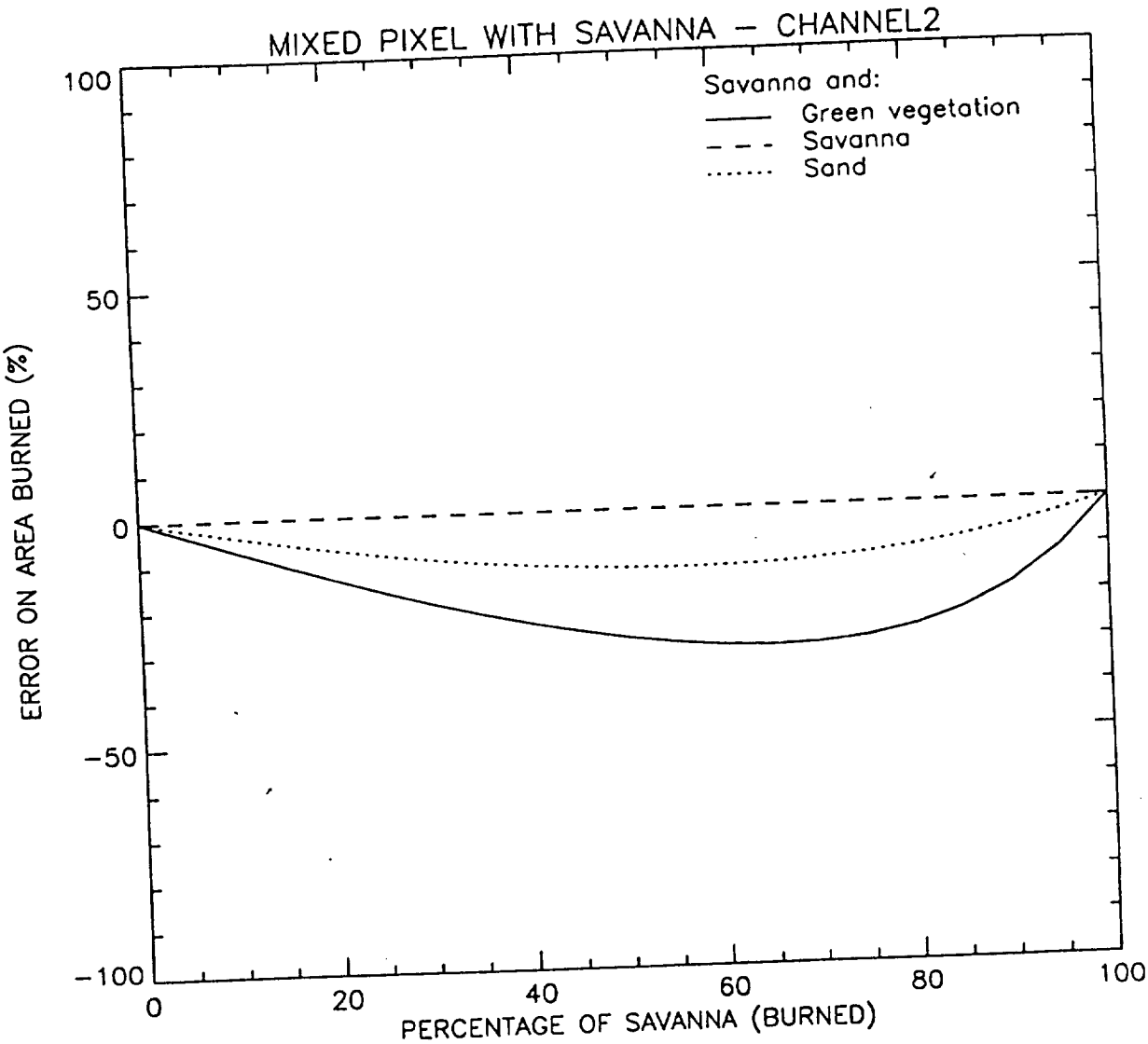
MIXED PIXEL WITH SAVANNA – CHANNEL2
Savanna and:
Green vegetation
Savanna
Sand
ERROR ON AREA BURNED (%)
100
50
0
-50
-100
0
20
40
60
80
100
PERCENTAGE OF SAVANNA (BURNED)

Fig. 13 (a)

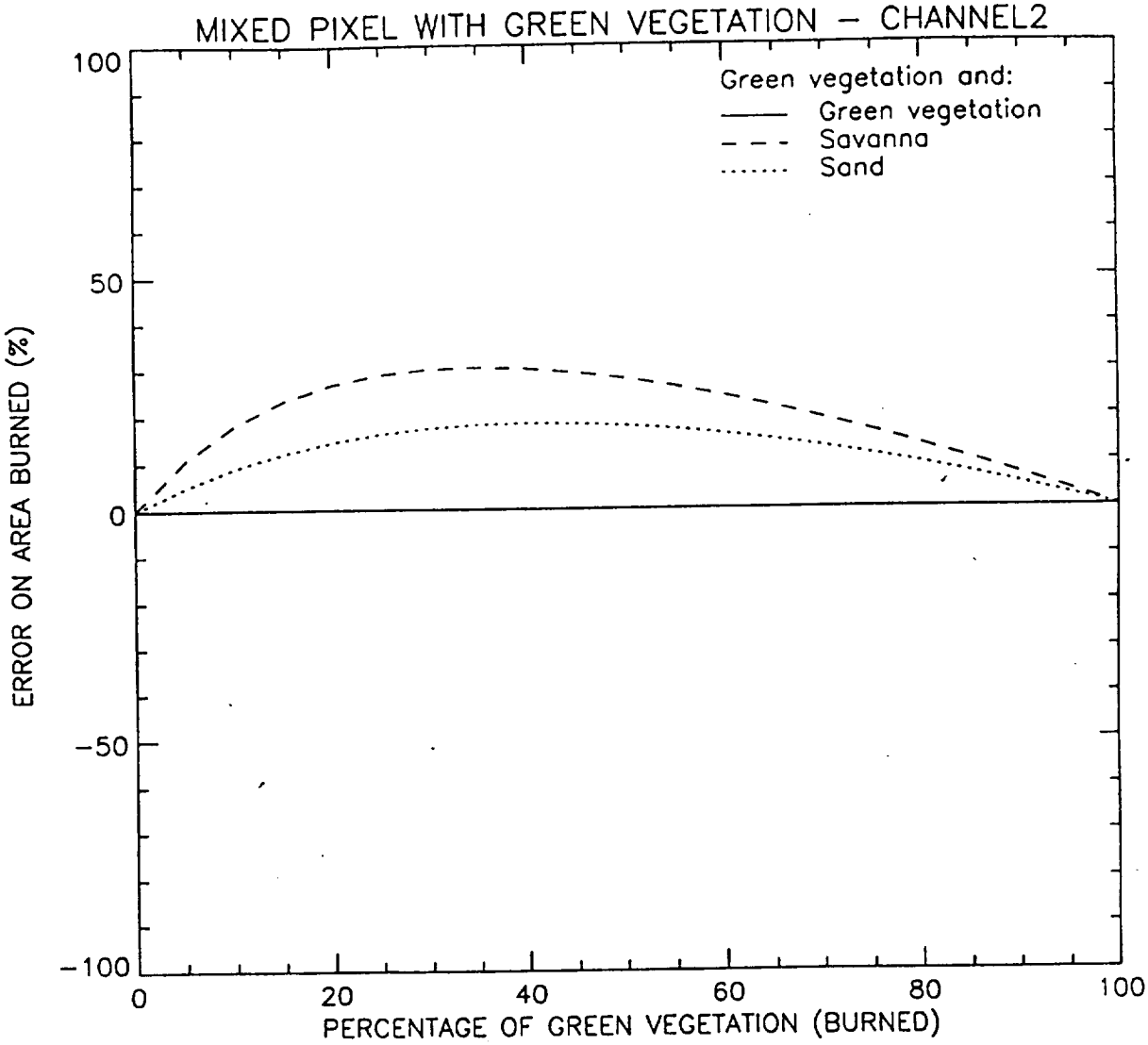
MIXED PIXEL WITH GREEN VEGETATION – CHANNEL2
Green vegetation and:
Green vegetation
Savanna
Sand
100
50
0
-50
-100
ERROR ON AREA BURNED (%)
0
20
40
60
80
100
PERCENTAGE OF GREEN VEGETATION (BURNED)

Fig. 13(b)

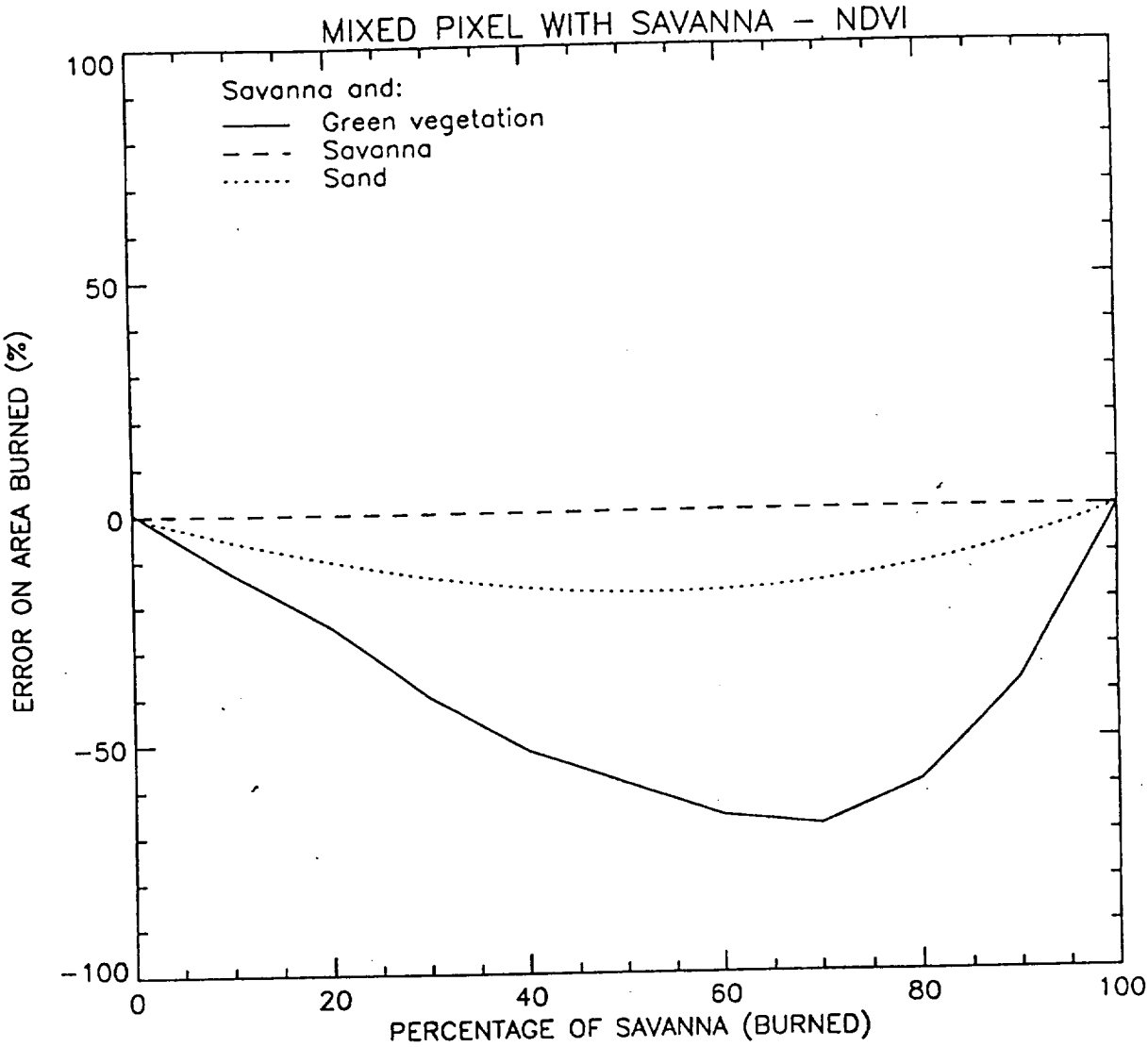
MIXED PIXEL WITH SAVANNA – NDVI
Savanna and:
Green vegetation
Savanna
Sand
ERROR ON AREA BURNED (%)
100
50
0
-50
-100
0
20
40
60
80
100
PERCENTAGE OF SAVANNA (BURNED)

Fig. 14 (a)

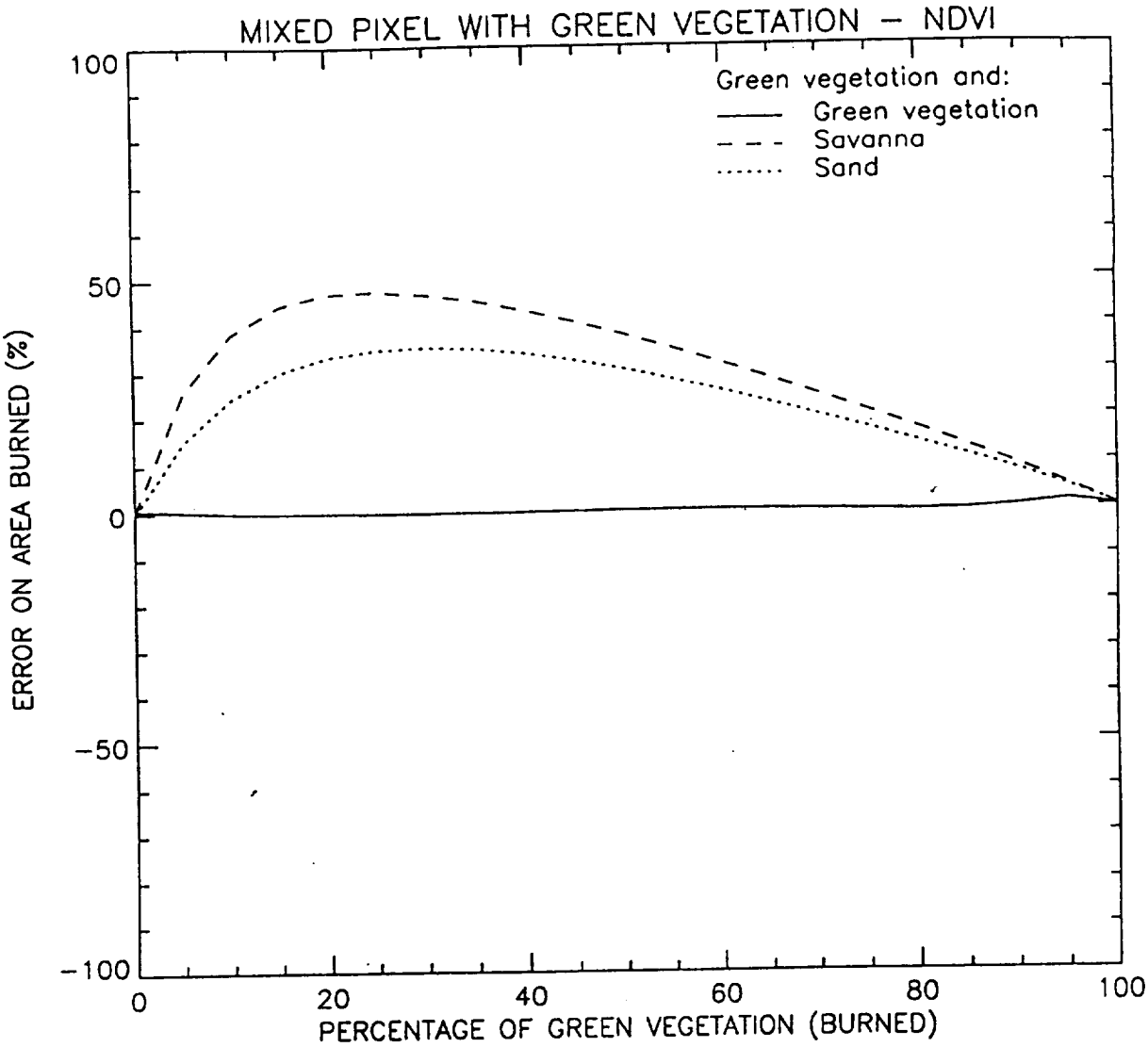
MIXED PIXEL WITH GREEN VEGETATION – NDVI
Green vegetation and:
Green vegetation
Savanna
Sand
ERROR ON AREA BURNED (%)
100
50
0
−50
−100
0
20
40
60
80
100
PERCENTAGE OF GREEN VEGETATION (BURNED)

Fig. 14 (b)

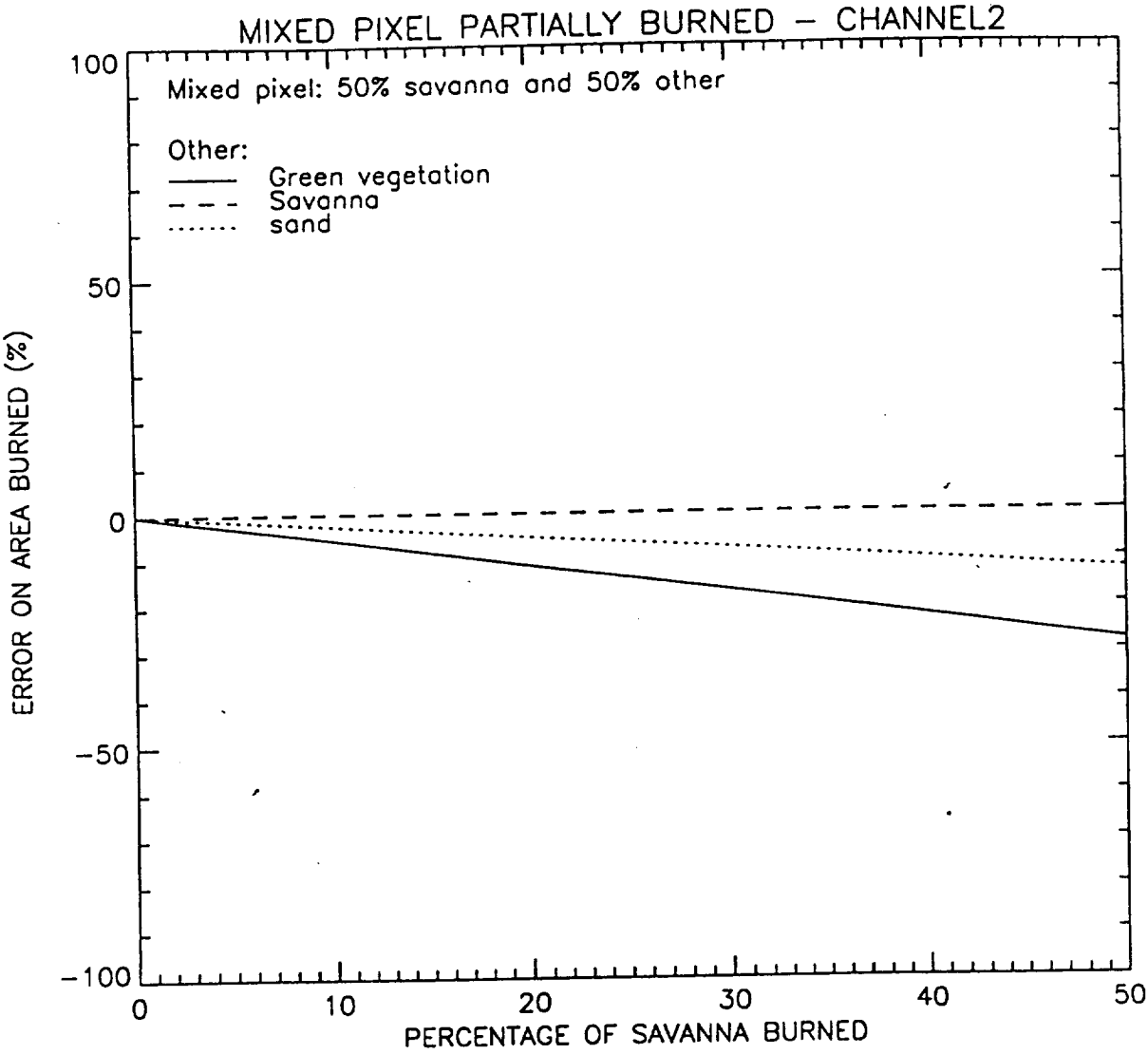
MIXED PIXEL PARTIALLY BURNED – CHANNEL2
Mixed pixel: 50% savanna and 50% other
Other:
Green vegetation
Savanna
sand
ERROR ON AREA BURNED (%)
100
50
0
−50
−100
0
10
20
30
40
50
PERCENTAGE OF SAVANNA BURNED

Fig. 15 (a)

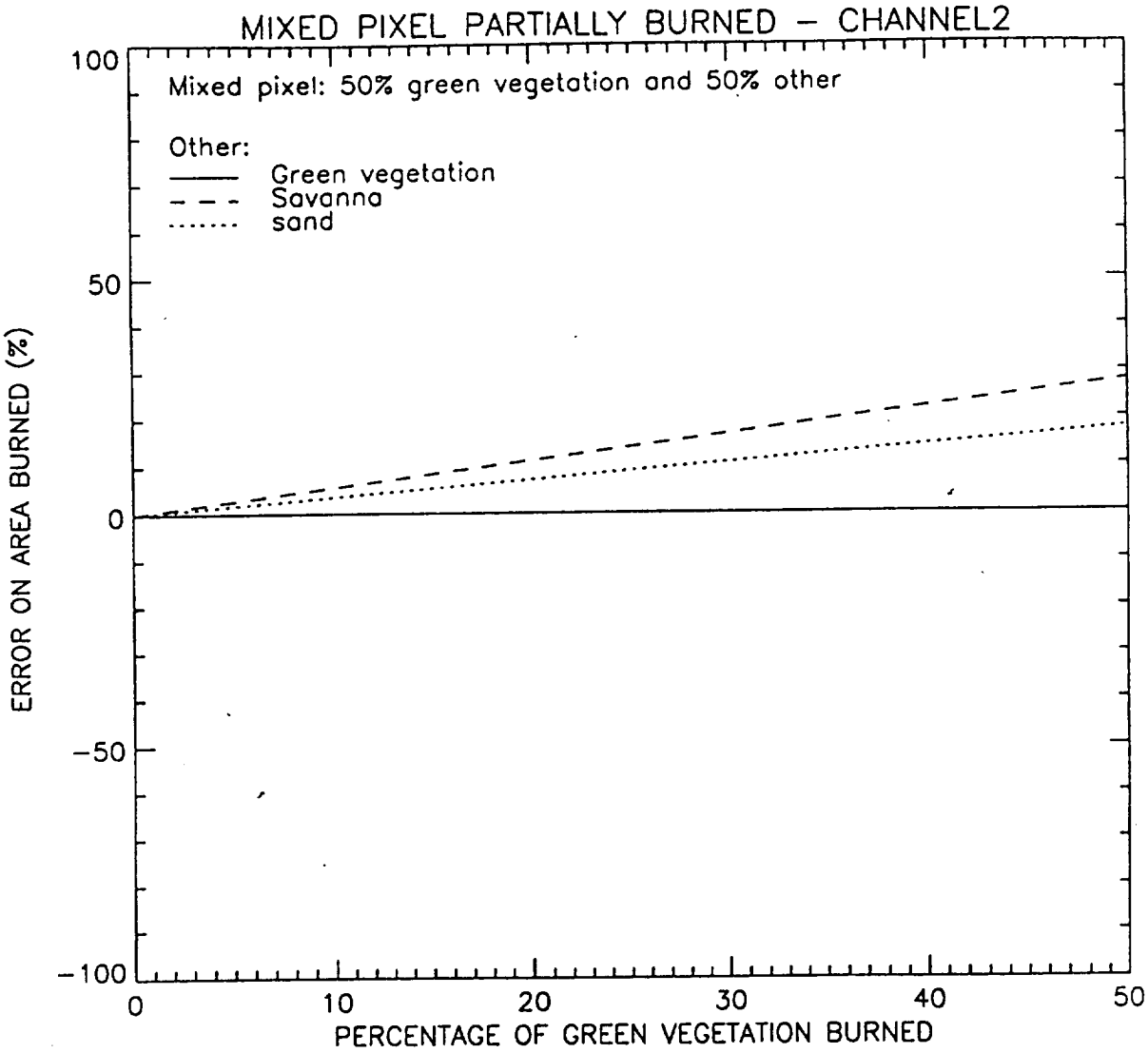
MIXED PIXEL PARTIALLY BURNED – CHANNEL2
Mixed pixel: 50% green vegetation and 50% other
Other:
Green vegetation
Savanna
sand
ERROR ON AREA BURNED (%)
100
50
0
−50
−100
0
10
20
30
40
50
PERCENTAGE OF GREEN VEGETATION BURNED

Fig. 15 (b)

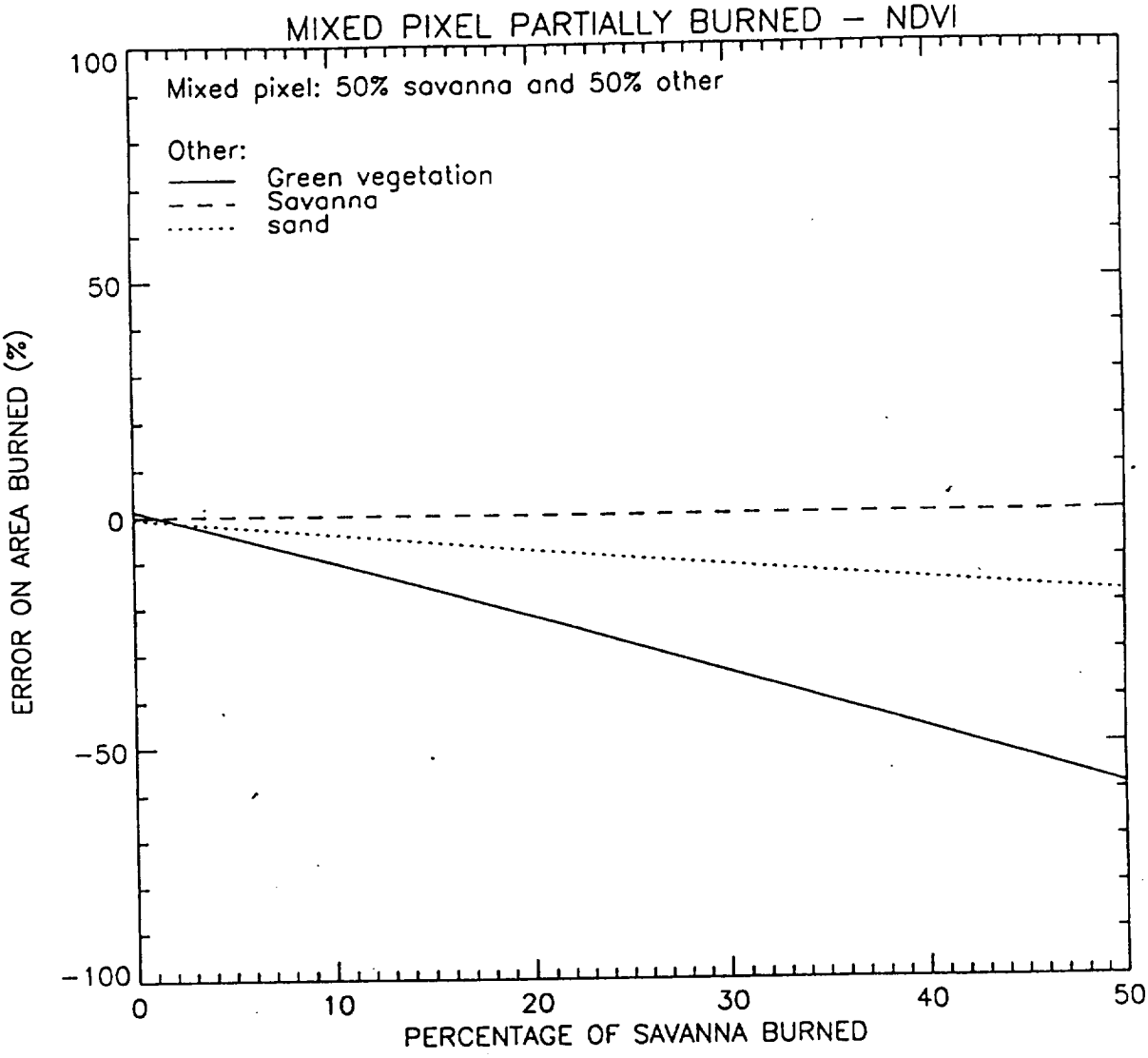
MIXED PIXEL PARTIALLY BURNED – NDVI
Mixed pixel: 50% savanna and 50% other
Other:
Green vegetation
Savanna
sand
ERROR ON AREA BURNED (%)
100
50
0
−50
−100
0
10
20
30
40
50
PERCENTAGE OF SAVANNA BURNED

Fig. 16(a)

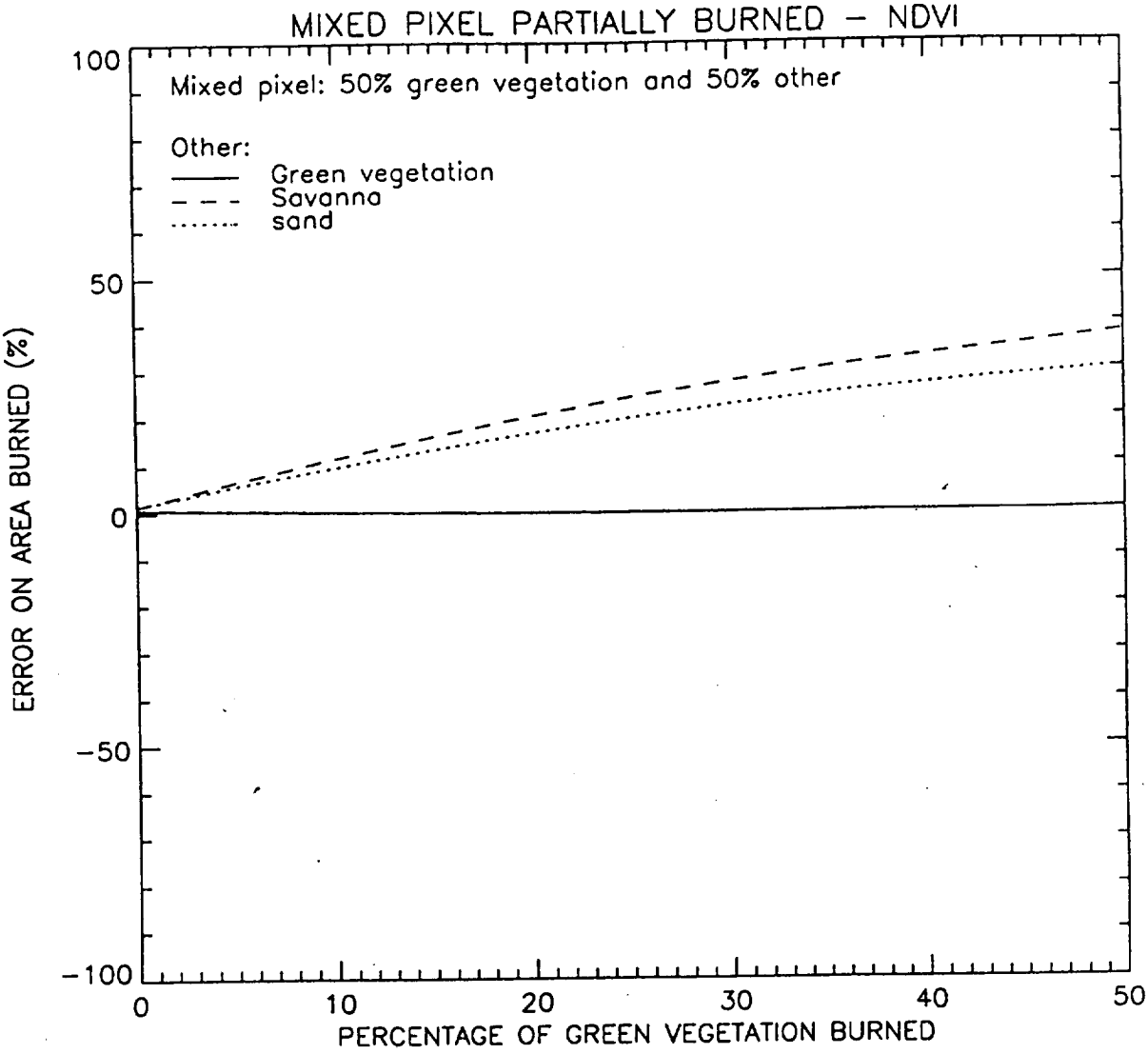
MIXED PIXEL PARTIALLY BURNED – NDVI
Mixed pixel: 50% green vegetation and 50% other
Other:
Green vegetation
Savanna
sand
ERROR ON AREA BURNED (%)
100
50
0
−50
−100
0
10
20
30
40
50
PERCENTAGE OF GREEN VEGETATION BURNED

Fig. 16(b)

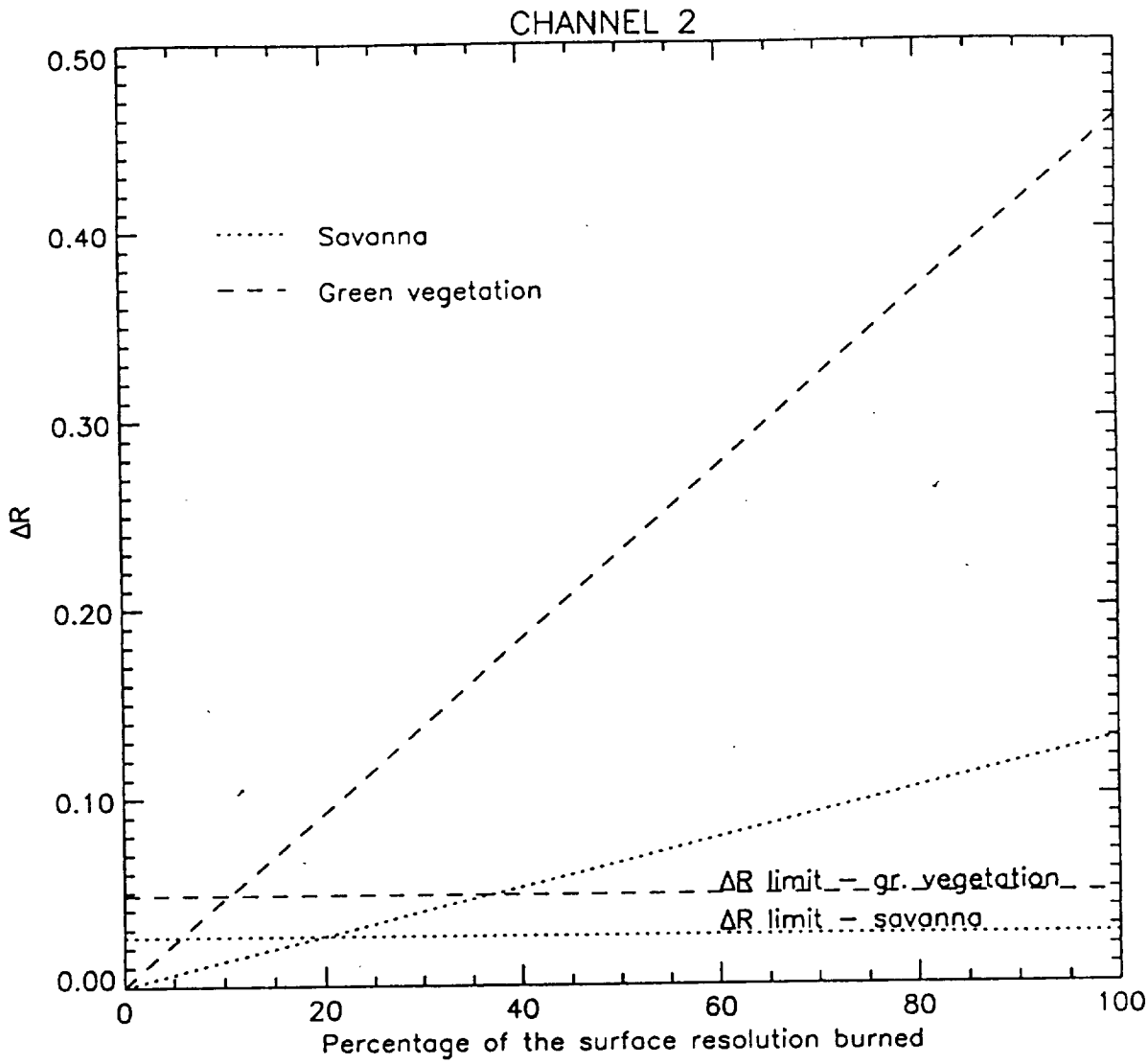
CHANNEL 2
0.50
0.40
0.30
0.20
0.10
0.00
ΔR
Savanna
Green vegetation
ΔR limit – gr. vegetation
ΔR limit – savanna
0
20
40
60
80
100
Percentage of the surface resolution burned

Fig. 17

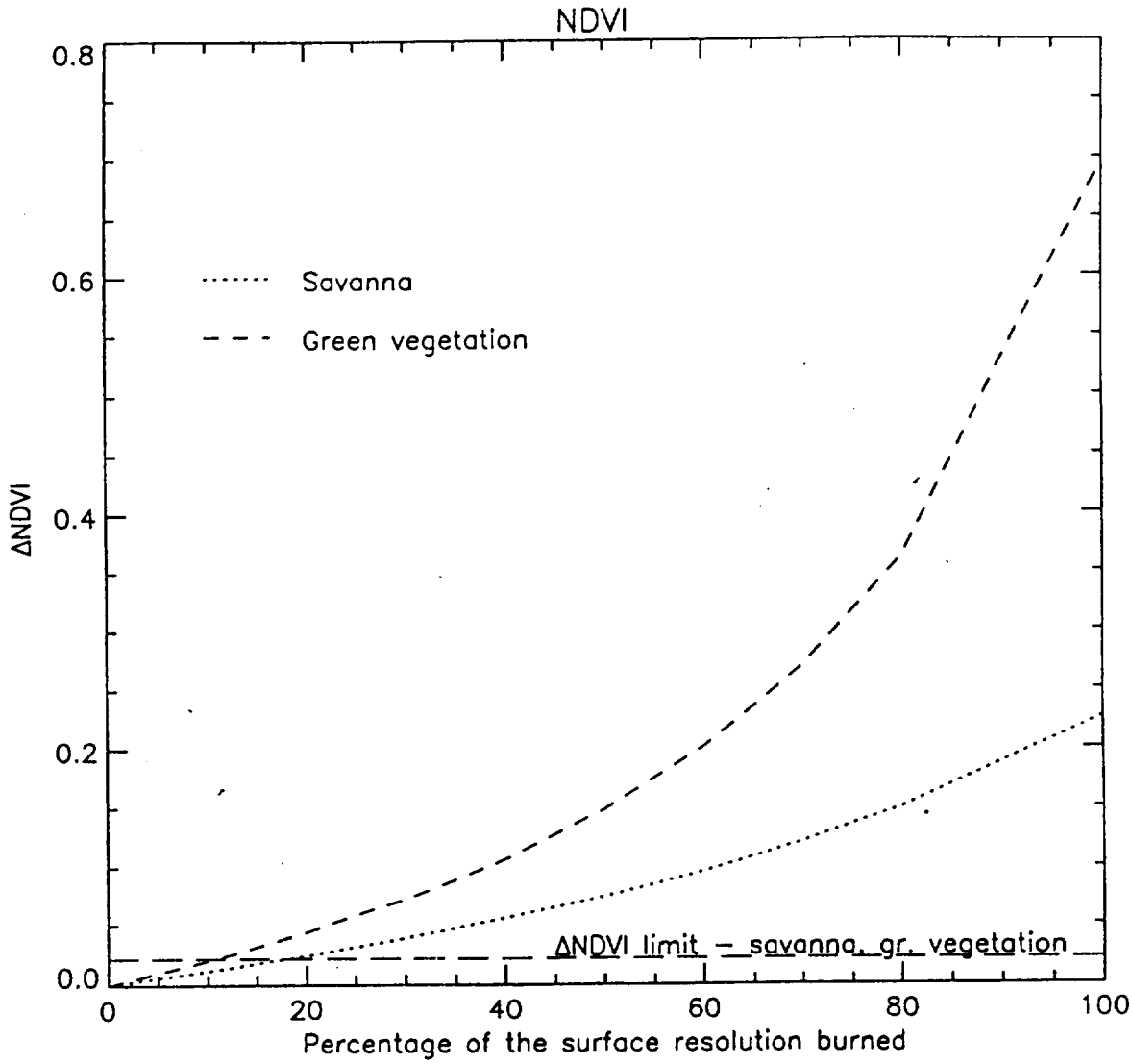
NDVI
0.8
0.6
0.4
0.2
0.0
ΔNDVI
Savanna
Green vegetation
ΔNDVI limit – savanna, gr. vegetation
0
20
40
60
80
100
Percentage of the surface resolution burned

Fig. 18